8-2004

Experimental investigation of time dependent behavior of welded Topopah Spring Tuff

Lumin Ma
University of Nevada, Reno

University of Nevada, Reno

Experimental Investigation of Time Dependent Behavior of Welded Topopah Spring Tuff

A dissertation submitted in partial fulfillment of the
requirements for the degree of Doctor of Philosophy in
Geo-Engineering

by

Lumin Ma

Dr. Jaak J. K. Daemen/Dissertation Advisor

August, 2004

Experimental Investigation of Time Dependent Behavior of Welded Topopah Spring Tuff

UNIVERSITY OF NEVADA RENO

THE GRADUATE SCHOOL

We recommend that the dissertation
prepared under our supervision by

LUMIN MA

entitled

Experimental Investigation of Time Dependent Behavior of Welded Topopah Spring Tuff

be accepted in partial fulfillment of the
requirements for the degree of

DOCTOR OF PHILOSOPHY

[redacted]
Jaak Daemen, Ph.D., Advisor

[redacted]
James Carr, Ph.D., Committee Member

[redacted]
George Danko, Ph.D., Committee Member

[redacted]
Shen-Yi Luo, Ph.D., Committee Member

[redacted]
George Fernandez, Ph.D., Graduate School Representative

[redacted]
Marsha H. Read, Ph. D., Associate Dean, Graduate School

August, 2004

ABSTRACT

Four types of laboratory tests have been performed. Specimens were attained from four lithophysal zones of the welded Topopah Spring Tuff unit at Yucca Mountain, Nevada: upper lithophysal, middle nonlithophysal, lower lithophysal and lower nonlithophysal zones. Two types of tests are conducted to study time-dependent behavior: constant strain rate and creep tests. Sixty five specimens from the middle nonlithophysal zone were tested at six strain rates: 10^{-2}, 10^{-4}, 10^{-5}, 10^{-6}, 10^{-7}, and 10^{-8} s^{-1}. Test durations range from 2 seconds to 7 days. Fourteen specimens from middle nonlithophysal, lower lithophysal and lower nonlithophysal zones are creep tested by incremental stepwise loading. All the tests are conducted under uniaxial compression at room temperature and humidity.

Specimens exhibit extremely brittle fracture and fail by axial splitting, and show very little dilatancy if any. It is assumed that microfracturing dominates the inelastic deformation and failure of the tuff. Nonlinear regression is applied to the results of the constant strain rate tests to estimate the relations between peak strength, peak axial strain, secant modulus and strain rate. All three these parameters decrease with a decrease of strain rate and follow power functions: $\sigma_{peak} = 271.37\dot{\varepsilon}^{0.0212}$, $\varepsilon_{peak} = 0.0066\dot{\varepsilon}^{0.0083}$, $E_S = 41985.4\dot{\varepsilon}^{0.015}$. Secant modulus is introduced mainly as a tool to analyze strain rate dependent axial strain.

Two threshold stresses define creep behavior. Below about 50% of peak strength, a specimen does not creep. Above about 94% of peak strength, a specimen creeps at an accelerating rate. Between the two threshold stresses, a power law relates strain rate and stress.

One hundred fifty eight Brazilian (Indirect tensile splitting) tests have been performed at six different constant strain rates.

Nineteen lithophysal specimens were tested in uniaxial compression to study their fracture pattern. These specimens have a far less brittle failure mode. They slowly crumble, collapse, and maintain considerable relative strength beyond the peak. Due to the presence of multiple relatively large lithophysal cavities, they are far weaker and softer than the nonlithophysal specimens.

ACKNOWLEDGEMENTS

Many people have made great contributions to my doctoral research and dissertation. They accompanied me walking through an important journey in my life. Their names have been borne firmly in my mind.

My deepest gratitude goes to my major advisor, Professor Jaak Daemen, for his extremely insightful guidance.

My gratitude is also extended to the other members of my doctoral advisory committee, Professor George Danko, Professor James Carr, Professor Shen-Yi Luo and Professor George Fernandez, for their advice and valuable suggestions.

I am very grateful to Mr. Rick Blitz, laboratory technician and Ms. Cheryl Breland, department administrative assistant for their technical assistance and cooperation.

Work presented in this dissertation was performed through U.S. Department of Energy Cooperative Agreement No. DE-FC28-98NV12081, Technical Task Representative Mr. Jaime Gonzalez. Support and cooperation are gratefully acknowledged. Valuable discussions with Dr. Mark Board are gratefully acknowledged.

I would like to give special thanks to Ms. Amy Smiecinski, the QA Manager in Harry Reid Center for Environmental Studies, and her staff QA experts, Mr. Morrie Roosa, Mr.

Robert Fulwider, Mr. Raymond Keeler and Ms. Barbara Roosa, for their quality assurance. Their rigorous work made all measurements in my research even more accurate and precise, and all the data traceable.

I would like to give many thanks to my family for their love, encouragement and patience.

TABLE OF CONTENTS

LIST OF TABLES

LIST OF FIGURES

LIST OF SYMBOLS

D	Diameter
E_S	Secant elastic modulus
K_I	Stress intensity factor
K_{IC}	Critical stress intensity factor or fracture toughness
L	Length
P	Force
s	Second
t	Time
α, β	Constants in transient creep equation
ε	Axial strain
ω	Damage factor
ε_e	Elastic strain component
ε_{in}	Inelastic strain component
ε_{long}	Peak axial strain of specimens curves for long term tests
ε_{loss}	Maximum reduction of peak axial strain curves for slow tests
ε_{peak}	Peak axial strain
ε_{tr}	Axial strain generated during transient creep
ε_s	Axial strain generated in steady-state creep
ε_{short}	Ultimate axial strain of specimens curves for short term tests
ε_{damage}	Axial strain component resulted from strain rate effect
ε_{total}	Total axial strain
ε_0	Initial axial strain
$\dot{\varepsilon}$	Axial strain rate
$\dot{\varepsilon}_{tr}$	Axial strain rate during transient creep
$\dot{\varepsilon}_s$	Axial strain rate during steady-state creep
σ	Axial stress
σ_{loss}	Strength reduction
σ_{peak}	Peak uniaxial strength

CHAPTER 1 INTRODUCTION

This study is a part of an investigation of welded Topopah Spring Tuff at the Yucca Mountain site. The purpose of the study is to improve our understanding of the time dependent behavior of the tuff. This study will provide knowledge about the long term mechanical properties of the host rocks of the repository excavations, which serves for engineering design and numerical simulation of the repository excavations.

1.1 Yucca Mountain

For over two decades, the Yucca Mountain Project has conducted an extensive scientific effort to determine whether Yucca Mountain, Nevada is a suitable site for a deep underground facility called a HLW (High Level Radioactive Waste) repository. The purpose of a repository is to safely isolate high level radioactive nuclear waste for at least 10,000 years. On July 9, 2002, the U.S. Senate cast the final legislative vote approving the development of a repository at Yucca Mountain. The Yucca Mountain Project is currently focused on preparing an application to obtain a license from the U.S. Nuclear Regulatory Commission to construct a repository (OCRWM, 2004).

Yucca Mountain lies in southern Nevada, in the Great Basin, which is part of the Basin and Range structural/physiographic province (Fig. 1.1). In the Yucca Mountain area, pre-Tertiary rocks consisting of a thick sequence of Proterozoic and Paleozoic sedimentary

rocks underlie approximately 1000 to 3000 m of Miocene volcanic rocks (OCRWM, 1999).

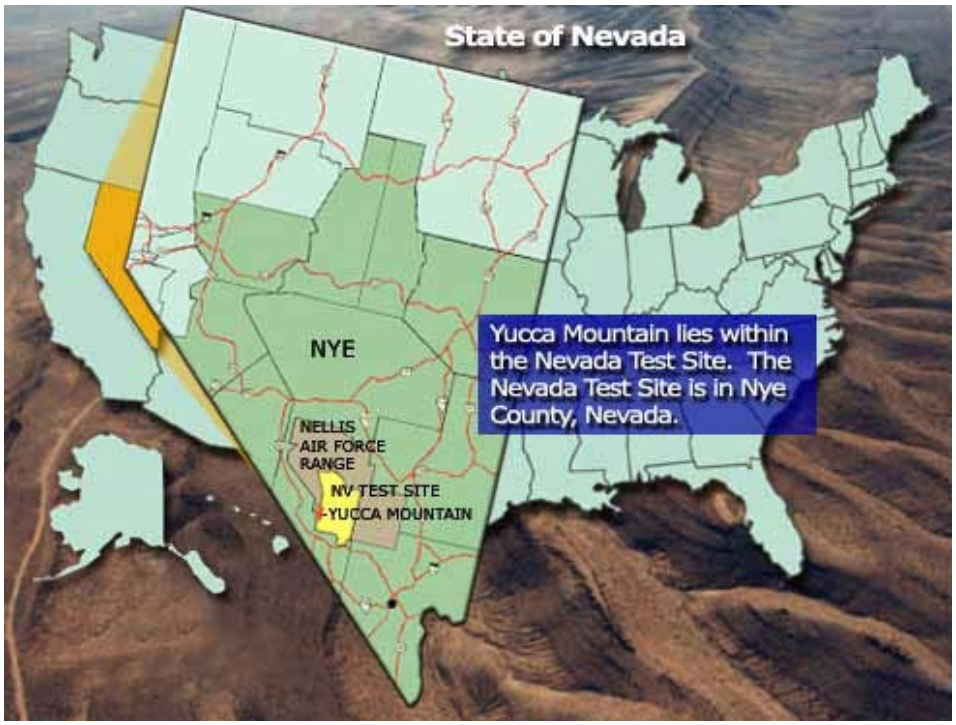

Figure 1.1 Map of Nevada showing the location of the Yucca Mountain site (from the website of OCRWM, 2004)

The Miocene volcanic sequence exposed at Yucca Mountain includes units of the Paintbrush and Timber Mountain Groups. The Paintbrush Group consists of pyroclastic rock and lavas originating from the Claim Canyon caldera, approximately 6 km north of the study area, and from 12.8 to 12.7 million years old. The Paintbrush Group includes a homoclinal sequence consisting of four formations, the Tiva Canyon, Yucca Mountain, Pah Canyon, and Topopah Spring Tuffs (Fig. 1.2). These formations consist of pyroclastic-flow and pyroclastic-fall deposits with interbedded lavas which dip 5 to 10 degrees to the east. Two of these formations, the Topopah Spring and Tiva Canyon Tuffs,

are voluminous, densely welded, compositionally zoned pyroclastic outflow sheets that grade upward from rhyolite composition to quartz latite composition. The tuff and ash flows of the Timber Mountain Group erupted from the Timber Mountain caldera complex and consist of the Ammonia Tanks Tuff and the Rainer Mesa Tuff (OCRWM, 1999).

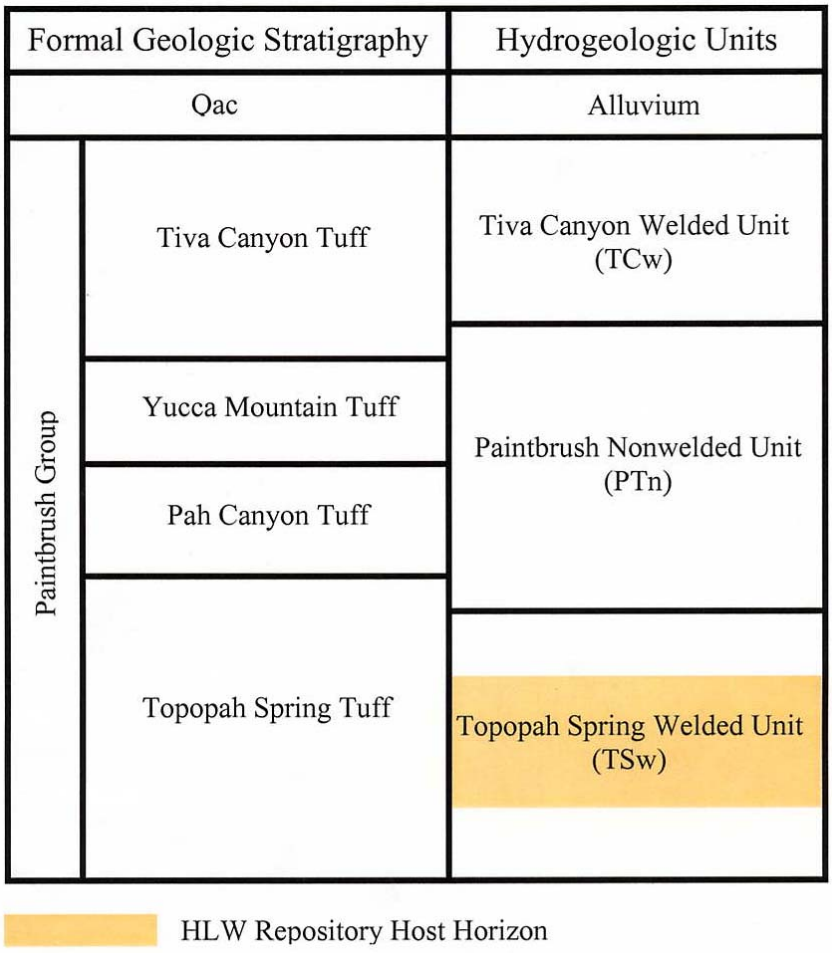

Figure 1.2 Stratigraphic column showing rock formations in Paintbrush Group and HLW Repository Horizon (modified from Figure 3-21 in OCRWM, 2002b)

About 300 m below the surface of Yucca Mountain is the Topopah Spring Tuff formation (OCRWM, 1999). The repository for high-level radioactive nuclear waste is to be

excavated entirely within this formation (Figs. 1.2 and 1.3). Units exposed in the crystal-poor member of the Topopah Spring Tuff include the Topopah Spring crystal-poor upper lithophysal zone (Tptpul), the Topopah Spring crystal-poor middle nonlithophysal zone (Tptpmn), the Topopah Spring crystal-poor lower lithophysal zone (Tptpll), and the Topopah Spring crystal-poor lower nonlithophysal zone (Tptpln) (OCRWM, 1999).

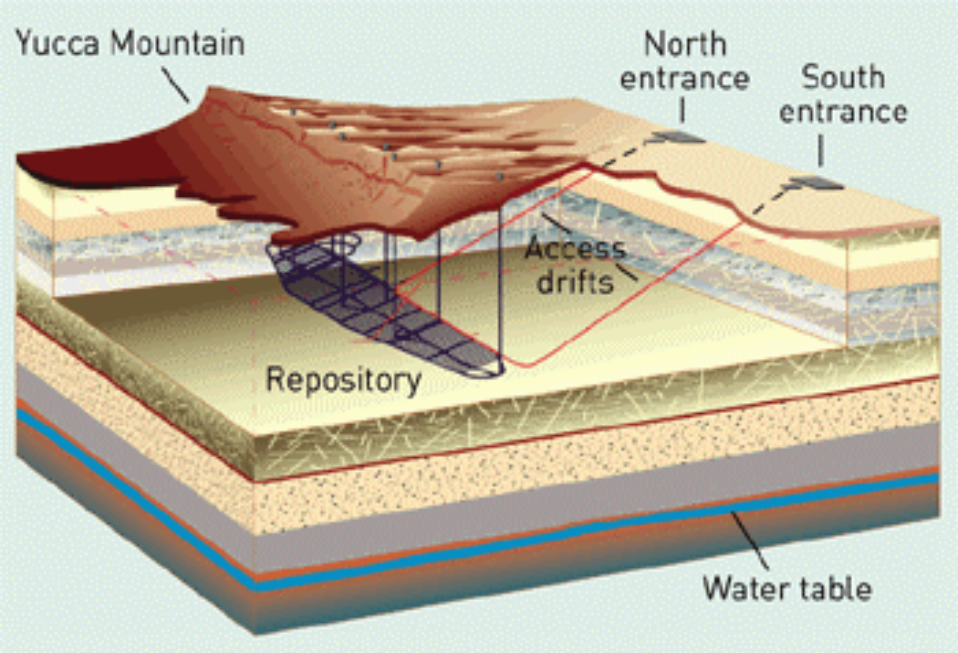

Figure 1.3 Repository design and operations concept overview (from the website of OCRWM, 2004)

The repository excavations are divided into two types in terms of their usage: emplacement drifts and nonemplacement areas. The nonemplacement excavations include main drifts, exhaust main and turnouts. Turnouts are curved sections of tunnel connecting the emplacement drifts to the main drifts. Emplacement drifts are exposed to higher temperatures than nonemplacement openings (OCRWM, 2002a).

1.2 Reason for time dependence study

The NRC (U.S. Nuclear Regulatory Commission) regulation, 10 CFR Part 63 (66 FR 55732) establishes a period of 50 years after the start of emplacement in which retrieval must be possible, unless a different period is specified by the NRC. The DOE (U.S. Department of Energy) has developed a design for a Yucca Mountain disposal system that could give future generations the choice of either closing and sealing the underground facility as early as allowable under NRC regulations or keeping it open and monitoring it for a longer time period. The design for the repository would not preclude the option for future generations to make societal decisions to monitor the repository for up to 300 years before making decisions to close the underground facility (OCRWM, 2002a).

Design criteria for both emplacement and nonemplacement drifts ground control includes the following requirements directly related to worker safety (OCRWM, 2002a):

1) The ground support systems must be designed to prevent rockfall that could result in personnel injury.

2) The ground control system must be designed to withstand a Category 1 or Category 2 earthquake, as appropriate to the seismic frequency classification assigned to each particular structure, system, and component.

3) The ground control system must be designed to include provisions which support a deferral of closure for up to 300 years.

4) The ground support systems must be designed to function without planned maintenance during the operational life of the repository while providing the option to perform unplanned maintenance as needed.

Available field evidence shows that rock excavations change in their shapes with time after their support systems have been installed and their surrounding stress redistribution is completed. This phenomenon is known as time dependence. For the 300-year design life, the long-term stability of the emplacement and nonemplacement drifts in the repository must receive major consideration. For this reason, long-term deformation and long-term strength of the surrounding rock must be well understood.

1.3 Methods of study

The study of time dependent behavior of the tuff is conducted based on two types of laboratory tests:

1) **Constant strain rate test**. Eighty eight cylindrical tuff specimens collected from Alcove #5 which is located in the middle nonlithophysal zone have been tested at a series of constant strain rates. This type of test provides information on how the

mechanical properties change with strain rate. The constant strain rate test is presented and discussed in Chapter 4.

2) **Constant stress test, also known as creep test.** Fourteen cylindrical tuff specimens collected from the middle nonlithophysal zone, the lower lithophysal zone and the lower nonlithophysal zone have been tested under uniaxial compression at room temperature. The cumulated time duration is about 401 days. Most important information expected from this type of test is the change of strain rate under applied stress for an extended period of time. The constant stress test is presented and discussed in Chapter 5.

Laboratory testing suggests that the tuff specimens from the three zones (middle nonlithophysal zone, lower lithophysal zone and lower nonlithophysal zone) exhibit brittle fracture. This feature has also been extensively described in site characterization (OCRWM, 1999). Based on the experimental observations and literature survey, the deformation and failure of the tuff is understood as resulted from microfracture initiation, propagation and coalescence. Given the testing results, three major outcomes have been developed as follows (a flow chart is given in Fig. 1.4).

1) An innovative method is suggested to separate the strain rate effected strain component from the total axial strain. The strain rate effected strain is caused by strain rate dependent stiffness damage of the specimen.

2) Strain rate dependent strength has been estimated using nonlinear regression method. The long term strength of the tuff is predicted based on the estimated regression equation.

3) At low stress, the tuff does not creep regularly. However, a power law for the creep rate is found when the stress reaches a certain level. This characteristic complies with the microfracture development in brittle rocks. A creep law for the tuff is suggested based on the results of both constant strain rate tests and creep tests.

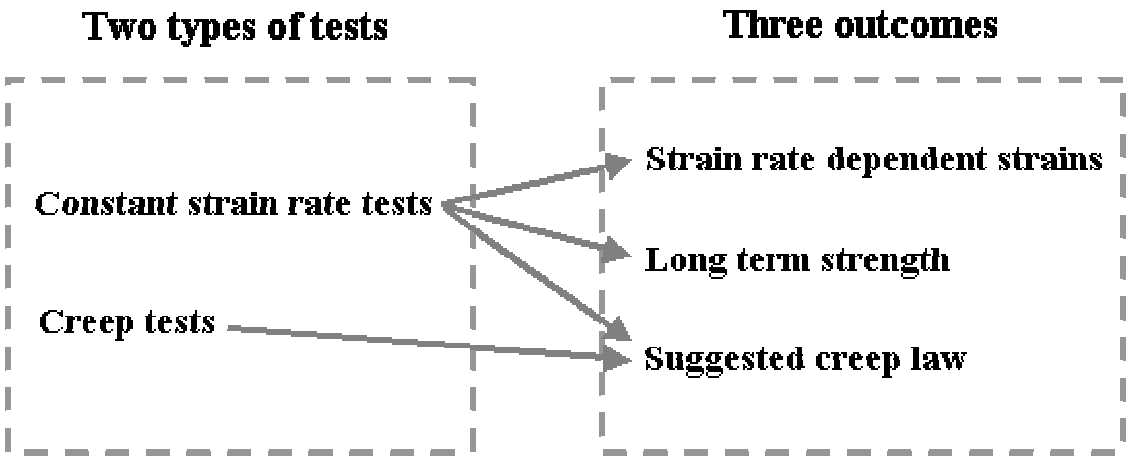

Figure 1.4 The relationships between laboratory tests and the outcomes.

1.4 Structure of this dissertation

Following this introductory chapter, seven chapters follow. Chapter 2 gives an overview of the current state of the art in mechanisms of brittle failure of rocks and their time

dependency. Chapter 3 introduces specimen preparation, experimental procedures, test conditions and test results for time dependence study (Chapters 4 and 5). Chapters 4 and 5 present experimental observations and analyses for constant strain rate and creep tests, respectively. Theoretical interpretations of the phenomena observed in the experiments are given wherever they are needed in these two chapters. Chapter 6 describes Brazilian (Indirect tensile splitting) test studies and their results. Chapter 7 presents details on the testing of lithophysal specimens, and the results of these tests. The results in Chapters 6 and 7 provide supporting knowledge for the three major outcomes addressed in Section 1.3, and give a better understanding of the mechanical behavior of Yucca Mountain tuff. Chapter 8 gives a summary, conclusions and recommendations. Appendix A gives a summary of all constant strain rate tests. Appendix B graphically presents creep tests.

CHAPTER 2 LITERATURE REVIEW

2.1 Brittle fracture in rocks

General. Bieniawski (1967a) and Lemaitre (1992) define brittle fracture as a fracture that exhibits no or little permanent (plastic) deformation. A brittle rock is understood to be a rock that fails in brittle fracture. Cruden (1970) describes a brittle rock as one that fractures at small strains with loss of cohesion between the fracture surfaces. Scholz (1968b) suggests that one of the most interesting properties of a brittle rock is the extensive small scale cracking that accompanies the deformation in compression.

In order to gain a sufficient understanding of inelastic deformation in brittle rocks, it is necessary to investigate the basic micromechanisms of the deformation and to relate these mechanisms to characteristic macroscopic rock properties (Costin, 1983). Griffith assumed that brittle material is filled with sharp flaws or 'Griffith cracks'. Applied stress is locally modified by these cracks, and may become tensile on certain points on a crack surface, even when the applied stress is wholly compressive (Odé, 1960, p. 297 cited by Brace and Bombolakis, 1963; Bieniawski, 1967a). Rock is a polycrystalline aggregate generally of several anisotropic phases. If a uniform stress is applied to such an inhomogeneous material, the local stress at a point will not, in general, be the same as the applied stress but will vary in some complex way throughout the body (Scholz, 1968b). This inhomogeneity is the basic factor governing the microfracturing of rock (Scholz, 1968a; Costin and Holcomb, 1983).

A large number of investigations on mechanisms of inelastic deformation in brittle rocks and in other brittle materials have been performed since the 1920's, especially within the last forty years (Shen et al, 1995; Wong et al, 2001). It has been widely accepted that the main mechanism of inelastic deformation in brittle rocks under uniaxial compression is characterized by the development of cracks parallel to the compressive stress direction (Brace and Bombolakis, 1963; Walsh, 1965; Brace et al., 1966; Cruden, 1970; Lajtai, 1971; Martin, 1972; Kranz and Scholz, 1977; Horii and Nemat-Nasser, 1985; Costin, 1985; Layanyi, 1993; Lemaitre, 1992; Martin, 1997). Brace et al. (1966), Costin and Holcomb (1983), Horii and Nemat-Nasser (1985), Shen et al. (1995) suggest that initiation, propagation and interaction of microcracks are the dominant, controlling microevents which lead to macroscopic fracture and failure of rocks under overall compression.

Half strength feature and dilatancy. Observations of microfracturing activity during compression tests demonstrate that microfracturing begins at approximately half the fracture stress (Scholz, 1968a). As stress is increased above this point, the rate of microfracturing events steadily increases until about 90 – 95% of its breaking strength, where a very rapid acceleration of activity was observed. For brittle rocks the microfracturing is often accompanied by dilatancy. Bieniawski (1967a) suggests that the stress threshold for dilatancy marks the initiation of microcrack propagation or proliferation. Brace et al. (1966) find that the dilatancy begins at a stress one-third to two-thirds of the fracture stress based on test results for Westerly granite, marble and aplite.

By comparing the pattern of microfracturing directly with observed macroscopic behavior, Scholz (1968b) finds that dilatancy could be attributed to microfracturing.

Near failure feature. As a rock approaches failure, cracks begin to interact, finally forming macrocracks and faults (Costin, 1983; Lauterbach and Gross, 1998). Wong et al (2001) point out that failure mechanism strongly depends on the crack coalescence pattern between pre-existing flaws. The peak strength of a specimen does not depend on the initial crack density but on the actual number of pre-existing flaws involved in the coalescence. Anderson and Grew (1977) suggest that for fast fracture, there exists a critical stress intensity factor K_{IC} above which rapid unstable crack propagation occurs.

2.2 Time dependency of brittle fracture in rocks

The strength of brittle rocks is time dependent. If such a rock is subjected to a constant load it will, in general, fracture after some time interval (Scholz, 1968b). Anderson and Crew (1977) and Costin (1983) point out that microcrack growth is important in creep deformation of brittle rock where time dependent crack growth occurs by a stress corrosion mechanism. Stress corrosion cracking is environment-induced subcritical crack growth under sustained stress. The weakening of strength of rocks in time is known as static fatigue. It has been shown for a wide variety of materials that static fatigue is due to stress corrosion; i.e., when a brittle material is stressed in a corrosive environment, the high tensile stresses at the tips of cracks accelerate the corrosion reaction there so that the cracks tend to lengthen (Scholz, 1968b). The primary corrosive agent responsible for

static fatigue of silicate materials is water (Charles, 1959; le Roux, 1965 cited by Scholz, 1968b).

In the presence of a chemically active environment, such as water vapor, cracks can grow under subcritical conditions, $K_I < K_{IC}$. In experiments on glass (Wiederhorn and Bolz, 1970), pure quartz (Martin, 1972), and rock (Henry et al., 1977) it has been shown that the rate of crack growth can be related to the applied stress intensity factor. This relationship can be approximated by

$$\frac{\delta a}{\delta t} = \Gamma e^{\beta K_I} \tag{2.1}$$

where Γ and β are material parameters and are functions of environmental conditions, principally temperature and the partial pressure of water vapor.

Creep at temperatures below about a fifth of the melting temperature and stress levels above approximately half the maximum strength is produced by microcracking (Scholz, 1968c). Costin (1985) proposes that if a material is stressed below a threshold stress level and allowed to creep, the creep rate should decay to zero over time and no failure will occur. If the threshold stress level is exceeded, the damage level will continue to evolve, resulting in an eventual acceleration of the creep rate (tertiary creep) and failure.

Martin (1972) finds that for randomly oriented cracks the strain rate of a rock in creep is proportional to the rate of crack growth. Layanyi (1993, p. 79) suggests that modeling of time-dependent behavior of rocks in the brittle regime is principally a matter of fracture

mechanism. The similarity in form between the creep curve and that for time-dependent crack growth is in itself not sufficient to conclude that crack growth is the mechanism of creep in brittle rocks. What is needed is a theory of creep that defines the observed strain in terms of time-dependent crack growth (Martin et al., 1995, p. 6).

The difference between the creep test and rapid fracture test lies in the method of overcoming the energy barrier. In the fracture test, the energy is supplied by the continuously increasing stress, which drives the cracks to extend and interact. In creep testing, at a constant stress, cracks propagate into a stable position and stop. Further growth occurs when the energy barrier is lowered by a stress corrosion reaction at the crack tip (Layanyi, 1993, p. 83).

2.3 Microfracture growth in rocks

After performing a series of experiments, including some using microscope cover glass, Brace and Bombolakis (1963) summarize that crack growth occurred by extension of the initial crack along a curving path which gradually becomes parallel with the direction of compression. When this direction was attained further crack growth stopped. Costin and Holcomb (1983) suggest that as rock is loaded in compression it initially responds elastically. When the applied stress reaches a sufficient magnitude, the stress intensity factor associated with the most favorably oriented cracks reaches the critical value and these cracks begin to grow. Fig. 2.1 gives a conceptual description for a single inclined crack extension under compression stress. Under increasing compression the crack faces

begin to slide. This leads to the nucleation of tension cracks (wings) at the tips of the preexisting crack. As the load further increases these tension cracks grow and curve towards the direction of maximum compression (Lauterbach and Gross, 1998).

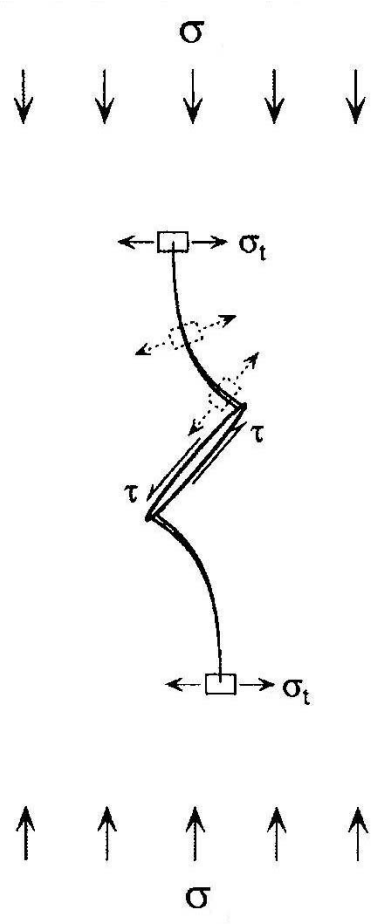

Figure 2.1 Schematic diagram of a single pre-existing crack extension towards the compression stress (from Eberhardt et al., 1998).

From the usual arguments given in brittle fracture theory, the longest cracks will grow first. These grow and become stable, and then shorter and less favorably oriented cracks are successively activated as stress is raised. All of these grow by lengthening in an axial direction; sliding on the inclined cracks then causes the axial cracks to open. At this stage

the rock is observed to be dilatant (Brace et al., 1966). In an experiment to simulate an isolated crack growth using a photoelastic technique, Brace and Bombolakis (1963) find that in compression, the most severely stressed crack is inclined at about 30° to the axis of compression.

More experimental study has been done on crack propagation from a single pre-existing crack in compression. Examples include the work of Lajtai (1971) on plaster of Paris, Martin (1972) on quartz, and Horii and Nemat-Nasser (1985) on CR39. Recently, Shen et al. (1995), Bobet and Einstein (1998a), Bobet and Einstein (1998b), Vasarhelyi and Bobet (2000) and Sagong and Bobet (2002) have studied crack propagation and coalescence on model-rock specimens containing two inclined flaws which are either both open or closed. Wong et al. (2001) and Tang et al. (2001) have investigated crack propagation and coalescence both experimentally and numerically on model-rock specimens containing three inclined flaws.

It is reported from both experiments and numerical simulations that two main types of newly created fractures are observed during loading of a specimen containing a pre-existing inclined crack. One type is the tensile fracture, or wing fracture or primary fracture, which is clearly caused by tensile stress concentrations at the tips of pre-existing fractures and propagates in a curved path toward the direction of loading. The wing fractures initiated from a frictional pre-existing fracture are less curved than those from a nonfrictional pre-existing fracture. The other type of fracture appears after the wing

fracture and is called a shear fracture or secondary fracture (Shen et al, 1995). The conceptual diagram in Fig. 2.2 gives an illustration.

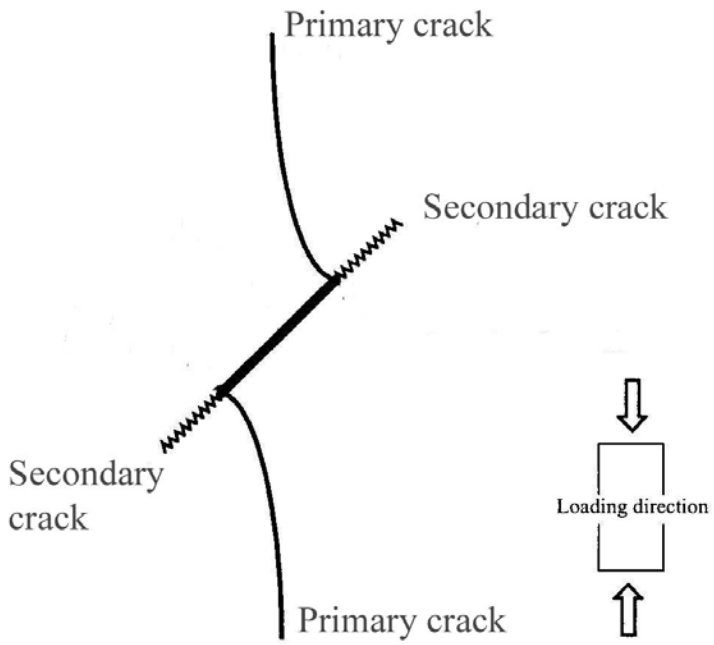

Figure 2.2 Crack pattern observed in pre-cracked specimen of rock materials in uniaxial compression (modified from Sagong and Bobet, 2002).

Bobet and Einstein (1998) find that wing cracks grow in a stable manner since an increase in load is necessary to lengthen the cracks, and align with the direction of the largest compressive load. Shear cracks appear later and are responsible, in most cases, for specimen failure. Shear cracks in most cases initiate in a direction coplanar to the crack. In numerical simulations, Tang et al. (2001) suggest that a shear crack propagates in an unstable manner.

As the rock approaches failure, cracks begin to interact, finally forming macrocracks and faults (Costin, 1983). Coalescence is unstable crack propagation. The failure mechanism strongly depends on the crack coalescence pattern between pre-existing flaws. The peak strength of a specimen does not depend on the initial crack density but on the actual number of pre-existing flaws involved in the coalescence (Wong et al, 2001).

Costin (1985) concludes that if the compressive stress is sufficiently large then K_I will approach the critical value for crack growth, K_{IC} and a small amount of crack growth will take place. When $K_I > K_{IC}$ unstable crack growth does not occur because the crack is imbedded in a localized region of tensile stress; thus, as the crack grows, the local stress is relieved reducing the driving force on the crack. The crack only grows for enough to come to an equilibrium point where $K_I = K_{IC}$. As the external load is increased, the crack will again grow to a new equilibrium position. If the stress is reduced, the crack length remains fixed. Lauterbach and Gross (1998) find that under uniaxial compression the stress intensity factor decreases monotonically with increasing wing length. This means that crack growth will be arrested after a certain crack length has been attained. It is then necessary to increase the load to achieve further crack growth.

CHAPTER 3 EXPERIMENTAL DESCRIPTIONS AND RESULTS FOR TIME DEPENDENCE STUDY

3.1 Specimen preparation

This chapter introduces the tests discussed in Chapters 4 and 5. To study the time dependent behavior of tuff, two types of tests have been conducted: constant strain rate tests (Chapter 4) and creep tests (Chapter 5). Specimens are prepared from rock cores (Fig. 3.1). The rock cores are received from the Sample Management Facility (SMF), Yucca Mountain Site Characterization Project. The rock cores for the two types of tests are collected from the middle nonlithophysal (Tptpmn), lower lithophysal (Tptpll) and lower nonlithophysal (Tptpln) zones of welded Topopah Spring Tuff. The nominal diameters of the cores are 2.4 inch (60.96 mm) and 1.78 inch (45.21 mm). Most cores contain various flaws such as lithophysae, vapor-phase altered zones, fractures, etc. Lithophysae are gas-formed voids created soon after emplacement of the ash-flow tuff. Vapor-phase altered zones are regions of tuff matrix altered by gases in the early stages of tuff emplacement (Martin, III et al, 1993; Buesch and Spengler, 1998). Some lithophysae and vapor-phase altered zones are visible on the surface of the cores (Fig. 3.2 (a)). Others are not, and can only be recognized after the core breaks (Fig. 3.2 (b)). When preparing a specimen, lithophysal cavities and large vapor-phase altered zones can be avoided or can be expressly included, e.g. to study their influence on the mechanical behavior of the rock. Small vapor-phase altered zones appear so frequently that often they are difficult to avoid.

(a) (b) (c)

Figure 3.1 Rock cores received from SMF at Yucca Mountain site. All these cores are collected from the Tptpmn zone. (a) and (b) = 2.4 inch diameter, (c) = 1.78 inch diameter.

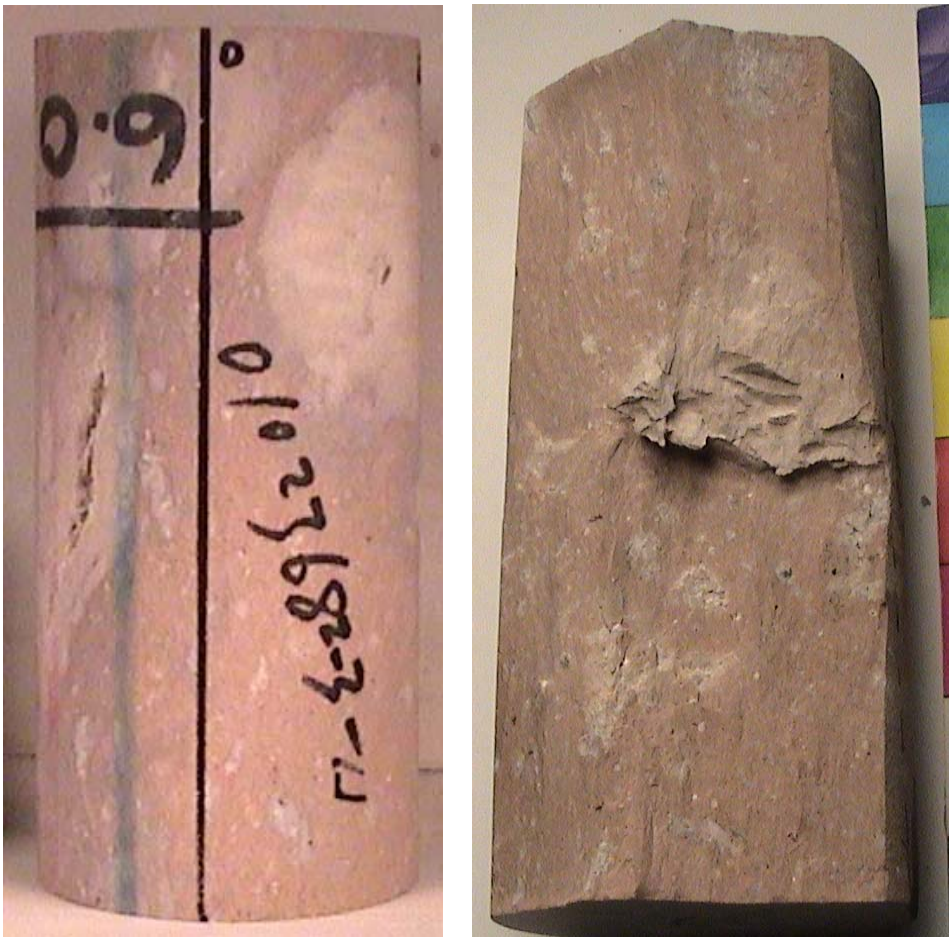

(a) (b)

Figure 3.2 Specimens with lithophysae and/or vapor-phase altered zones, either visible on the specimen surface (a) or contained inside the specimen (b).

All the specimens are prepared in the sequence: cut to length → grind top and bottom → measure dimensions and weight → measure moisture content (moisture content for a small number of specimens is measured immediately after testing, for a few is not measured) → install strain gages → take photos → test → take photos. This process follows ASTM D 4543-85.

3.2 Numbering of specimens and tests

Every rock core received is identified with a barcode. It has an eight-digit number, e.g. 01023363. All the test specimens are numbered to inherit the barcodes of rock cores from which the specimens are prepared. In addition to the barcode, two more pieces of information are incorporated to number or identify a specimen: serial number of the specimen in the rock core and type of test. Fig. 3.3 gives a description of the system of specimen numbering.

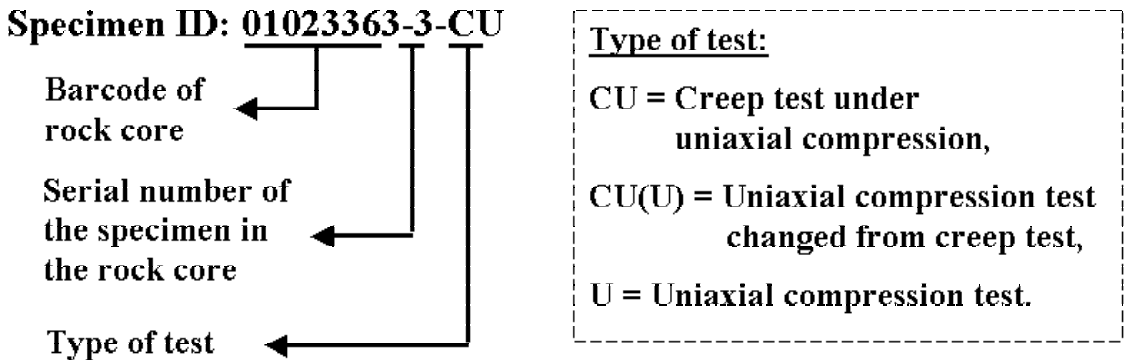

Figure 3.3 Specimen numbering system

Each test is performed with one specimen. A test is identified with the ID of the specimen that is tested. Serial number refers to the number this particular specimen is assigned when a section of core is long enough to allow preparation of more than one test specimens.

3.3 Experimental setup

Two identical MTS (Material Testing System) servo-controlled testing machines are used for all the tests. Each has a 600 kip capacity and is controlled by an MTS TestStar IIm digital controller. Load is measured using a load cell. Displacement is measured using an LVDT (Linear Variable Differential Transducer) in the machine. Strain for most of the specimens is measured using 120-ohm electric resistance strain gages. For a small number of specimens testing for high strain rates (orders of 10^{-2} and 10^{-3} s^{-1}), strain is measured using 350-ohm strain gages. Six strain gages are installed on most specimens. Four measure axial strain. Two measure lateral strain. All strain gages are cemented at about midheight of the specimen. Strain in each direction is calculated by taking the average of all measurements in that direction. The data is collected using both the TestStar IIm data acquisition program and LabVIEW software. All the tests are conducted at room temperature and humidity. Fig. 3.4 shows an MTS testing machine with a specimen installed in and the controlling and recording computer.

Figure 3.4 An MTS servo-controlled testing machine with a specimen installed, and the controlling computer.

3.4 Specimen storage

Moisture contents of the rock cores received are low (typically < 0.8%). The rock cores have been stored in cardboard core boxes over extended periods of time, typically years. All specimens were stored in a rock mechanics laboratory, at room temperature and humidity (in a very dry climate, the average relative humidity in the room temperature is about 20%). When the rock cores were received, they were packaged in plastic bags, and they were left in the bags until they were prepared for testing.

3.5 Constant strain rate test

3.5.1 Test description

This type of test is applied to study the strain rate dependence of the tuff strength and stiffness. Eighty eight specimens have been tested at varying strain rates. All the specimens are collected from Alcove #5 which is located in the middle nonlithophysal (Tptpmn) zone. Sixty five of these do not contain obvious flaws. They are randomly divided into six groups to test at six strain rates: 10^{-2}, 10^{-4}, 10^{-5}, 10^{-6}, 10^{-7}, and 10^{-8} s^{-1}. The durations corresponding to each strain rate are about 2 seconds, 1 minute, 10 minutes, 1 day, 3 days and 7 days. The number of specimens in each group is not the same. Another group of specimens which contains obvious flaws in each specimen is tested to study failure patterns and explore how the peak strengths and especially the failure behavior are influenced by gross defects at a given strain rate. Most of the specimens in this second group are tested at the strain rate of 10^{-5} s^{-1} that falls in the time duration in ASTM D 2938-95 for standard uniaxial compression tests. Fig. 3.5 shows an example of specimens without obvious flaws and used for constant strain rate tests.

Figure 3.5 Specimens with and without obvious flaw (Nominal diameter = 2.4 inch or 60.96 mm, from Tptpmn).

At the time of testing all specimens had a low moisture content. Among the 65 specimens used for the constant strain rate testing, the moisture contents have been measured for 62. Forty five of these moisture contents have been measured before testing. The mean moisture content is 0.7%. Standard deviation is 0.1%. The moisture content of 17 specimens has been measured after testing. The mean is 0.75%. The standard deviation is 0.07%. All the measurements of moisture contents are listed in Appendix A.

3.5.2 Test results

Fig 3.6 gives stress-strain curves for six tests. It is not intended to show strain rate dependency of the curve in this plot, but to give an example that the specimens exhibit strong elasticity up to failure. For the strain rate dependence study, peak strength, peak

axial strain and elastic modulus for all the tests are expected and therefore have been determined. For some of the tests, peak lateral strain and Poisson's ratio have been obtained as well. A summary of all the test results is given in Appendix A.

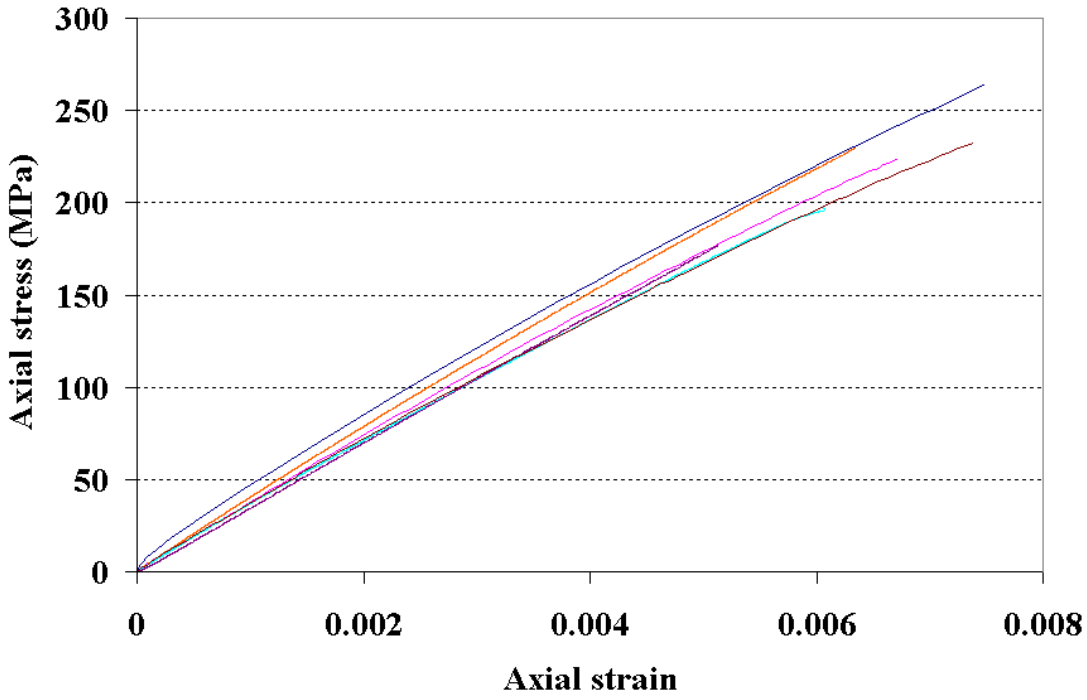

Figure 3.6 Axial stress–strain curves for six tests to represent the stress-strain relations for all the tests in constant strain rate testing. The tests used to construct the plot: 01023703-1-U ($\dot{\varepsilon} = 1.1\times10^{-4}\ \ s^{-1}$), 01023702-2-U ($\dot{\varepsilon} = 1.1\times10^{-5}\ \ s^{-1}$), 01025235-2-U ($\dot{\varepsilon} = 1.1\times10^{-6}\ \ s^{-1}$), 01025233-1-U ($\dot{\varepsilon} = 9.7\times10^{-8}\ \ s^{-1}$), 01023751-1-U ($\dot{\varepsilon} = 1.1\times10^{-7}\ \ s^{-1}$) and 01023707-3-U ($\dot{\varepsilon} = 1.3\times10^{-5}\ \ s^{-1}$). All the specimens are collected from Tptpmn.

The stress-strain curves in Fig. 3.6 exhibit nearly linear elasticity or very small inelastic deformation in the specimen during the course of loading. Fig. 3.7 gives a test performed with two loading-unloading cycles before loading to failure. The unloading is started at

76% of its peak strength. The permanent strain is extremely small ($<< 4\times10^{-5}$). This specimen was collected from the lower lithophysal zone, which is next to where the specimens for constant strain rate tests were collected. They have very similar mechanical properties. The specimen is shown in Fig. 3.8.

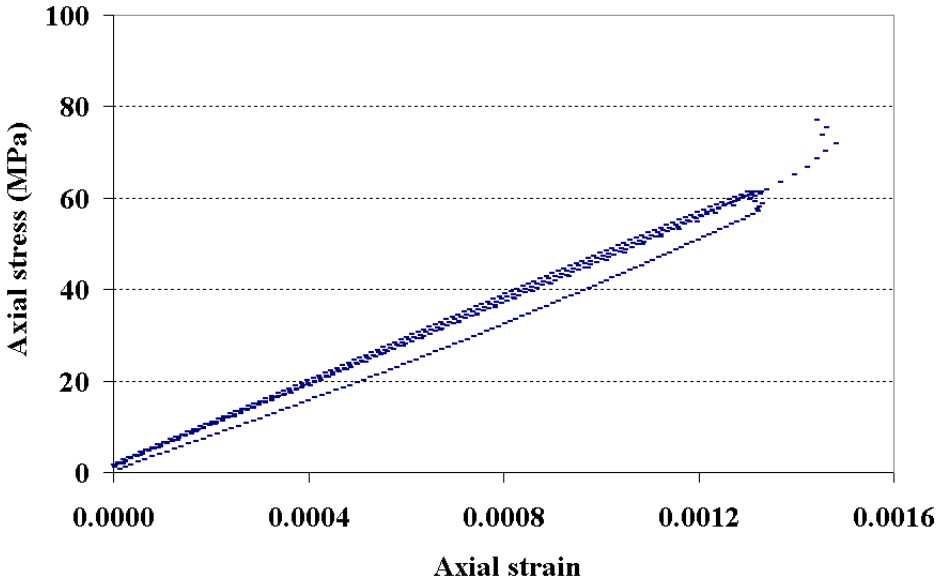

Figure 3.7 Two loading-unloading loops of stress-strain curve showing extremely small permanent deformation in the specimen (Specimen ID: 01014764-2-CU(U), peak strength = 80.53 MPa, from Tptpll).

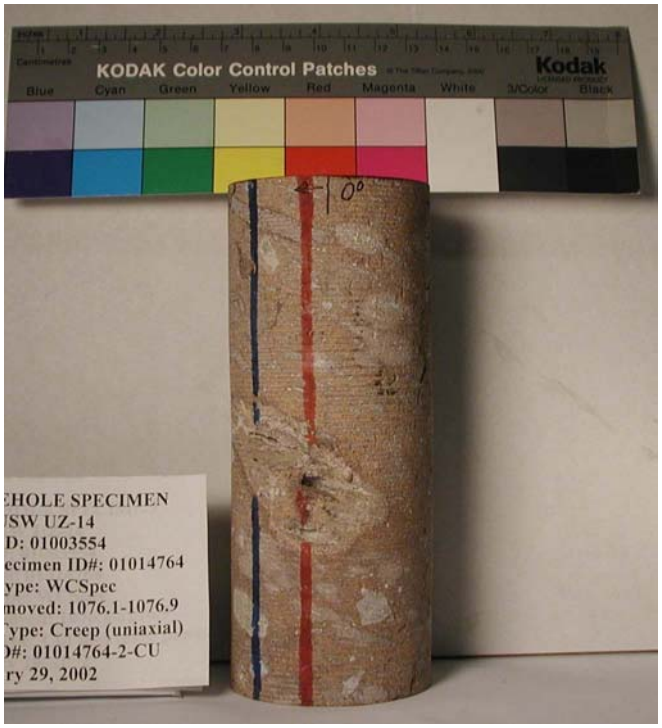

Figure 3.8 Specimen which experienced two loading-unloading loops of stress-strain curve showing extremely small permanent deformation (Specimen ID: 01014764-2-CU(U), peak strength = 80.53 MPa, from Tptpll). Notice larger vapor altered inhomogeneities.

All specimens failed in a very brittle manner. Fig. 3.9 shows a broken specimen and its equivalent failure pattern. The specimen fails nearly parallel to its axis, or the loading direction, by predominantly longitudinal splitting.

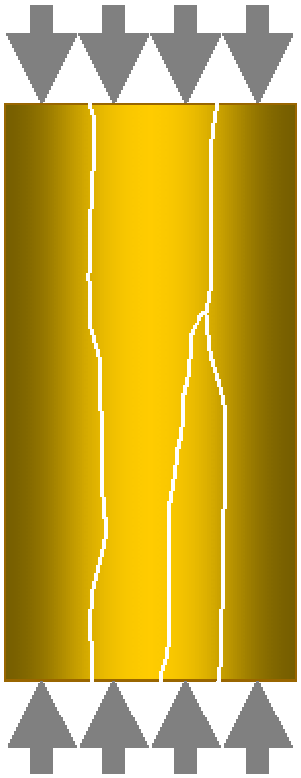

(a) A failed specimen (b) An equivalent failure pattern

Figure 3.9 Typical failure pattern (Specimen ID: 01014951-1-CU, from Tptpmn).

Fig. 3.10 gives another four failed specimens. The two on left hand side contain vapor-phase altered spot (in white color). Such inclusions usually affect the strength significantly. They are difficult, often impossible, to detect before testing.

Figure 3.10 Specimens after failure. Longitudinal splitting dominates the failure mode of all these specimens. Vapor-phase altered spots are present inside the specimens. The IDs for the specimens: 01023582-1-U ($\dot{\varepsilon} = 2.5\times10^{-5}s^{-1}$, σ_{peak} = 202.98 MPa), 01023657-1-U ($\dot{\varepsilon} = 1.0\times10^{-5}s^{-1}$, σ_{peak} = 233.16 MPa), 01023668-3-U ($\dot{\varepsilon} = 1.4\times10^{-8}s^{-1}$, σ_{peak} = 113.21 MPa) and 01023667-1-U ($\dot{\varepsilon} = 1.2\times10^{-6}s^{-1}$, σ_{peak} = 176.63 MPa). All the specimens were collected from Tptpmn.

For a certain strain rate, the peak strengths (σ_{peak}) and the corresponding peak axial strains (ε_{peak}) fluctuate widely. Relatively, the secant moduli (E_S) at peak strength are less variable. Table 3.1 gives the statistics of these three parameters for 18 specimens tested at the strain rate of $10^{-5}\ \ s^{-1}$.

Table 3.1 Statistics of three parameters (peak axial strain at failure, peak strength, secant modulus) for 18 specimens tested at strain rate of $10^{-5}\ s^{-1}$

	ε_{peak}	σ_{peak}, MPa	E_S, GPa
Minimum	0.00331	122.28	31.02
Maximum	0.00822	291.64	40.64
Mean	0.00607	214.28	35.49
Median	0.00626	224.62	35.78
Std Deviation	0.00142 (23.4%)*	49.19 (23%)*	2.57 (7.2%)*

* % of mean

All the tests for constant strain rate are performed using displacement control. For each test, the displacement rate is held constant. Displacement is measured by the LVDT in the MTS machine. This measurement includes the deformation of steel platens and spacers, includes the machine frame deformation (although the frame is extremely stiff), and includes the deformation of each contact pair of specimen, platens, spacers and load cell. As a result, the strain rate calculated from the strain measured by strain gages on the specimen is not constant, especially at the beginning of loading (Fig. 3.11). The strain–time relation is not a perfectly straight line, as shown in Fig. 3.11. For the strain rate dependence study, we assume that it is accurate enough if we treat this relation as linear. Doing so simplifies the problem without loss of significance. The strain rate is calculated by taking the slope of the dashed line in Fig. 3.11, i.e. the strain rate is averaged over the full duration of the test.

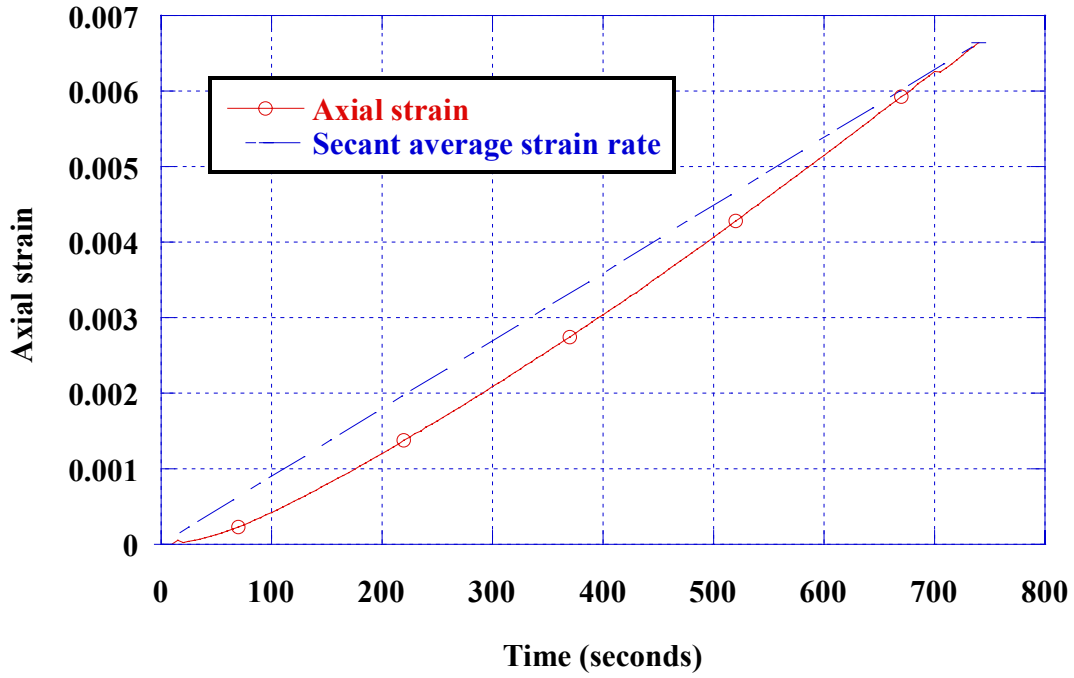

Figure 3.11 Typical axial strain versus time for a displacement rate controlled test. Secant average strain rate calculation.

3.6 Creep test

3.6.1 Test description

Fourteen specimens have been tested in uniaxial creep. The specimens were collected from the middle nonlithphysal (Tptpmn), lower lithophysal (Tptpll) and lower nonlithophysal (Tptpln) zones of the welded Topopah Spring Tuff formation. The specimens are selected so that they do not contain major lithophysae or visible fissures. Vapor-phase altered spots are common among the rock cores. Small vapor-phase altered inclusions are allowed in the specimens for creep testing. Fig. 3.12 shows two representative specimens used for creep testing, illustrating that a “flawless” specimen is

"flawless" only when compared to a lithophysal specimen, certainly not when compared to a uniform fine-grained limestone or granite.

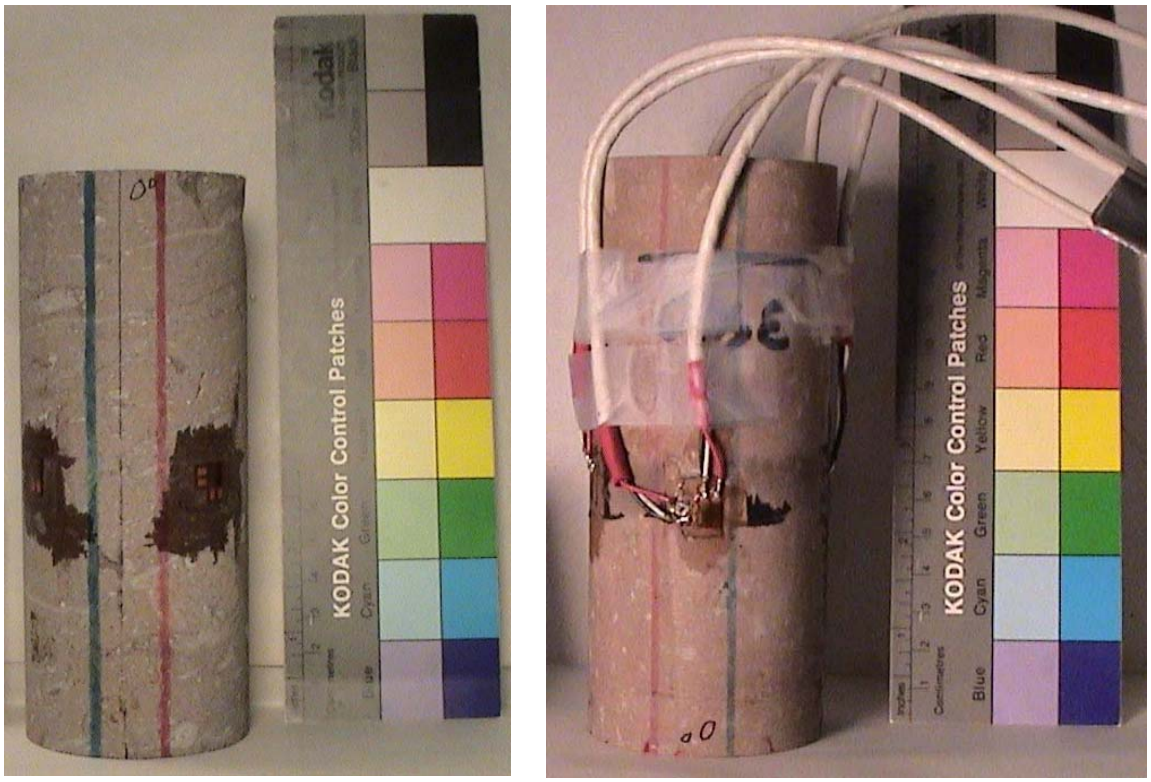

(a) (b)

Figure 3.12 Specimens for creep testing. (a): Specimen ID = 01014733-2-CU, nominal diameter = 2.4 inch (60.96 mm), from Tptpll. (b): Specimen ID =01023682-3-CU, nominal diameter = 2.4 inch (60.96 mm), from Tptpmn.

All the test specimens are cut to a ratio of length to diameter of 1.9 – 2.5 (Table 3.2), to approximately meet ASTM D 4543-85. Moisture contents have been measured after testing. Table 3.2 gives a summary of the test specimen geometries and moisture contents.

Strain is measured using 120-ohm electric resistance strain gages for all the tests. Six strain gages are used. Four measure axial strain. Two measure lateral strain. All strain gages are cemented at about midheight of the specimen (Fig. 3.12). Strain in each direction is calculated by taking the average of all measurements in that direction.

Thermocouples are used to monitor the temperature for most of the tests. Significant temperature variation is observed in some tests. The variation is also reflected by strain gage readings. The temperature variation comes from three sources: 1) alternation of days and nights; 2) accumulated heat generated by the testing machine; 3) unexpected adjustment of room air conditioning. Of the above, 1) accompanied all the tests. The 3) happened several times during the creep testing. Seasonal temperature change is not obvious. Temperature change impairs strain gage readings. Not only does it affect the strain gage itself, but it affects the test specimen as well. In fact, the temperature effect on specimens is more serious than the one on strain gages (this can be observed by checking extensometer measurements). The deformations of both specimen and strain gage are recorded by the strain gage measurement. Applying the temperature-correction equations provided by the manufacturer of the strain gages to correct the strain gage measurements only eliminates the part of temperature effect accounted for by the strain gages. As a consequence a complementary measure is adopted. Each load step is maintained for not less than three days. Then it is not difficult to get a reasonable curve fitting for strain rate to eliminate the effects of temperature cycles.

Table 3.2 Summary of test specimen geometry and moisture content of specimens used for creep testing.

Specimen ID	Diameter (in)	Length (in)	L/D ratio	Moisture content (%)	Zone
01014949-1-CU	2.39	5.95	2.5	0.29	Tptpmn
01014951-1-CU	2.39	5.93	2.5	0.32	Tptpmn
01014951-2-CU	2.39	4.55	1.9	0.30	Tptpmn
01014733-2-CU	2.40	5.92	2.5	0.25	Tptpll
01014756-1-CU	2.41	5.24	2.2	0.47	Tptpmn
01015022-1-CU	2.41	5.36	2.2	0.59	Tptpmn
01015022-2-CU	2.41	5.61	2.3	0.47	Tptpmn
01015465-CU	2.40	4.57	1.9	N/A	Tptpln
01023361-1-CU	1.78	4.21	2.4	0.41	Tptpmn
01023363-1-CU	1.78	4.14	2.3	0.45	Tptpmn
01023363-3-CU	1.78	4.05	2.3	0.42	Tptpmn
01023364-1-CU	1.78	4.15	2.3	0.43	Tptpmn
01023582-3-CU	2.40	5.71	2.4	0.72	Tptpmn
01023665-2-CU	2.40	4.89	2.0	0.71	Tptpmn
				Average: 0.45%	

3.6.2 Test results

A commonly recognized creep curve is shown in Fig. 3.13. Three stages describe the creep history: transient (primary), steady-state (secondary) and accelerating (tertiary) creep. In the transient creep, the specimen deforms at a decreasing strain rate. After this stage the strain rate tends to remain constant at a certain value, i.e. the test transits to the steady-state stage. When the deformation of the specimen reaches a critical threshold, the accelerating stage starts. After a short time, the specimen breaks.

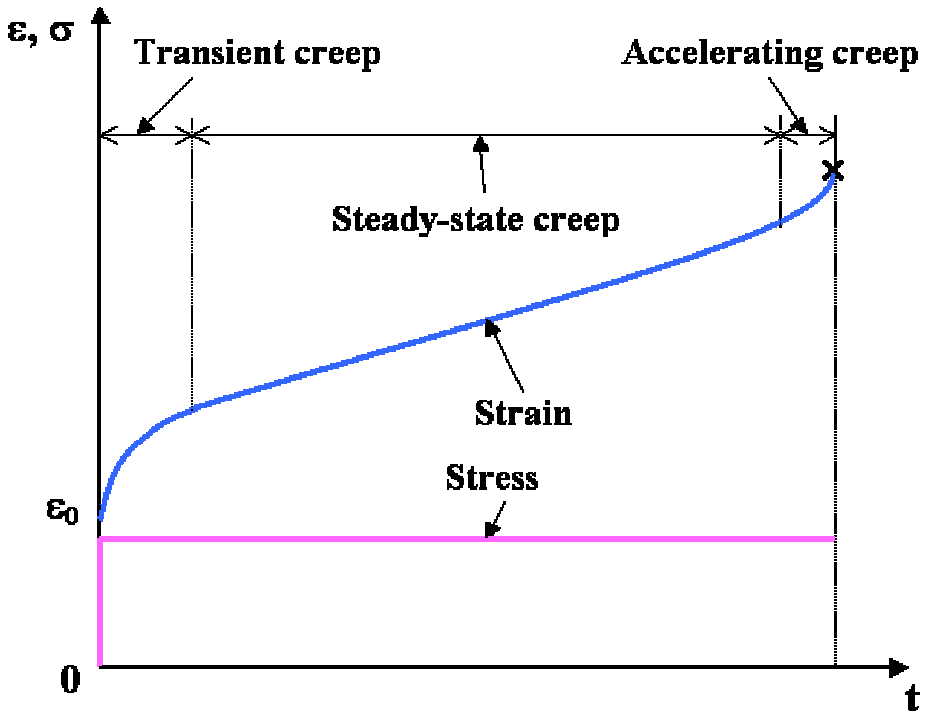

Figure 3.13 A commonly recognized creep curve (e.g. Jaeger and Cook, 1979, Fig. 11.1.1; Goodman, 1989, Fig. 6.16). Axial strain ε as a function of time t, constant axial stress σ

The Yucca Mountain tuffs under study break in a very brittle pattern and exhibit extremely variable peak strengths from specimen to specimen. It is difficult to predict the peak strength for a specific specimen. Thus it is difficult to complete a creep test in one stress level, because it is difficult to select a stress level that will assuredly give creep without instantaneously leading to failure. In this study, multiple stress levels are applied to each specimen until it fails. Each stress level is maintained for at least three days. The stress level increment ranges from 7 to 10 MPa. The tests took from 2 to 17 stress steps. The longest test lasted 1644.4 hours (68.5 days). Figs. 3.14 and 3.15 show two complete stress-time and strain-time curves for the tests 01023665-2-CU and 01023364-1-CU. The

strain-time and stress-strain curves for other tests are shown in Figs. B-1 through B-12 in Appendix B.

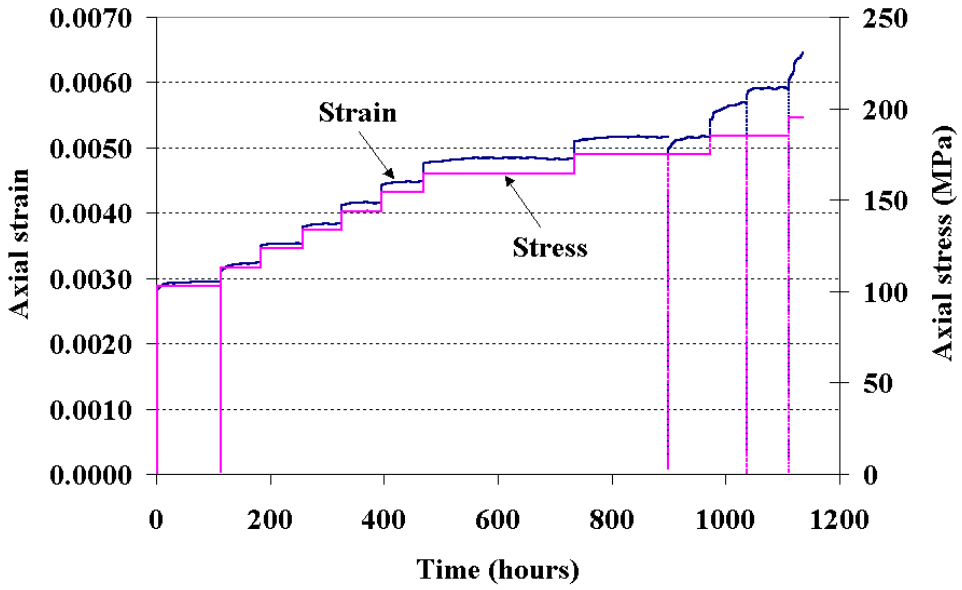

Figure 3.14 Experimental stress-time and strain-time curves for test 01023665-2-CU (from Tptpmn)

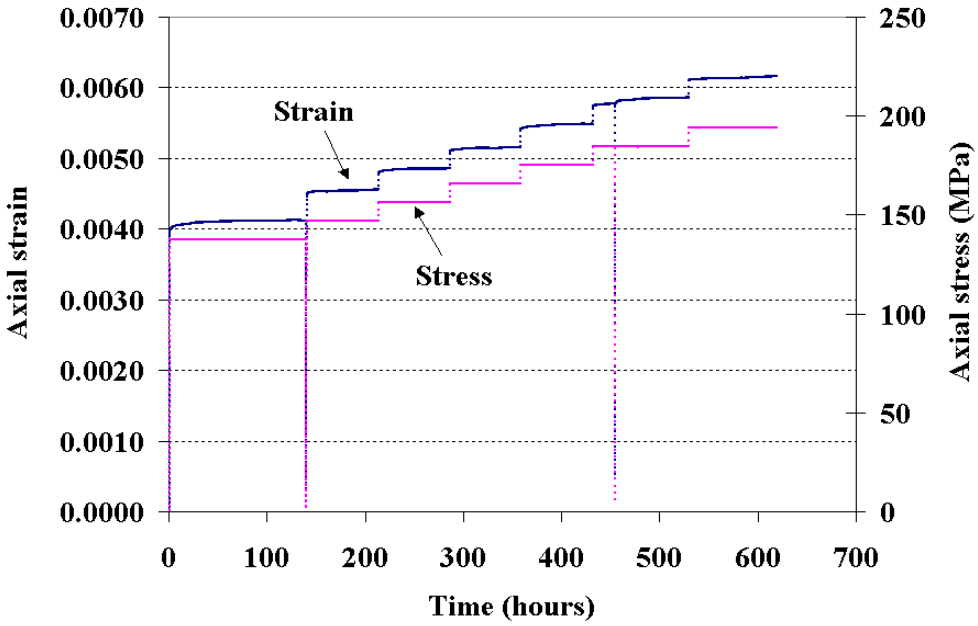

Figure 3.15 Experimental stress-time and strain-time curves for test 01023364-1-CU (from Tptpmn)

Table 3.3 lists time durations, number of stress levels, first stress levels and ultimate long term strengths for all the creep tests. As shown in Table 3.3, the first stress levels are set at from 30% to 90% of the ultimate strengths of the specimens.

Table 3.3 Summary of all the creep tests

Specimen ID	Test duration (hours (days))	Number of stress levels	First stress level (MPa)	Peak strength (MPa)	First stress level/Peak strength
01014949-1-CU	480.7 (20.0)	6	62.17	96.74	0.6
01014951-1-CU	510.7 (21.3)	6	62.01	89.65	0.7
01014951-2-CU	332.1 (13.8)	2	55.09	61.98	0.9
01014733-2-CU	73.4 (3.1)	2	93.19	103.53	0.9
01014756-1-CU	655.4 (27.3)	7	61.16	91.75	0.7
01015022-1-CU	1644.4 (68.5)	13	61.05	187.45	0.3
01015022-2-CU	232.0 (9.7)	2	61.14	152.98	0.4
01015465-CU	287.7 (12.0)	3	102	143.93	0.7
01023361-1-CU	213.3 (8.9)	4	93.74	112.47	0.8
01023363-1-CU	1206.3 (50.3)	13	93.79	168.77	0.6
01023363-3-CU	1609.6 (67.1)	17	87.49	187.49	0.5
01023364-1-CU	617.7 (25.7)	7	137.53	193.77	0.7
01023582-3-CU	637.0 (26.5)	7	159.67	200.79	0.8
01023665-2-CU	1132.9 (47.2)	12	102	195.29	0.5

CHAPTER 4 ANALYSIS OF CONSTANT STRAIN RATE TESTS

4.1 Study method for constant strain rate tests

All the specimens for constant strain rate testing to be studied in this chapter were collected from Alcove #5 which is located in the middle nonlithophysal zone (Tptpmn). Collecting the test specimens from a small area should increase the similarity in mechanical properties of the specimens. It has been shown in Chapter 3 that all the specimens in the time dependence study, including both the specimens tested at constant strain rate and the specimens tested in creep, showed brittle failure, and failed by axial splitting. Previous studies have strongly suggested that microfractures and pre-existing fractures dominate the failure of brittle rocks. The objectives of this chapter are to study the strain rate dependent strain and strain rate dependent strength of the tuff. To achieve this goal, strain rate dependence of the strength and the strain will be analyzed using a statistical method. Large variations in peak strength and peak axial strain from specimen to specimen have been presented in Chapter 3. It also has been shown that various flaws such as lithophysae, vapor-phase altered zones, fractures, etc are contained in the specimens either visible on the specimen surface or inside the specimen. Quantitatively investigating an influence of these flaws on specimen strength and maximum strain is difficult. Comparing the strengths of specimens with and without a certain type of flaw can be helpful to understand the influence of flaws. Random distribution of flaws could create a size effect among the specimens. For this reason, size effect on peak strength will be presented. All the specimens for constant strain rate testing have the same diameter,

2.4 inch (60.96 mm). Given the fixed diameter, size effect then becomes a length effect problem.

4.2 Influences of flaws and of specimen length on peak strength

For specimens that do not contain obvious flaws (called flawless hereafter), the usual failure mode is by axial splitting as shown in Figs. 3.9 and 3.10. After testing, undulating smooth fracture surface(s) are observed. Sometimes a crack propagation path is clearly visible. When breaking, flawless specimens generate large noise, shock and much dust. This indicates that much strain energy is released. When performing a high strain rate test, a specimen usually breaks into a large number of small approximately equal-sized pieces. This is especially true for high strength specimens.

For flawed specimens failure occurs in various ways. When a specimen contains a lithophysal cavity or a large vapor-phase altered zone, failure most likely starts from or around the flaw. If a specimen contains more than one lithophysal cavity, the largest one usually plays the decisive role in the failure.

Fig. 4.1 gives a comparison of the strengths of specimens with and without obvious lithophysal cavities, at the strain rate of $10^{-5} s^{-1}$. Each specimen for this plot classified as "with flaws" contains one or two visible cavities. The cavities are contained at about midheight of each specimen, and are oriented approximately along the axial direction

(Fig. 4.2). Their lengths range from 0.6 to 1.2 inch (15 to 30 mm). Their widths are small compared to their lengths.

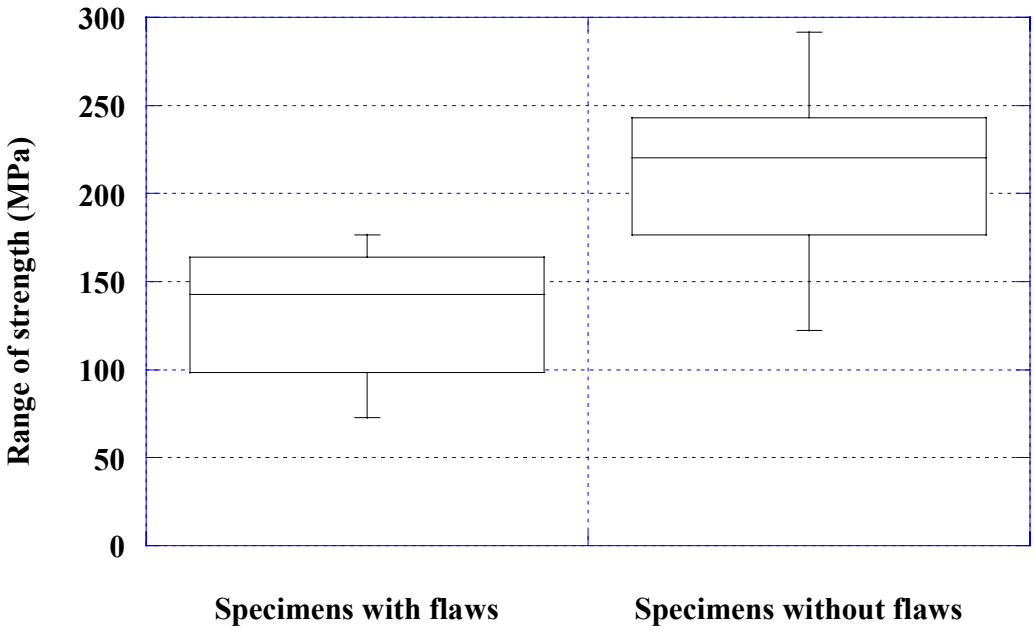

Figure 4.1 Strength of specimens with and without flaws, the former defined here as containing obvious lithophysal cavities with one dimension of at least about 0.6 inch (15 mm). Eleven specimens with flaws and twenty without flaws are used to construct this plot. The box plots give a five-number summary for each case: lowest, lower fourth, median, upper fourth and highest strength.

Figure 4.2 Specimens with flaws (cavities). Specimen IDs: 01025263-U, 01025231-2-U.

Specimen length affects strength. Fig. 4.3 shows a plot of strength versus ratio of length to diameter. The strength decreases with an increase in length. As already mentioned the specimens of various lengths are randomly grouped for strain rate dependence studies. It is assumed that the length effect from group to group is cancelled out.

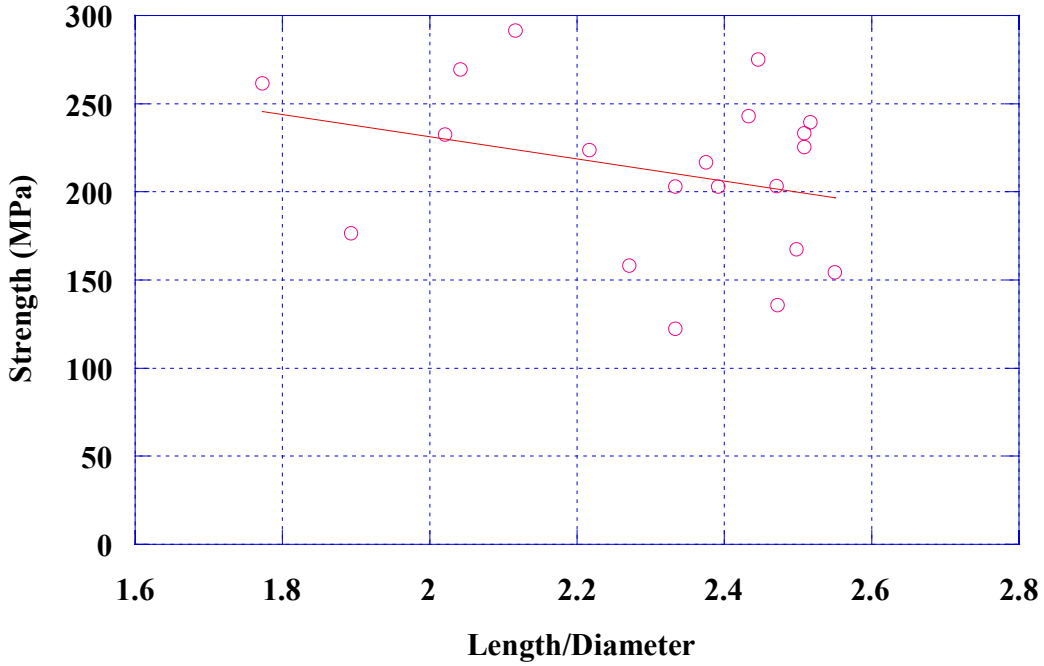

Figure 4.3 Size effect on uniaxial compressive strength

For a given strain rate, the peak strength is highly correlated to its corresponding peak axial strain. The correlation coefficient from specimens tested at a strain rate of $10^{-5}s^{-1}$ is as high as 0.95. As a result, the secant elastic moduli of the specimens evaluated at peak strength are much more constant than the strengths (Table 3.1). The peak strength of a specimen is mainly governed by peak axial strain. The peak axial strain is the value of the strain at the point of failure. The peak axial strain is influenced by the flaws in the specimen. Even for the specimens that do not contain obvious flaws, small or hidden ones affect their strength. With an increase in the volume of the specimen, the probability of containing hidden flaws in the specimen increases. This partially explains why the strength has a size effect (Hudson, 1993).

4.3 Stress-strain curves and their implications

Stress-strain curves reflect mechanical behavior of rocks. For brittle rocks, these curves can mirror pore/crack closure, crack growth, dilation and onset of failure during the course of loading. In investigations of brittle failure of rocks, a number of researchers divided the stress-strain curves into four or five regions in terms of their curvature changes (Brace et al., 1966; Bieniawski, 1967a; Lajtai and Lajtai, 1974). They believe that the beginning and progress of a particular deformational mechanism is reflected by the shape of a stress-strain curve through changes in the slope of the stress-strain curves. Fig. 4.4 shows curves of stress-axial strain, stress-lateral strain, stress-volumetric strain and stress-crack volumetric strain for specimen 01023662-2-U. Each curve is described below.

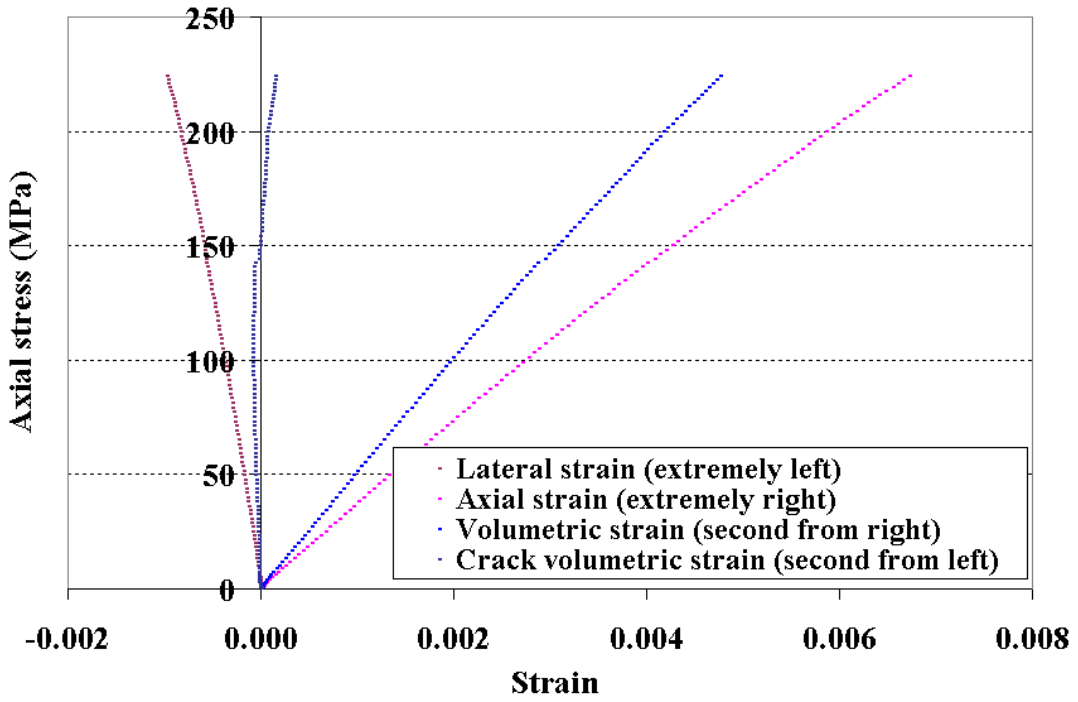

Figure 4.4 Axial stress versus axial strain, lateral strain, volumetric strain and crack volumetric strain for test 01023662-2-U (Test duration = 10.8 minutes; strain rate = $8.01\times10^{-6}\ \ s^{-1}$)

1) Stress-axial strain curve

Typically, three distinct parts can be observed in a stress-axial strain curve of a brittle rock specimen (Lajtai, 1998). The low stress part displays closure of pores and pre-existing cracks. If a specimen contains a significant volume of pores and pre-existing open cracks, the stress-axial strain curve is nonlinear and convex upward. The curve in Fig. 4.4 does not have this initial curved portion. It probably suggests that the tuff specimen has a low porosity and small volume of pre-existing open cracks. Up to well above 30-50% of peak strength, the curve appears linear. Within this range, the

pre-existing pores and open cracks have been closed if there are any, and the new cracks have not started. Young's modulus is normally defined as the slope of the curve in this linear range. ASTM D 3148 suggests that Young's modulus is estimated at about 50% of peak strength. Beyond the linear portion, the curve starts to depart from linearity. For brittle rocks, cracks start to form and grow at this stage. Consequently internal damage occurs in the specimen. If unloading is performed before the specimen fails, inelasticity can be read in the loading-unloading loop of the stress-axial strain curve. The curve in Fig. 4.4 does not show obvious nonlinearity, which indicates the linear elastic behavior of the tuff specimen. Let the axial strain be defined positive for compression. Axial strain is denoted as ε throughout this dissertation.

2) Stress-lateral strain curve

Lateral strain takes negative values for expansion. The more negative the lateral strain, the more expansion the specimen in lateral direction. The stress-lateral strain curve is normally unaffected by crack closure, but it is strongly influenced by the dilation of the axial cracks (Walsh, 1965; Lajtai, 1998). In brittle rocks, the position of crack initiation is identified at the first deflection of the initially linearly elastic portion of the stress-lateral strain curve (Lajtai and Dzik, 1996). Dilatancy resulting from crack opening under axial compression makes the axial stress-lateral strain curve deviate from linearity in the negative direction. Lateral strain is denoted as ε_l.

In Fig. 4.4, the stress-lateral strain curve appears nearly linear. This indicates that no or little dilatancy occurs in the specimen.

3) Stress-volumetric strain curve

Volumetric strain measures the volume change of a specimen. Following the sign convention used for axial and lateral strain, the volumetric strain takes a positive value if the volume of the specimen decreases. Under the assumption of small strain, volumetric strain is calculated by adding up the strains in three dimensions of the specimen (Brace et al., 1966; Sano et al., 1982; Martin and Chandler, 1994; Lajtai, 1998). For a cylindrical specimen, the volumetric strain is calculated as

$$\varepsilon_v = \frac{\Delta V}{V} = \varepsilon + 2\varepsilon_l \tag{4.1}$$

where ε_v = volumetric stain, ΔV = volume change, V = initial volume.

4) Stress-crack volumetric strain curve

The crack volumetric strain is derived from the volumetric strain curve by removing the elastic volume change and is calculated by

$$\varepsilon_{cv} = \varepsilon_v - \varepsilon_{ev} \tag{4.2}$$

where ε_{cv} = crack volumetric strain, ε_{ev} = elastic volumetric strain for a uniaxial compressive test, which is given by

$$\varepsilon_{ev} = \frac{1-2\upsilon}{E} \times \sigma \tag{4.3}$$

where E and v are Young's modulus and Poisson's ratio, respectively, σ is the axial stress.

The crack volumetric strain measures the cumulative volume of cracks. It inherits the sign convention of volumetric strain. Negative values represents axial cracks opening, or dilation. Positive value represents an event opposite to dilation, which could be closure of pre-existing open cracks (Lajtai. 1998) or compaction. The general shape of the crack volumetric strain curve reflects the interplay between the two opposite microscopic processes: axial crack opening (dilation) and pre-existing open crack closing (compaction). The stress-axial strain curve in Fig. 4.4 does not show pre-existing open cracks.

4.4 Dilatancy

Dilatancy is an important and typical feature in the failure behavior of most brittle rocks. Lac du Bonnet granite (Martin and Chandler, 1994; Lajtai, 1998), Westerly granite (Holcomb, 1978) and marble (Brace et al., 1966) show significant dilatancy with the growth of cracks in loading direction. Dilation can be observed in stress-lateral strain

curve. Dilatancy can also be indicated in stress-volumetric curve as the curve reverses towards the negative direction, as shown in Fig. 4.5.

Fig. 4.5 gives the stress strain diagram for a specimen. The lateral strain and volumetric strain curves indicate a weak dilatancy starting at half the strength. At near failure the dilatancy gets a little larger. Comparing the tuff with granite, the dilatancy is very small.

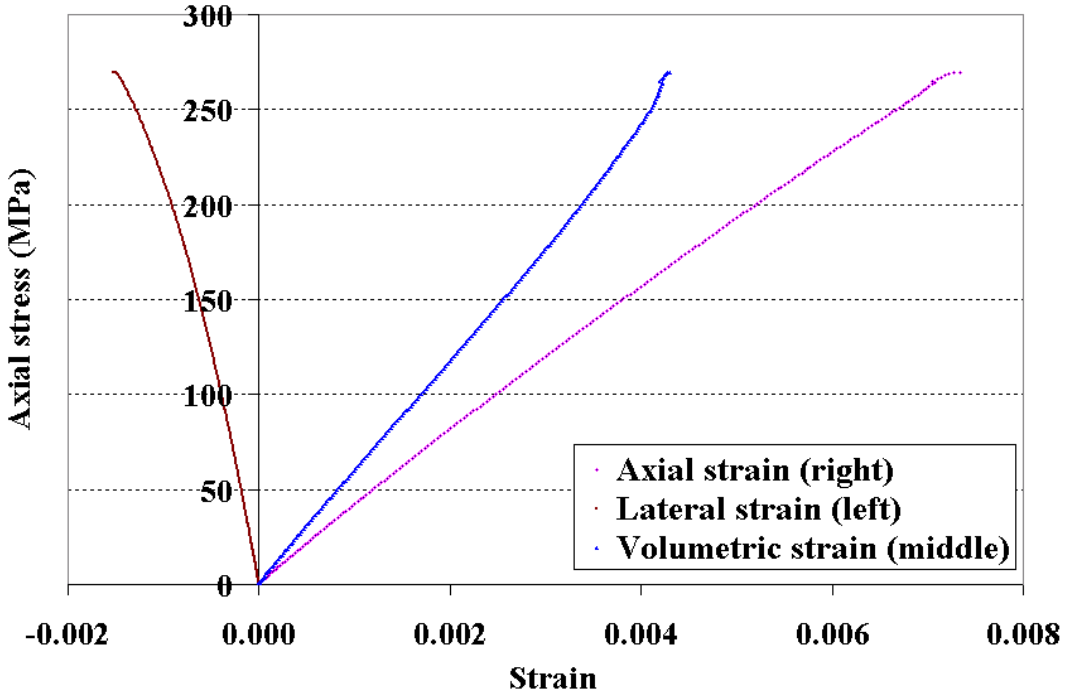

Figure 4.5 Axial stress versus axial strain, lateral strain and volumetric strain for a representative specimen showing slight dilatancy occurs during the test (Specimen ID: 01025230-2-U, peak strength = 269.62 MPa, strain rate = 10-5 s^{-1}).

4.5 Indication of crack initiation in stress-strain curves

Fig. 4.6 shows the stress strain diagram for Lac du Bonnet granite. As shown in the upper part of the figure, the four regions are defined as: Region I-crack closure, Region II-linear elastic deformation, Region III-crack initiation and stable crack growth, and Region IV-critical energy release and unstable crack growth.

Region I represents the closure of existing pores/microcracks in the rock specimen, which may or may not be present, depending on the initial pore volume/crack density. Once the existing pores/cracks are closed, the rock is presumed to be linearly elastic (Region II). The elastic properties of a rock specimen can be determined from this portion of the stress-strain curves. Crack initiation starts at the beginning of Region III. Crack initiation under axial compression is accompanied by crack dilation. Brace et al. (1966) find that dilation begins at a stress level of 30 to 50% of the peak strength of granite. The stress level at the beginning of Region III is referred to as the crack initiation threshold. The crack development in this region is considered as stable since its further development requires an increase of loading. The axial stress level where the total volumetric strain reversal occurs marks the beginning of Region IV and represents the onset of unstable crack growth. Bieniawski (1967a) finds that this reversal point occurs at about 80% of the short term peak strength for norite and quartzite. At this stress level the stress-axial strain curve clearly departs from linearity.

In a study of Lac du Bonnet granite, Martin (1993) proposed a plot of crack volumetric strain versus axial strain (cited by Martin and Chandler, 1994) as shown in the lower part of Fig. 4.6. This conceptual plot was later adopted by Eberhardt et al. (1998). They believe that the crack initiation stress can be determined using this plot.

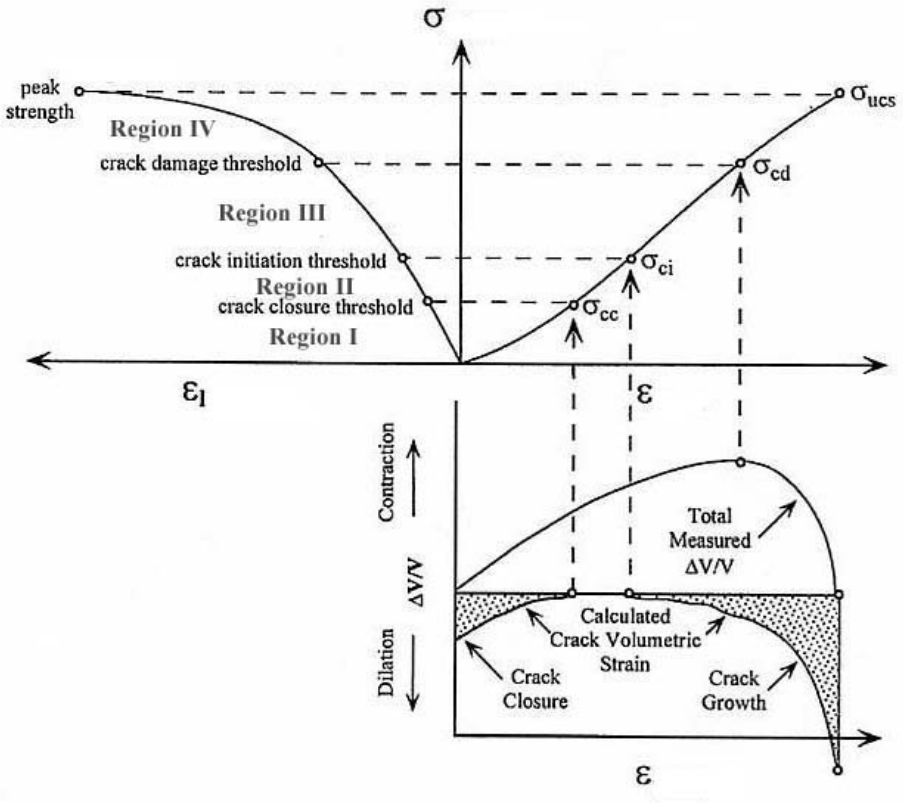

Figure 4.6 Stress-strain diagram showing the elements of crack development (after Martin, 1993). Note that only the axial strain (ε) and lateral strain (ε_l) are measured; the volumetric strain and crack volumetric strain are calculated. σ = axial stress; σ_{ucs} = peak strength; σ_{cd} = stress level at the beginning of Region IV where the crack damage or unstable crack propagation starts; σ_{ci} = crack initiation threshold; σ_{cc} = crack closure threshold; ΔV = change in volume; V = initial volume. This diagram is modified from Eberhardt et al., 1998.

In Fig. 4.6, the crack volumetric strain-axial strain curve reverses at the end of Region II. The reversal point is thought of as the beginning of crack initiation. This method has not been accepted widely. One drawback is that the calculation of elastic volumetric strain is very sensitive to the values of Young's modulus and Poisson's ratio. In the current study of Yucca Mountain tuff, a similar procedure has been applied. The only variation made here is using crack volumetric strain versus axial stress instead of axial strain. The purpose for this variation is to observe the development of crack volumetric strain along the course of axial stress. Three distinct shapes of crack volumetric strain-axial stress curves are obtained and discussed below.

Case 1 Stress-crack volumetric strain curve reverses to negative direction

Fig. 4.7 gives axial stress versus axial strain, lateral strain, volumetric strain and crack volumetric strain for test 01025226-1-U, which sustained an increasing load for 15.3 hours. The stress-axial strain curve is quite linear, especially at low stress. Above about 100 MPa, the curve goes slightly nonlinear with downward bending. A clear nonlinearity in the stress-lateral strain can be observed, but it is much less than for the Lac du Bonnet granite shown in Fig. 4.6. Beyond about 100 MPa level the curve departs from linearity faster. This phenomenon may indicate that a certain degree of crack dilatancy occurs after at above 100 MPa. The stress-volumetric strain curve does not show the reversal point. The stress-crack volumetric strain reverses at about 100 MPa. To demonstrate this reversed curve clearer, Fig. 4.8 is given with an increased scale along the horizontal axis.

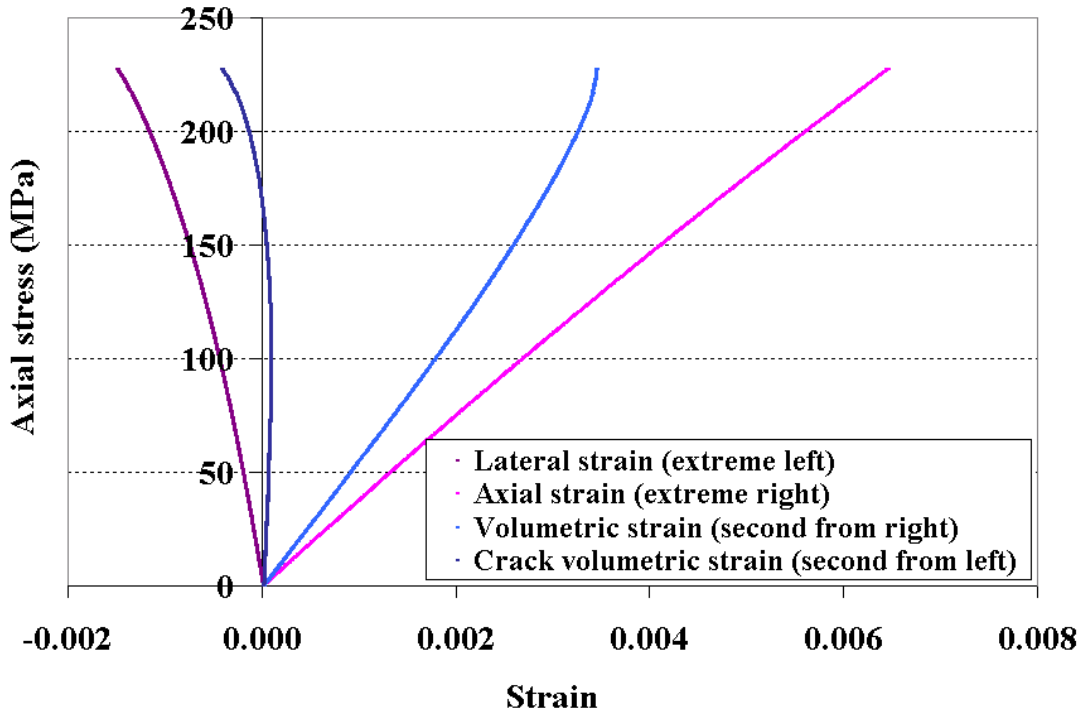

Figure 4.7 Axial stress versus axial strain, lateral strain, volumetric strain and crack volumetric strain for test 01025226-1-U (test duration = 15.3 hours; strain rate = $1.17 \times 10^{-7}\ s^{-1}$)

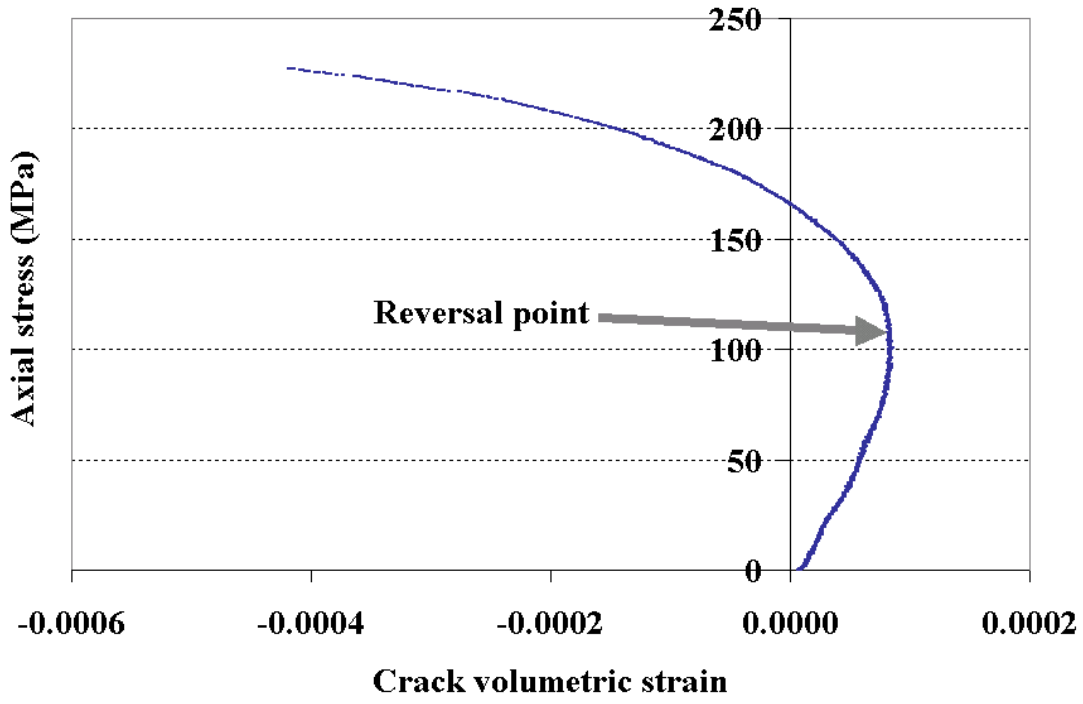

Figure 4.8 Axial stress versus crack volumetric strain for test 01025226-1-U (test duration = 15.3 hours; Strain rate = $1.17 \times 10^{-7}\ s^{-1}$)

The crack volumetric curve is initially positive, goes through the reversal point, and finally ends with a negative value (dilation). The reversal point on the stress-crack volumetric strain curve occurs at about 108 MPa. Taking the explanation by Martin and Chandler (1994) and Eberhardt et al. (1998) to the reversal phenomenon, it can be judged that crack dilatancy starts at the 108 MPa, which implies that the crack initiation takes place at this stress.

Case 2 Stress-crack volumetric strain curve reverses to positive direction

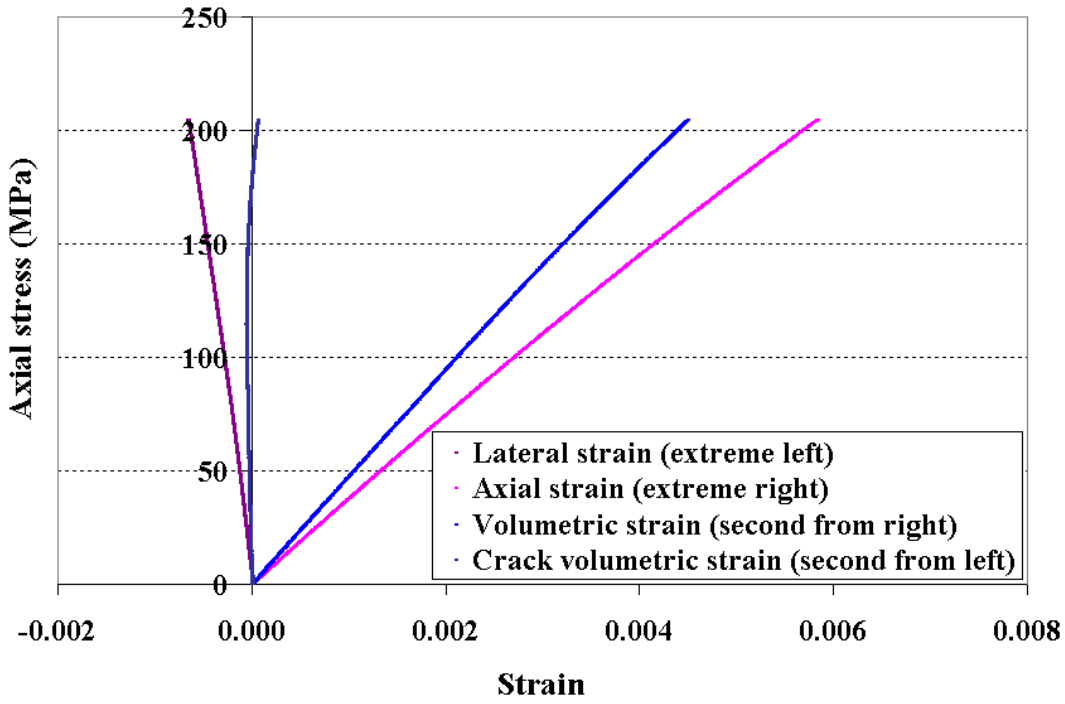

Figure 4.9 Axial stress versus axial strain, lateral strain, volumetric strain and crack volumetric strain for test 01023662-1-U (test duration = 15.8 hours; strain rate = $1.17\times10^{-7}\ \ s^{-1}$)

Compared with Fig. 4.7, the stress-lateral strain curve shown in Fig. 4.9 for test 01023662-1-U exhibits much more linearity. Very little indication is given of dilatancy. The stress-volumetric strain curve is slightly concave to the right. It is interesting that the stress-crack volumetric strain curve changes in the opposite direction from the test 01025226-1-U shown in Figs. 4.7 and 4.8. The reversal point on the curve is at about 115 MPa (Fig. 4.10). The stress level where the stress-crack volumetric strain curve reverses is very close to the test in case 1.

According to the explanation by Martin and Chandler (1994) and Eberhardt et al. (1998), the specimen must have a relatively large deformation in the axial direction compared to the lateral deformation. The specimen is compacted. Dilation does not occur or is too small to be observed. Lajtai (1998) suggests that compaction entails permanent damage along grain boundaries that are under high compression. During compaction, the permanent crack volume becomes positive (compression).

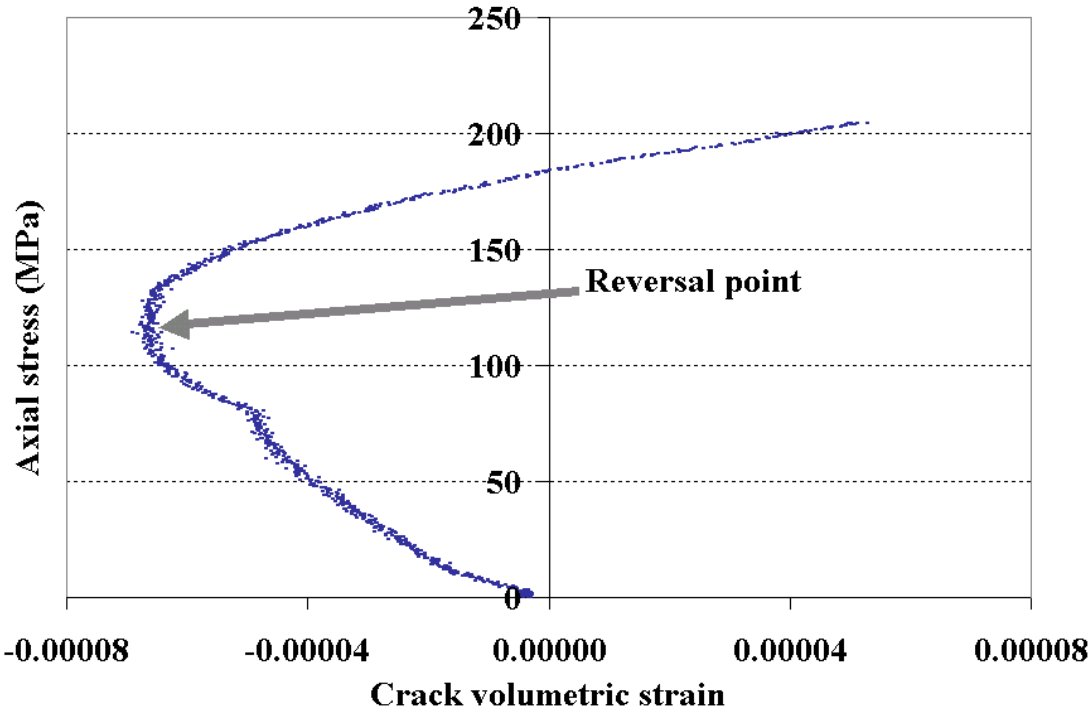

Figure 4.10 Axial stress versus crack volumetric strain for test 01023662-1-U (test duration = 15.8 hours; strain rate = $1.17 \times 10^{-7}\ s^{-1}$)

Case 3 Stress-crack volumetric strain curve reverses to negative and then to positive direction

In Fig. 4.11, both stress-axial strain curve and stress-lateral strain curve appear clearly nonlinear compared to the curves in Fig. 4.9. Most interestingly, the stress-crack volumetric strain curve reverses twice: it is initially positive, goes through the first reversal point, then turns to negative (dilation), reverses again and goes to the second reversal point, and finally ends with a positive value (compaction). The first reversal point is at about 120 MPa. The second reversal point is at about 225 MPa, which is about 92% of the peak strength of the specimen. The first reversal point has the same meaning as the one in case 1. What does the second reversal point mean? One possibility is that the second reversal point indicates the onset of failure. At that stress level the specimen matrix has been broken.

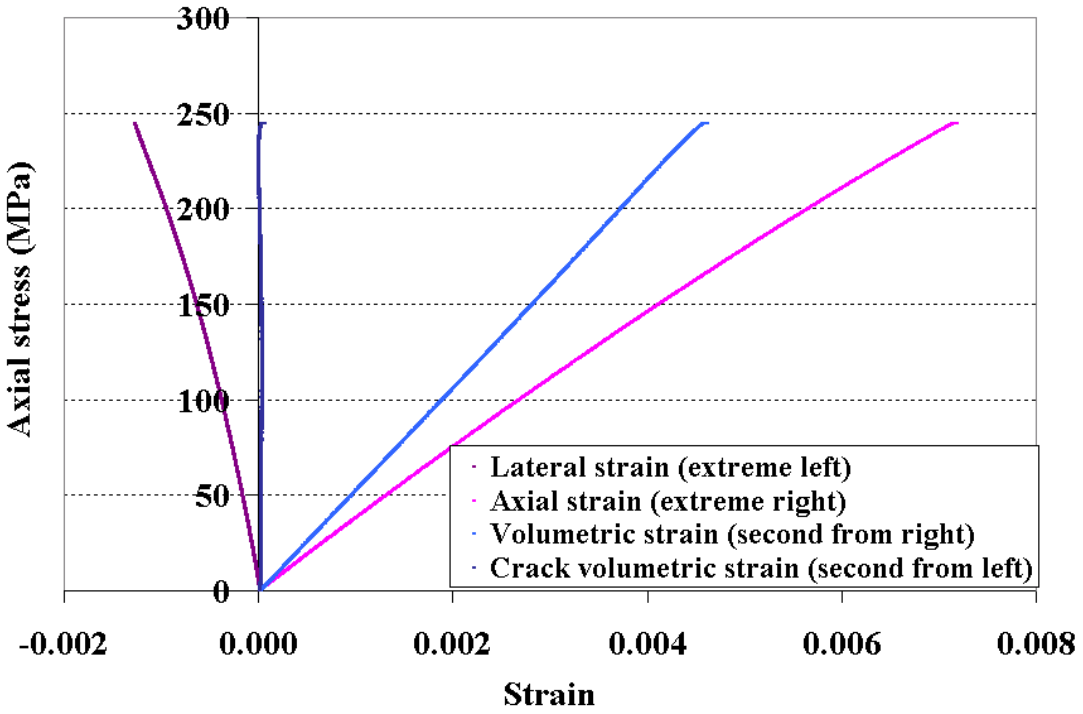

Figure 4.11 Axial stress versus axial strain, lateral strain, volumetric strain and crack volumetric strain for test 01023694-2-U (Test duration = 1.7 hours; strain rate = $1.17 \times 10^{-6}\ \ s^{-1}$)

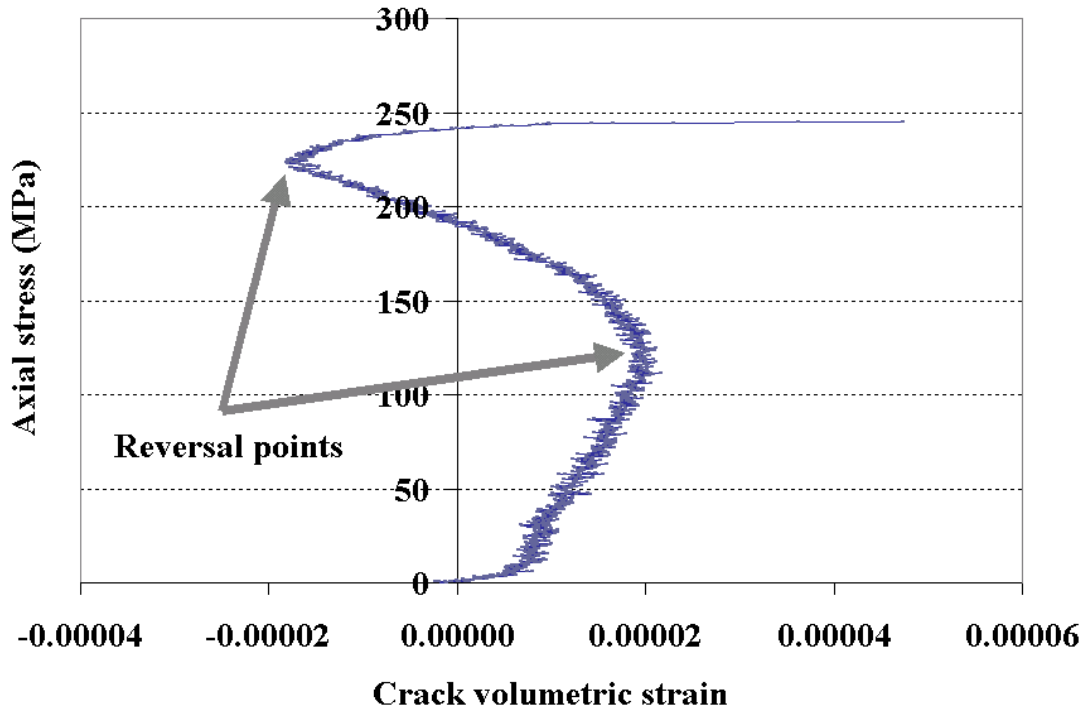

Figure 4.12 Axial stress versus crack volumetric strain for test 01023694-2-U (Test duration = 1.7 hours; strain rate = $1.17 \times 10^{-6}\ s^{-1}$)

Stress-crack volumetric strain curves for 17 tests have been determined. The reversal stress level and the reversal direction for each test are summarized in Table 4.1. The radio of reversal stress to peak strength for each test is also shown in the table. It can be seen that this ratio does not change much from test to test. The mean value is 0.52 and the standard deviation is 0.09. To see the strain rate dependence of this ratio, a plot is given in Fig. 4.13.

Table 4.1 Summary of reversal stresses for 17 tests

Specimen ID	Reversal stress (MPa)	Strength (MPa)	$\frac{ReversalStress}{Strength}$	Reversal direction	Test duration (hours)	Average Strain Rate
01023580-U	105	172.00	0.61	Pos. to Neg,*	1.32	1.10E-06
01023662-2-U	105	203.36	0.52	Neg. to Pos.	0.18	8.01E-06
01025224-1-U	102	209.32	0.49	Neg. to Pos.	0.01	1.16E-04
01025225-2-U	80	217.53	0.37	Neg. to Pos.	0.02	1.01E-04
01025224-3-U	80	154.49	0.52	Neg. to Pos.	0.15	9.47E-06
01025230-2-U	140	269.62	0.52	Neg. to Pos.	0.19	1.07E-05
01025259-1-U	175	238.26	0.73	Neg. to Pos.	1.90	1.04E-06
01025230-1-U	120	209.46	0.57	Neg. to Pos.	1.65	1.31E-06
01023694-2-U	120	244.80	0.49	Pos. to Neg,	1.70	1.17E-06
01023662-1-U	115	204.55	0.56	Neg. to Pos.	15.77	1.03E-07
01025226-1-U	105	227.37	0.46	Pos. to Neg,	15.32	1.17E-07
01023706-1-U	115	199.89	0.58	Neg. to Pos.	72.33	2.53E-08
01023751-1-U	60	176.95	0.34	Pos. to Neg,	13.13	1.09E-07
01025227-1-U	100	189.27	0.53	Neg. to Pos.	0.00	6.85E-04
01025232-1-U	105	215.84	0.49	Neg. to Pos.	0.00	4.63E-03
01023695-2-U	105	203.02	0.52	Neg. to Pos.	0.15	1.07E-05
01023760-2-U	80	158.24	0.51	Pos. to Neg,	0.01	9.22E-05

* Neg. = Negative, Pos. = Positive.

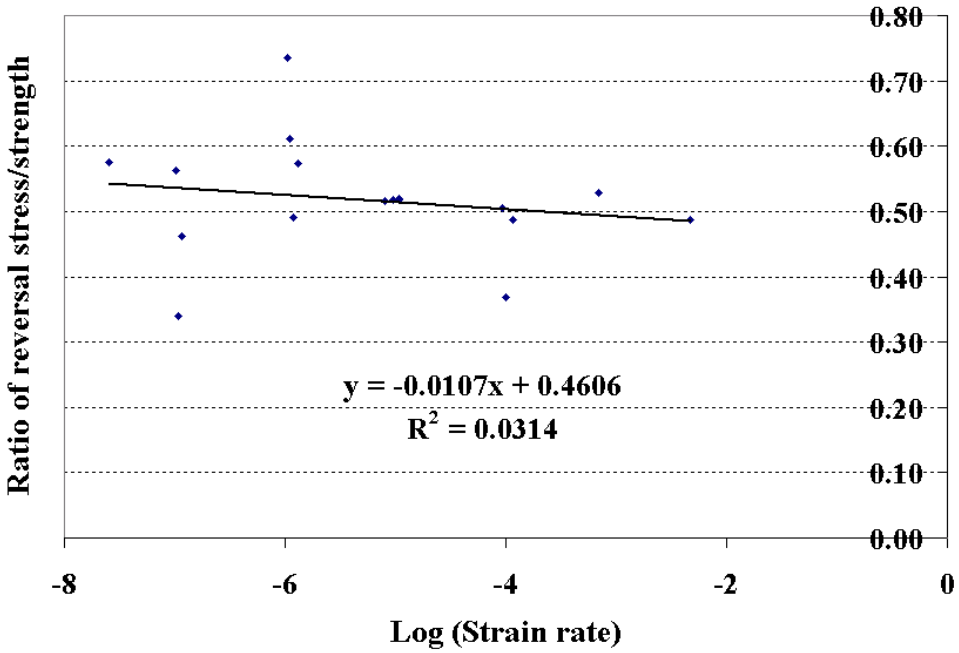

Figure 4.13 Ratio of reversal stress to peak strength for each test as a function of logarithm of strain rate (t-test for the slope of the fitting line = -0.7, p-value = 0.5).

The fitting line in Fig. 4.13 indicates that the influence of strain rate on the ratio of reversal stress to peak strength is not statistically significant. The t-test and p-value for the slope of the fitting line are -0.7 and 0.5, respectively. Three points deviate significantly from the fitting line. All other points stay around the fitting line. Therefore they support the strain rate dependency well. If the three points which deviate significantly from the fitting line are removed, the t-test and p-value for the slope of the fitting line become –1.6 and 0.15, respectively.

From Table 4.1, 29% (5 of 17) of the tests have the stress-crack volumetric strain curve reversing from positive to negative direction (dilation) and 71% (12 of 17) do the

opposite (compaction). This means that 71% of the tests reverse their stress-crack volumetric strain curve oppositely to Lac du Bonnet granite (Martin and Chandler, 1994). The Yucca Mountain tuff has a much smaller dilation before failure. This can be seen from Figs. 4.5. All the tuff specimens in this study were collected from the same location (Alcove #5) at Yucca Mountain site. Why do they show different behaviors? This is a matter of microstructure. Some rock specimens dilate more than others. It is the microstructures in rock specimens that influence the dilation or compression.

Recognizing the dilatancy of the Yucca Mountain tuff helps understand what occurs in rock specimens. This is not the final goal for this section. The most important conclusion from the above analysis is that the stress-crack volumetric curves for all the tests have very close reversal stress levels: average 52% of peak strength.

The fact that the stress-crack volumetric strain curve for test 01023594-2-U reverses twice should not be ignored. The second reversal stress may indicate unstable crack propagation. This phenomenon will be discussed later.

The above analysis does not show much dilation in tuff specimens before failure. However, the specimens do fail by axial splitting (Figs. 3.7 and 3.8). These seemingly contradictory findings may be explained as: the specimens have relatively high cohesion. They do not show large dilation before failure.

4.6 Near failure feature in axial stress-axial strain curve

To explore the near failure behavior of the tuff specimens, stress-axial strain curves for all the 65 specimens used for strain rate dependence study have been plotted and examined. A clear stress drop in the stress-axial strain curve near failure is observed in 26 specimens. Fig. 4.14 shows four of them. Table 4.2 gives a summary of stress drop points in stress-axial strain curve at near failure stage for 26 tests

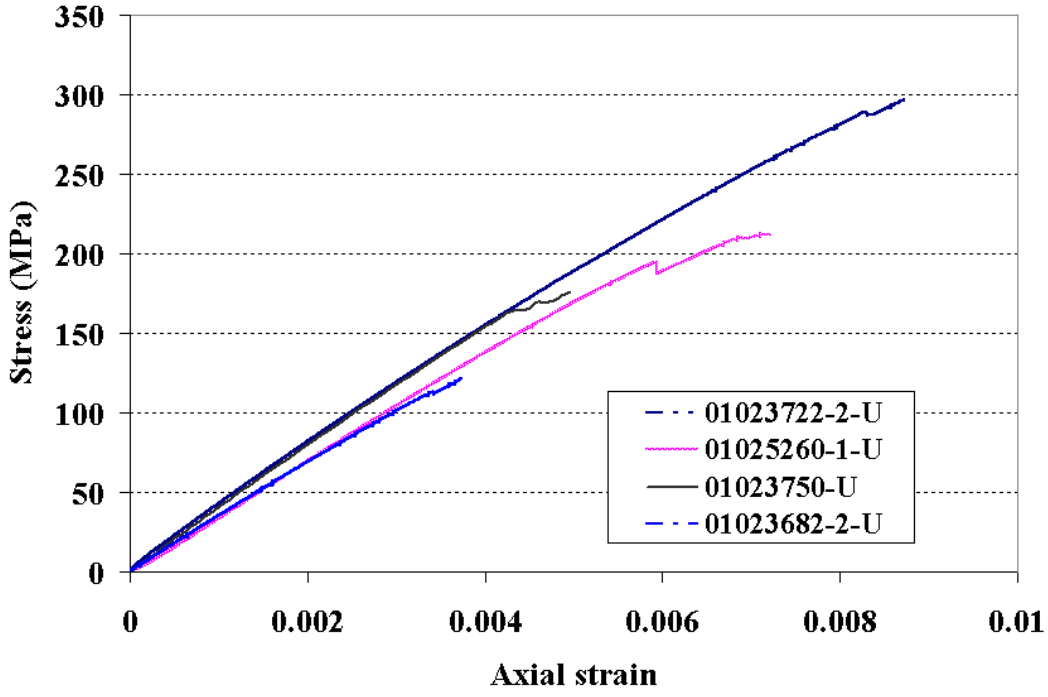

Figure 4.14 Stress-axial strain curves showing stress drop before ultimate failure, which may be the indication of unstable crack propagation. Specimen 01023722-2-U: peak strength = 296.47 MPa, strain rate = $1.23\times10^{-6}\ s^{-1}$; Specimen 01025260-1-U: peak strength = 212.17 MPa, strain rate = $1.18\times10^{-6}\ s^{-1}$; Specimen 01023682-2-U: peak strength = 121.15 MPa, strain rate = $1.02\times10^{-7}\ s^{-1}$; Specimen 01023750-U: peak strength = 176.52 MPa, strain rate = $1.15\times10^{-5}\ s^{-1}$.

Table 4.2 Summary of stress drop points in stress-axial strain curve at near failure stage for 26 tests

Specimen ID	Stress drop point (MPa)	Peak strength (MPa)	$\frac{StressDropPoint}{PeakStress}$
01023582-1-U	184.99	202.98	0.91
01023580-U	164.33	172.00	0.96
01023576-2-U	114.83	128.59	0.89
01023668-3-U	101.67	113.21	0.90
01023697-1-U	206.58	215.19	0.96
01023662-2-U	189.79	203.36	0.93
01023689-2-U	215.03	228.02	0.94
01023692-U	205.36	213.68	0.96
01023690-1-U	224.58	248.61	0.90
01025225-1-U	188.16	196.68	0.96
01023703-2-U	206.06	214.41	0.96
01025259-1-U	225.84	238.26	0.95
01023722-2-U	288.32	296.47	0.97
01025234-1-U	277.34	291.64	0.95
01023702-2-U	212.41	223.90	0.95
01023707-1-U	171.55	192.01	0.89
01025260-1-U	194.81	212.17	0.92
01023682-2-U	112.79	121.15	0.93
01023706-1-U	189.38	199.89	0.95
01023707-3-U	220.73	232.55	0.95
01023747-1-U	250.89	264.26	0.95
01023747-3-U	199.96	210.88	0.95
01023750-U	163.25	176.52	0.92
01023760-2-U	145.68	158.24	0.92
01025233-1-U	192.56	197.48	0.98
01025232-1-U	190.10	215.84	0.88
Mean = 0.936; Standard deviation = 0.0263; 95% Confidence Interval: 0.883 - 0.988			

The mean of the ratio of stress drop point to peak strength is 0.936. It is interpreted as that on average when the axial stress reaches 93.6% of the peak strength, the axial stress drops. This stress drop indicates that internal damage has occurred in the specimen. The internal damage may in turn indicate unstable crack propagation started. The stress drop point may have the same meaning as the second reversal point in Fig. 4.12. Scholz

(1968a) finds that microfracturing due to the propagation of cracks typically begins at about half the breaking strength and accelerates steadily until about 90 – 95% of its breaking strength for granite. There is no marked tendency for the ratio of stress drop point to peak strength to increase or decrease with strain rate.

4.7 Strain rate dependence

For a fast-loading test, the peak axial strain is composed of linear and nonlinear elastic strain. The permanent deformation is extremely small. Let ε_e represent axial elastic strain which includes both linear and nonlinear elastic strains. Let ε_{in} represent all types of inelastic axial strain even though those are very small. The peak axial strain for fast-loading tests can be expressed as

$$\varepsilon_{peak} = \varepsilon_e + \varepsilon_{in} \tag{4.4}$$

To study strain rate dependence, three parameters are evaluated: peak strength, corresponding peak axial strain and secant modulus measured at peak strength. Secant modulus is used as a tool to help describe the stress-strain relation. Secant modulus is measured at failure in a specimen. Therefore secant modulus directly links peak strength and peak axial strain. As described in Section 4.2, for the tests at strain rate $10^{-5}\ s^{-1}$, the tuff specimens exhibit high correlation between peak strength and peak axial strain. The correlation may be lower for different strain rates due to the strain rate dependence. Observations show that with a decrease in strain rate, the peak strength does not decrease

proportionally with a decrease of peak axial strain, but at a faster rate. Secant modulus can serve as an excellent parameter to count this. Beyond the linear period, internal damage starts. The internal damage is strain rate dependent (Lemaitre, 1992). Secant modulus can be an appropriate damage variable to describe the strain rate dependent internal damage of a specimen, which is presented in Section 4.8.

Peak strength, peak axial strain and secant modulus for the sixty five specimens subjected to constant strain rate tests have been measured and calculated. Scatter plots between each of these parameters and strain rate are shown in Figs. 4.15-4.17. Nonlinear regression is applied to estimate the relations between peak strength and strain rate, peak axial strain and strain rate, as well as secant modulus and strain rate. A call file for nonlinear regression in SAS, PROC NLIN, programmed by Professor George Fernandez who is in the Department of Applied Economics and Statistics, University of Nevada, Reno and also in the author's Doctoral Advisory Committee, is used for the regression analysis. All three relations are best represented by power functions. Three estimated equations are listed as Eqs. 4.5-4.7. Statistics for the regression equations are listed in Tables 4.3-4.5. Regression curves and 95% confidence bands for each of the three relations are added in Figs. 4.15-4.17.

The regression analyses are conducted in two steps: 1) each pair of data samples is transformed to a linear relation using log-transformation. The best relation between each pair of linear-transformed data samples is selected based on the minimum MSE (Mean Squared Error) criterion (Neter et al. 1996; Fernandez, 2003), and 2) nonlinear regression

is performed on each pair of untransformed data samples based on the relation chosen in 1). This step is to estimate the parameters and verify the pre-selected relation.

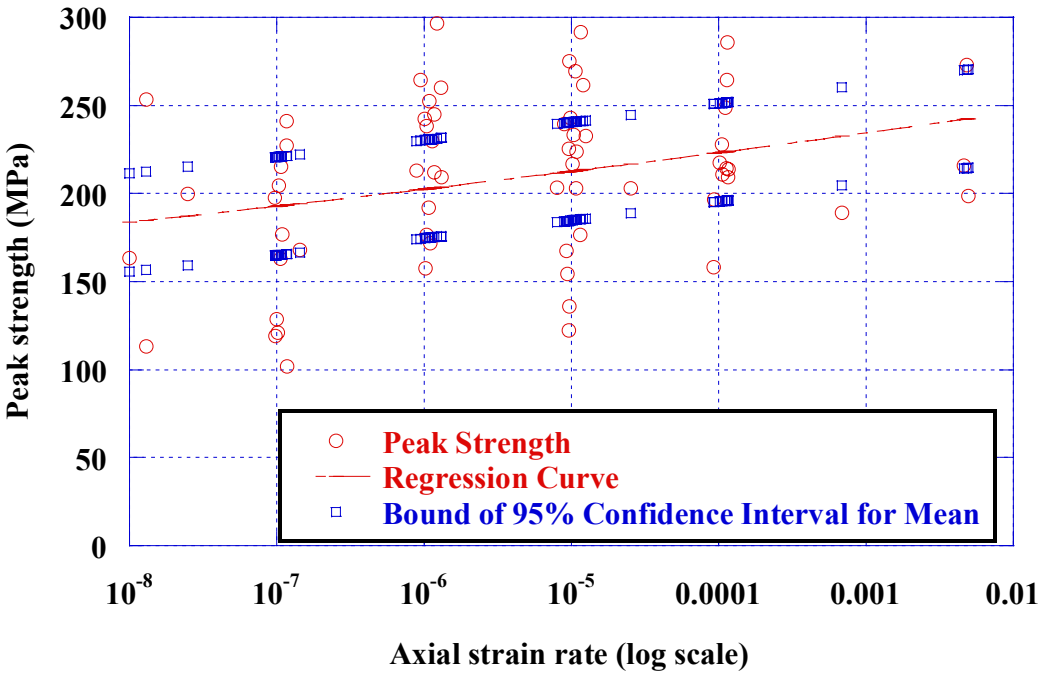

Figure 4.15 Peak strength versus strain rate with best regression line and 95% confidence bands.

Table 4.3 Statistics for regression of σ_{peak} on $\dot{\varepsilon}$

Variable	Estimate	Standard Error	t-value	Pr > |t|
Coefficient	2.44988	28.3422	9.57	<.0001
Exponent	0.02626	0.00837	2.54	0.0136

$$\sigma_{peak} = 271.37\dot{\varepsilon}^{0.0212} \tag{4.5}$$

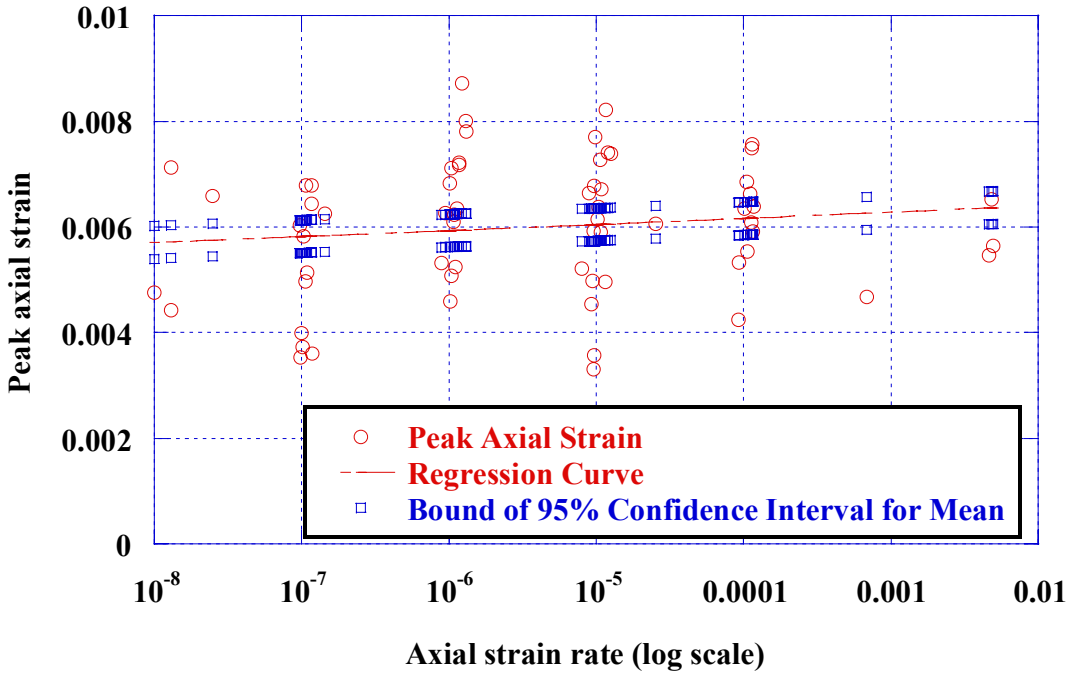

Figure 4.16 Peak axial strain versus strain rate with best regression line and 95% confidence bands.

Table 4.4 Statistics for regression of ε_{peak} on $\dot{\varepsilon}$

Variable	Estimate	Standard Error	t-value	Pr > |t|
Coefficient	0.006645	0.000698	9.53	<.0001
Exponent	0.00825	0.00826	1.00	0.3215

$$\varepsilon_{peak} = 0.0066\dot{\varepsilon}^{0.0083} \tag{4.6}$$

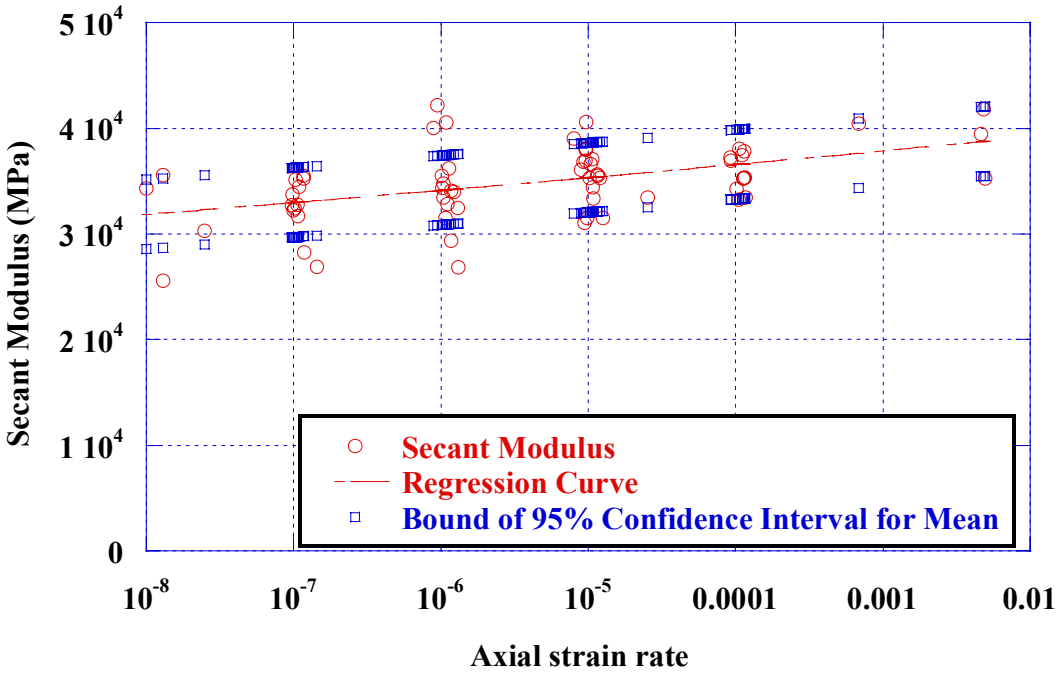

Figure 4.17 Secant modulus versus strain rate with best regression line and 95% confidence bands.

Table 4.5 Statistics for regression of E_S on $\dot{\varepsilon}$

Variable	Estimate	Standard Error	t-value	Pr > |t|
Coefficient	41985.38	1824.9	23.01	<.0001
Exponent	0.015035	0.00345	4.36	<.0001

$$E_S = 41985.4\dot{\varepsilon}^{0.015} \tag{4.7}$$

The t-tests and p-values indicate that at 95% confidence level, $\dot{\varepsilon}$ has significant influence on σ_{peak} (t-test = 2.54, p-value = 0.0136 < 0.05) and E_S (t-test = 4.36, p-value < 0.0001), but not on ε_{peak} (t-test = 1, p-value = 0.3215 > 0.05). This means that the determined

relations between peak strength and strain rate as well as between secant modulus and strain rate are significant. The relation between peak axial strain and strain rate is not.

4.8 Long term strain analysis

Estimated equations (Eqs. 4.5-4.7) and regression curves in Figs. 4.15-4.17 suggest that peak strength, peak axial strain and secant modulus all decrease with a decrease of strain rate $\dot{\varepsilon}$ in a power function. Based on these relationships, the following assumption can be made: if a specimen could be tested repeatedly and tested at different strain rates, a group of axial stress-axial strain curves shown in Fig. 4.18 would be obtained. Each curve in the diagram represents the stress-strain relation at a specific strain rate. The dashed lines represent secant moduli. With the decrease in strain rate, the peak strength, peak axial strain and secant modulus all decrease.

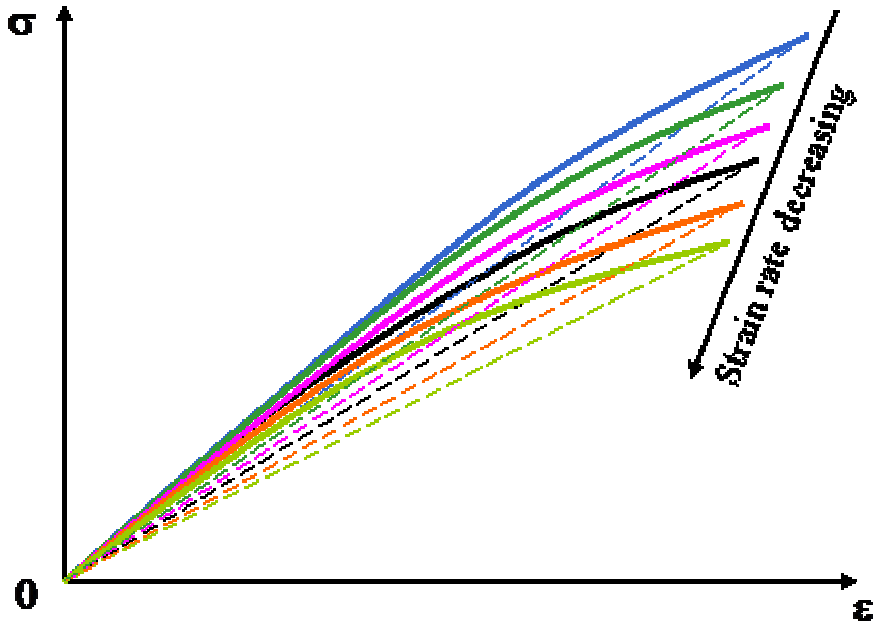

Figure 4.18 Schematic diagram showing the postulated peak strength, peak axial strain and secant modulus decrease with a decrease of strain rate.

Given the concept in Fig. 4.18, a diagram is constructed to decompose a strain component caused by strain rate effect from total axial strain (Fig. 4.19). Assume a specimen has experienced a fast loading test or short term test (high strain rate). Its stress-strain curve is shown as *O*-*A* in Fig. 4.19. If it experienced a slow loading test or long-term test (low strain rate), the stress-strain curve would be *O*-*B*. Compared with the short-term test, it would suffer a reduction in peak stress, σ_{loss}, a reduction in peak axial strain, ε_{loss}, and a secant modulus reduction. The secant modulus reduction is the difference in slopes between dashed lines *O*-*A* and *O*-*B*. From Fig. 4.19, it can be seen that σ_{loss} is not caused by ε_{loss} alone, but is caused by a strain component between *B* and *C* as well. This strain component is strain rate effected. It is caused by strain rate dependent internal

damage. So it is denoted by ε_{damage}. This component is reflected in the secant modulus reduction indicated in Fig. 4.17.

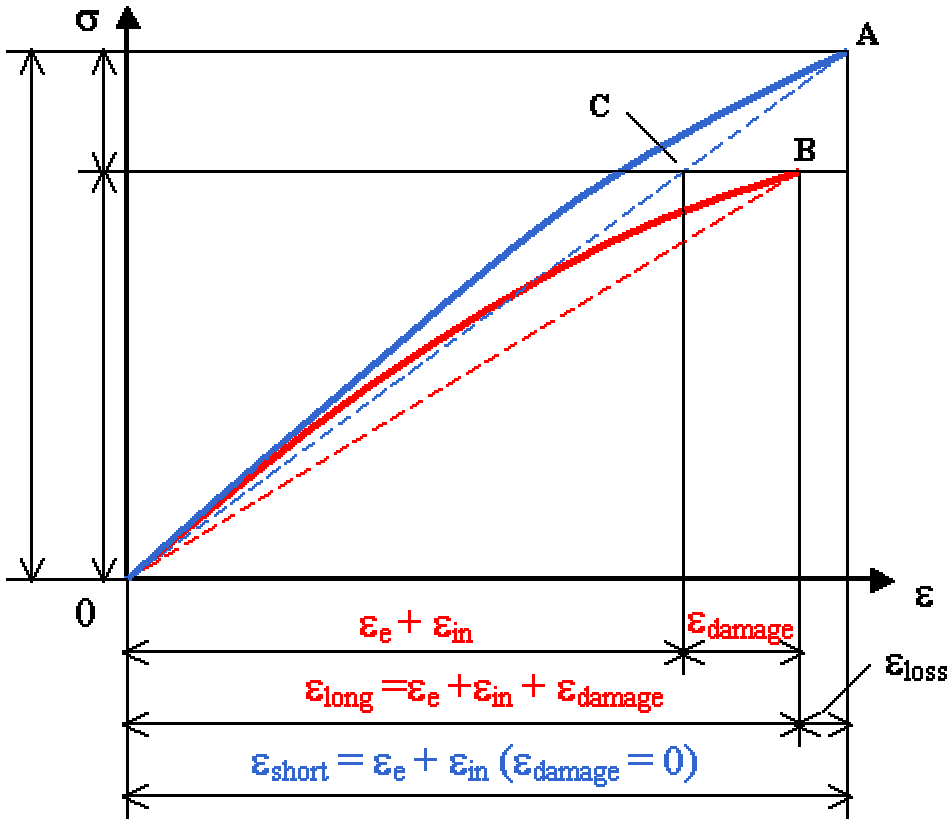

Figure 4.19 Diagram for strain rate dependent strain analysis. It helps calculate strain rate effected strain component ε_{damage}.

For both short-term and long-term tests, the peak axial strain can be decomposed as

$$\varepsilon_{short} = \varepsilon_e + \varepsilon_{in} \tag{4.8}$$

$$\varepsilon_{long} = \varepsilon_e + \varepsilon_{in} + \varepsilon_{damage} \tag{4.9}$$

where ε_e is an elastic strain component and ε_{in} an inelastic strain component. In this study, $\varepsilon_{long} < \varepsilon_{short}$. The strain rate effected strain component ε_{damage} for each strain rate

can be determined from σ_{loss}, ε_{loss} and E_S (E_S must be evaluated at point A as shown in Fig. 4.19). These three parameters can be determined using Eqs. 4.5-4.7. The highest strain rate serves as a baseline. The parameters σ_{peak}, ε_{peak} and E_S evaluated at the baseline are considered the limits as $t \rightarrow 0$.

$$\varepsilon_{damage} = \frac{\sigma_{loss}}{E_S} - \varepsilon_{loss} \tag{4.10}$$

Applying Eqs. 4.5-4.7 and Eq. 4.10, peak or total axial strain, strain component caused from elasticity and instantaneous inelasticity as well as strain rate effected strain component at each strain rate can be determined, as shown in Fig. 4.20.

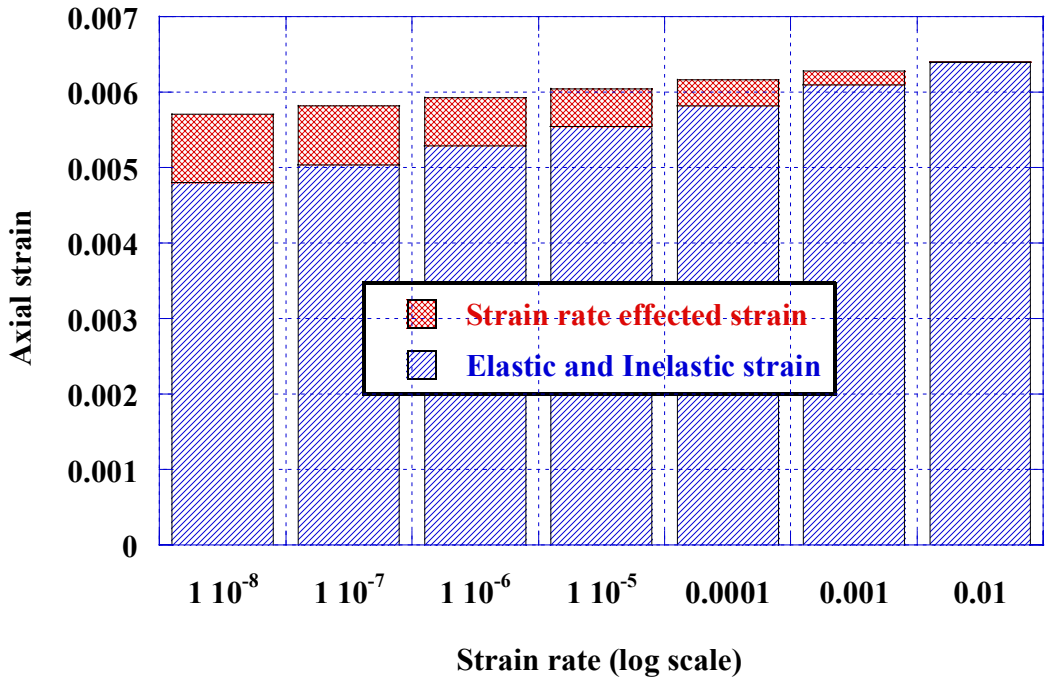

Figure 4.20 Schematic diagram showing changes of each strain component with strain rate.

Peak axial strain decreases with a decrease of strain rate at a rate defined by Eq. 4.6. Strain component due to strain rate dependent damage decreases with a faster rate than the peak strain does. This strain component affects the stiffness of a specimen. It is reflected by the secant modulus.

Fig. 4.21 gives a plot of changes of the ratio of strain component due to strain rate dependent damage to total axial strain. This plot is a slightly convex downward curve. When the strain rate decreases from 10^{-4} to $10^{-8} s^{-1}$, the damage strain increases from 5.6% to 15.8% of the total axial strain. This percentage is also a reflection of strain rate dependent stiffness loss of the tuff specimens.

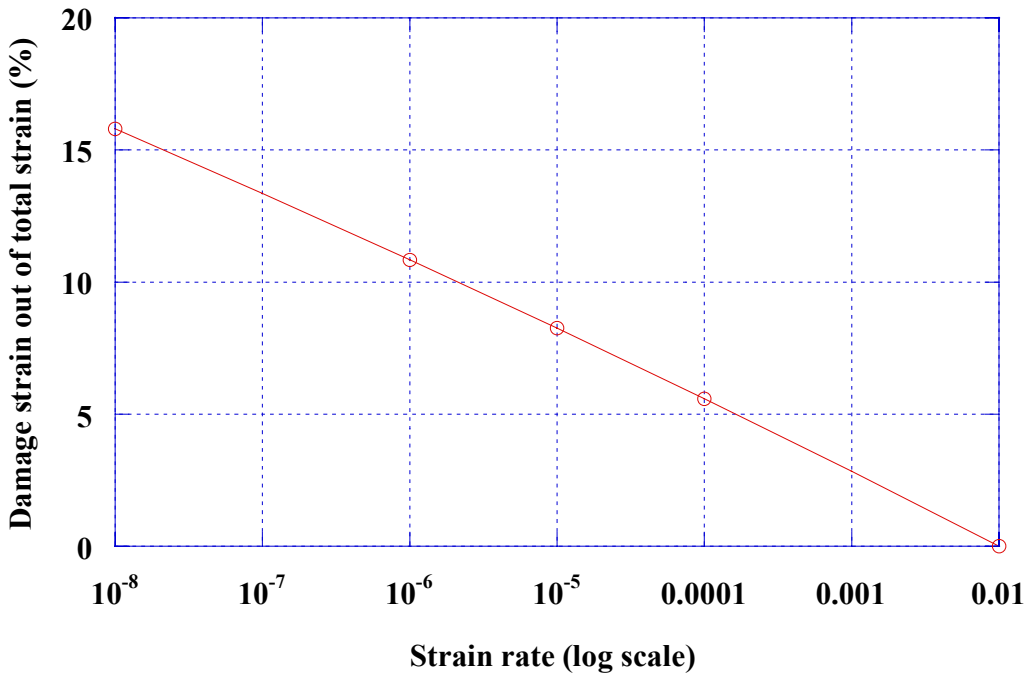

Figure 4.21 Percentage of strain rate dependent damage strain component to total axial strain versus strain rate.

The stiffness loss with a decrease of strain rate can be expressed as strain rate dependent or time dependent stiffness damage. Taking the concept of damage from damage mechanics (Lemaitre, 1992), let the stiffness damage factor be defined as

$$\omega = 1 - \frac{E_{S-long}}{Es} \tag{4.11}$$

where ω is the damage factor for strain rate dependent stiffness. E_{S-long} .is the secant modulus measured at peak strength for a long term test. E_S is secant modulus measured at peak strength for a short term test. Again, E_S is treated as the baseline. For short-term test, the specimen is considered to exhibit no strain rate effected damage, so $\omega = 0$. Referring to Fig. 4.19, the damage factor can be transformed to

$$\omega = 1 - \frac{E_{S-long}}{E_S} = 1 - \frac{\dfrac{\sigma_{long}}{\varepsilon_{long}}}{\dfrac{\sigma_{long}}{\varepsilon_{long} - \varepsilon_{damage}}} = 1 - \frac{\varepsilon_{long} - \varepsilon_{damage}}{\varepsilon_{long}} = \frac{\varepsilon_{damage}}{\varepsilon_{long}} \tag{4.12}$$

In fact, the curve in Fig. 4.21 is the relation between the damage factor ω and strain rate $\dot{\varepsilon}$. The importance of the strain rate dependent or time dependent strain analysis is as follows: 1) it helps understand how strain softening occurs under long-term loading. Due to the time dependent stiffness loss, a unit reduction of usable strain is related to (coupled with) a smaller stress application; 2) it influences the selection and design of support system. The principle of engineering design requires that the support system should match the surrounding rock in deformational property.

4.9 Long term strength under constant strain rate loading condition

In order to discuss long-term strength, a relation between peak strength and time is estimated. The estimation is conducted using the same data, the same software and the same procedure as for Eqs. 4.5-4.7. The strength as power function of time is the best estimation (Eq. 4.13). A summary of statistics for the regression is listed in Table 4.6.

$$\sigma_{peak} = 236.5t^{-0.0173} \tag{4.13}$$

Table 4.6 Statistics for regression of σ_{peak} on t

Variable	Estimate	Standard Error	t-value	Pr > |t|
Coefficient	236.5469	15.6130	15.15	<.0001
Exponent	-0.01732	0.00860	-2.01	0.0482

Eq. 4.13 represents that a specimen with the peak strength σ_{peak} takes time t to failure when it is loaded at a constant strain rate. The laboratory tests last for about a week at the longest. To predict a long term strength based on the results of these tests requires extrapolation. How accurate the prediction will be depends on many factors. The most important factor is whether the trend of response variable is understood or not. To validate the subsequent prediction, more tests with longer duration are needed.

Applying Eq. 4.13, a group of values for maximum stress versus time duration is listed in Table 4.7 and plotted in Fig. 4.22. The table and the plot can be interpreted as: if a

specimen breaks under 214.32 MPa in 5 minutes, it will break in 300 years if the stress ultimately reaches 158.98 MPa.

Table 4.7 Maximum stress to break a specimen in a specified time duration

Time	5 minutes	1 year	10 years	50 years	100 years	200 years	300 years
Maximum stress (MPa)	214.32	175.47	168.61	163.98	162.03	160.10	158.98

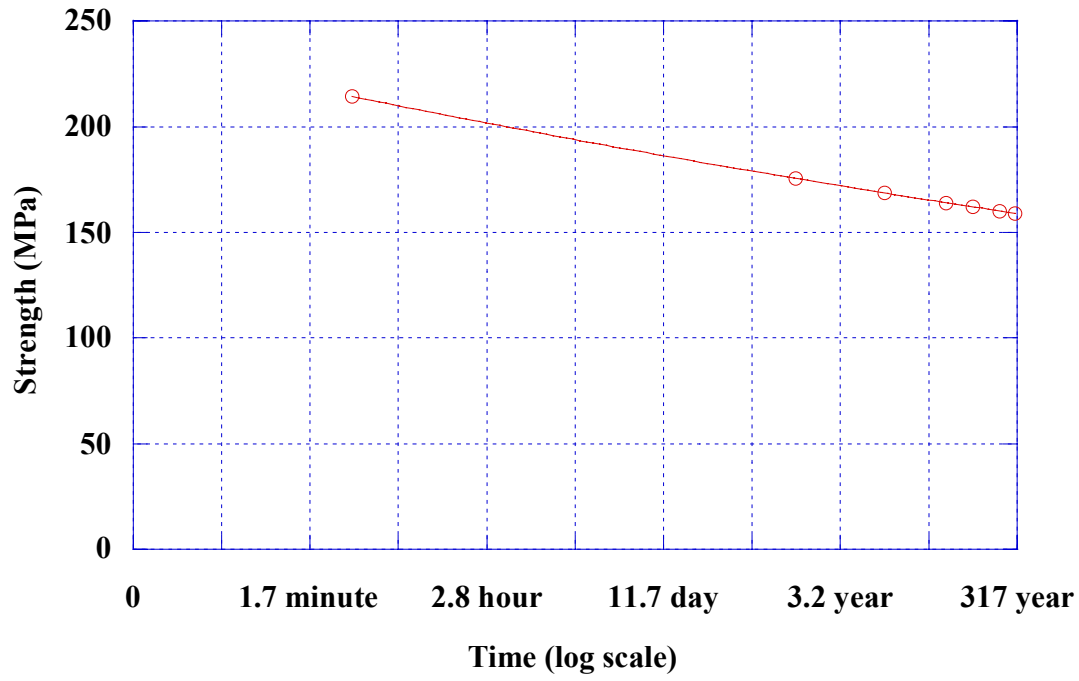

Figure 4.22 Maximum stress to break a specimen in a specified time duration

The property of the power function gives a conservative prediction for long-term strength. As time goes on, the curve tends to flatten. The predicted results show that from 1 year to 10 years, the peak strength drops 6.86 (175.47 – 168.61) MPa, whereas from 100 years to 300 years, the peak strength drops only 3.05 (162.03 – 158.98) MPa.

CHAPTER 5 ANALYSIS OF CREEP TESTS

5.1 Separation of creep curves

As mentioned in Chapter 3, it is difficult to select a single load level to lead a tuff specimen to failure within a reasonable test duration. Alternatively, stepwise load was applied for all the fourteen creep tests. In each test, one or more unloading/reloading may be applied. Does the unloading/reloading affect the strain rate at the subsequent loading level? No, at least not significant. On unloading, the damage does not change, resulting in a memory of the previous maximum stress state. This effect is observed experimentally by recording acoustic emissions as the rock is loaded. The rock remembers the previous maximum stress state through the mechanism of changing crack states (Costin and Holcomb, 1983).

In strain-time curves as shown in Fig. 5.1, transient creep and steady-state creep exist at every stress level before the final one. In the final stress level, typically all three creep stages exist. For the special case where the specimen is close to failure, the steady-state creep may not develop. To study the strain development as a function of time, the strain-time curve for each stress level will be separated for each stress level. Fig. 5.2 gives a strain-time curve for one stress level.

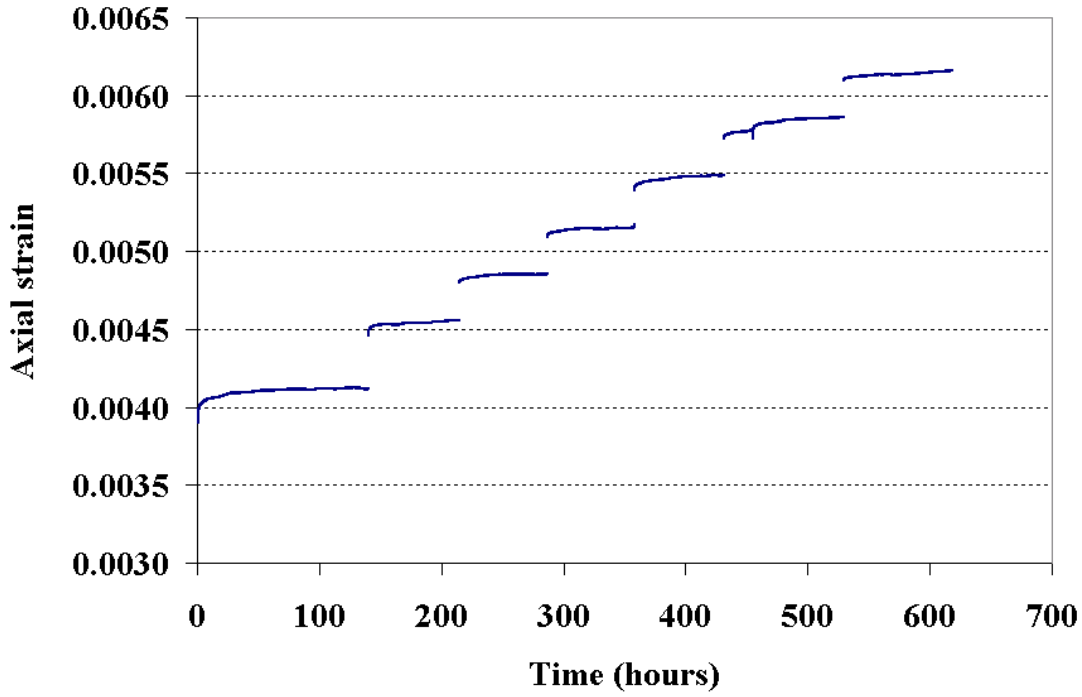

Figure 5.1 A stepwise experimental creep curve under multiple constant stresses (Specimen ID: 01023364-1-CU, from Tptpmn)

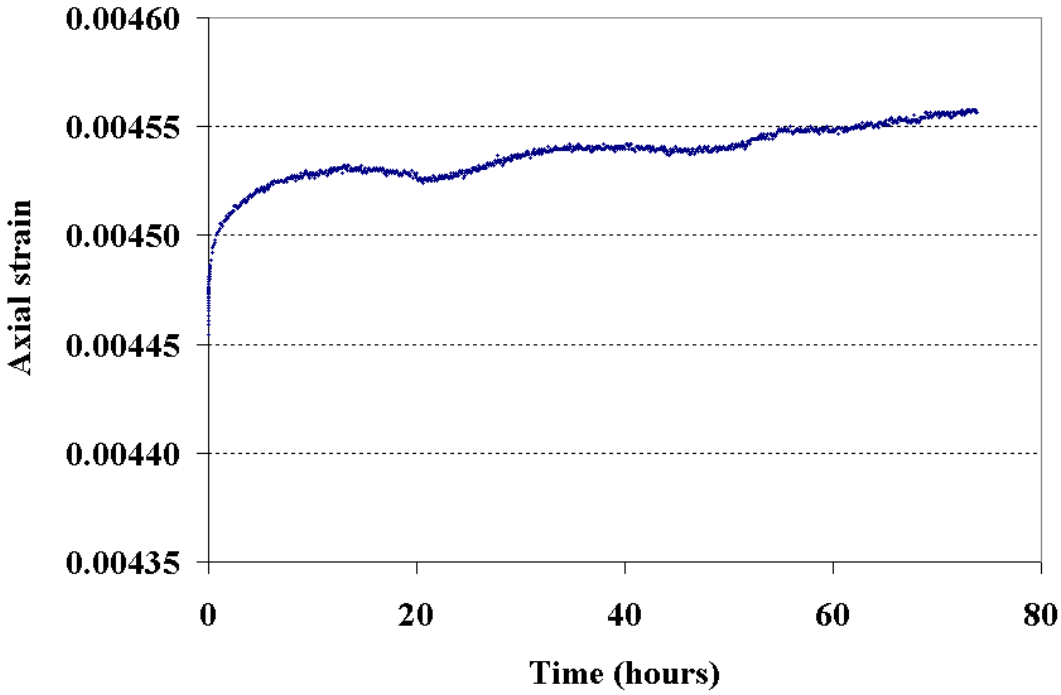

Figure 5.2 Experimental strain-time curve for one stress level (Specimen ID: 01023364-1-CU, Stress level = 146.90 MPa, from Tptpmn)

Transient creep and steady-state creep typically exist in a strain-time curve for each stress level. A strain-time curve for a single stress level will be further separated at the transition point to study the distinct behavior for each different creep stage.

5.2 Transient creep

The transient creep stage normally takes 7 to 25 hours to complete. Fig. 5.3 shows an experimental strain-time plot and a fitting curve. For almost every stress level the strain-time transient creep stage observed in this study can be fit with an equation of the form

$$\varepsilon_{tr} = \varepsilon_0 + \alpha t^{\beta} \tag{5.1}$$

where ε_0 is the initial axial strain, α and β are constants. In the equation of the fitting curve in Fig. 5.3, α and β take the values of 4.67×10^{-5} and 0.22, respectively.

Taking the derivative of Eq. 5.1 with respect to time *t*, the strain rate for the transient creep is obtained as

$$\dot{\varepsilon}_{tr} = \alpha \times \beta \times t^{\beta-1} \tag{5.2}$$

Eq. 5.2 has the same form as the empirical law for salt proposed by Andrade (1910) which was quoted by Dusseault (1993, p. 121) for transient creep. In Andrade's study, the exponent of *t* takes the value of –2/3. When Cruden (1974, p. 68) used Griggs' data for alabaster creep tests (1940) to fit the strain-time curve for transient creep, he finds the same function as Eq. 5.2.

Applying Eq. 5.2, the strain rate during transient creep was calculated. The strain rate as a function of time is plotted in Fig. 5.4. The curve of secant modulus (determined by dividing axial stress by axial strain) versus time is plotted in the same coordinate system. At the beginning of transient creep, both strain rate and secant modulus decelerate rapidly. As time goes by, the two parameters decrease, following similar functions. This view tells us that a relationship might exist between the two parameters in transient creep.

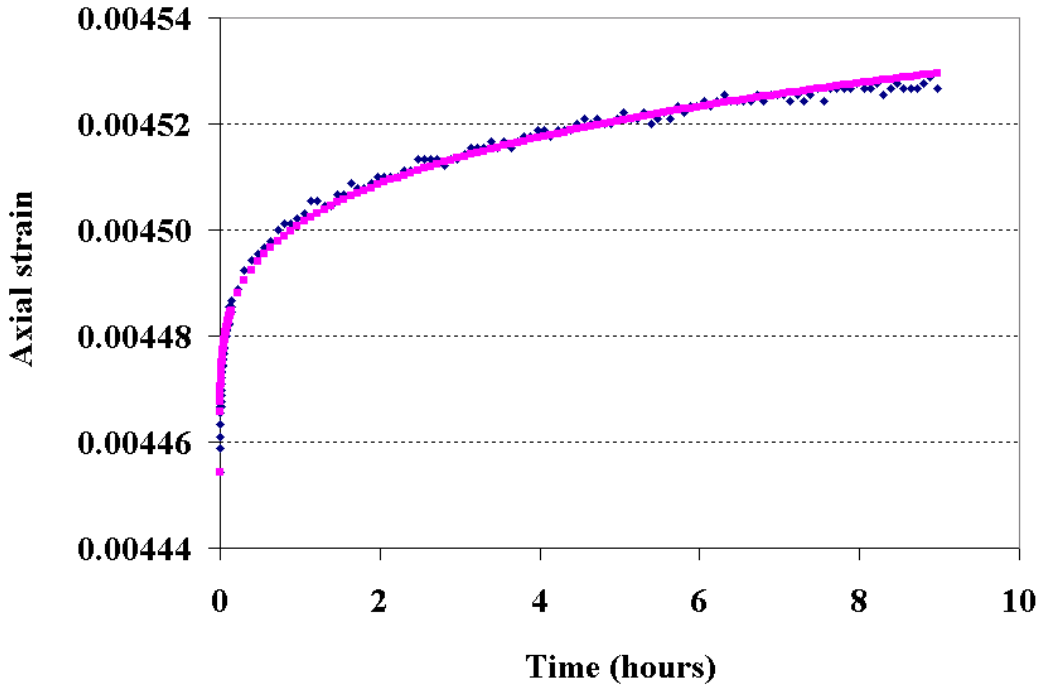

Figure 5.3 Experimental strain-time curve for transient creep and fitting curve (Specimen ID: 01023364-1-CU, Stress level = 146.90 MPa, from Tptpmn)

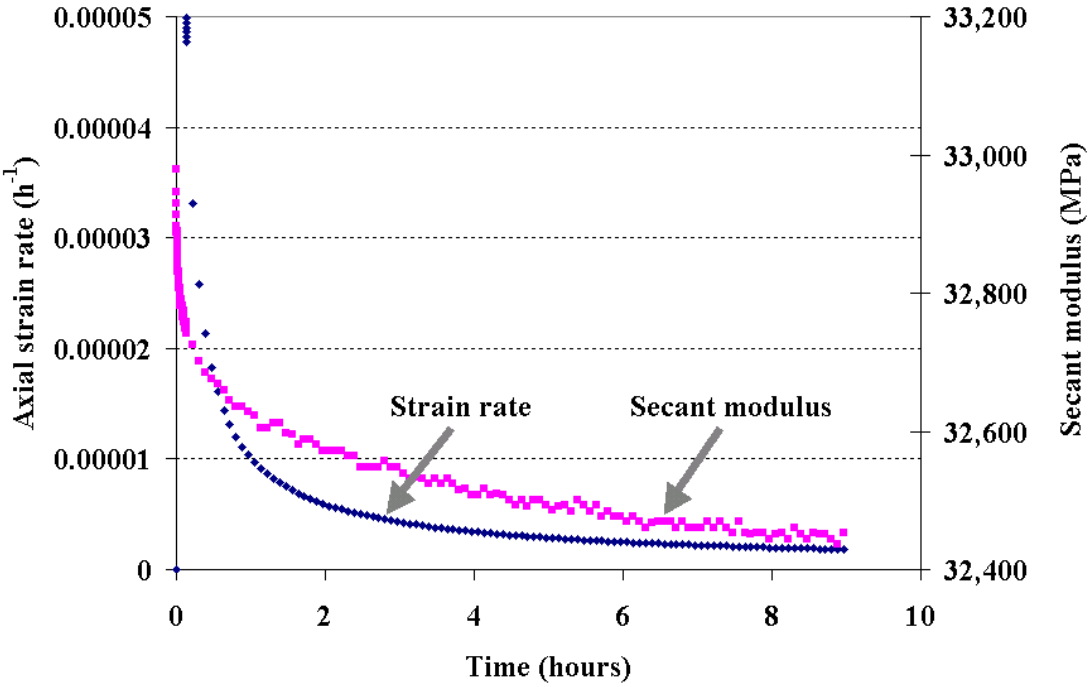

Figure 5.4 Strain rate-time and secant modulus-time curves for transient creep (Specimen ID: 01023364-1-CU, Stress level = 146.90 MPa, from Tptpmn)

The elastic aftereffect of the specimen may be a reasonable explanation to the above phenomenon. The elastic aftereffect is due to the thermoelastic property of the material. A detailed discussion of this can be found in Timoshenko (1953, pp. 336-357). If the explanation is correct, then the transient creep is not a real creep. It is widely believed that cracking is the mechanism responsible for creep of brittle rock (Costin, 1985, p. 26; Scholz, 1968b, p. 3300). However, it is still quite uncertain whether the three stages result from the same mechanism. In a study of time-dependence of quartz, Martin (1972, p. 1416) finds that time-dependent cracking has an initial period of rapidly decelerating

growth followed by what might be interpreted as a steady-state segment if the test is short.

Picking the axial stress and axial strain at the transition point between transient and steady-state creep for each stress level, plotting these points in a stress-strain coordinate, and connecting these points, forms the boundary between transient and steady-state creep for each stress level (Fig. 5.5).

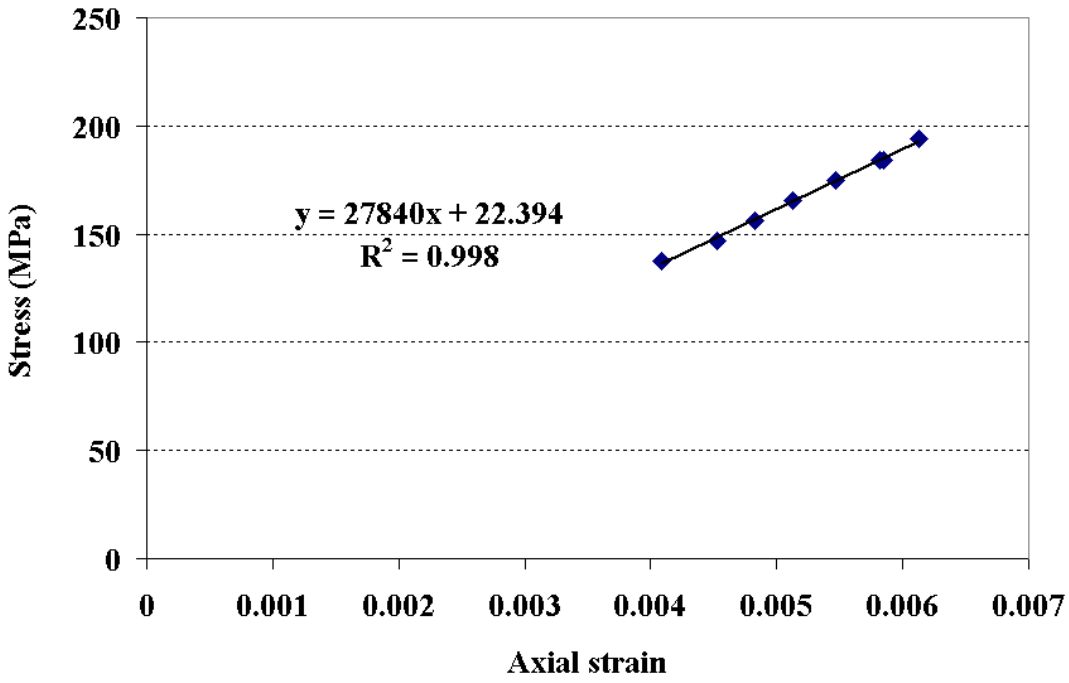

Figure 5.5 Stress-strain magnitudes at which the transition takes place from transient to steady-state creep at seven stress levels (Specimen ID: 01023364-1-CU, from Tptpmn)

Below the elastic limit, the plot, as shown in Fig. 5.5, appears approximately linear. This plot indicates that a stabilized secant modulus marks the end of the transient creep and the beginning of the steady-state creep. Within the elastic limit, the secant modulus

slightly decreases with an increase of the stress level. The decrease of the secant modulus results from stiffness damage (a finding in Chapter 4).

Fig. 5.6 gives an example in which a nonlinear part occurs at the end of the stress-strain plot. As shown in Fig. 5.6, the three points at the end of the plot deviate from the straight trend. This occurs when the specimen is severely damaged. Before a specimen fails, a larger strain is generated. The elastic limit is exceeded. The rock is no longer elastic. Fig. 5.7 illustrates the transition boundary (dashed line AB) between transient and steady-state creep, which describes how Figs. 5.5 and 5.6 were obtained.

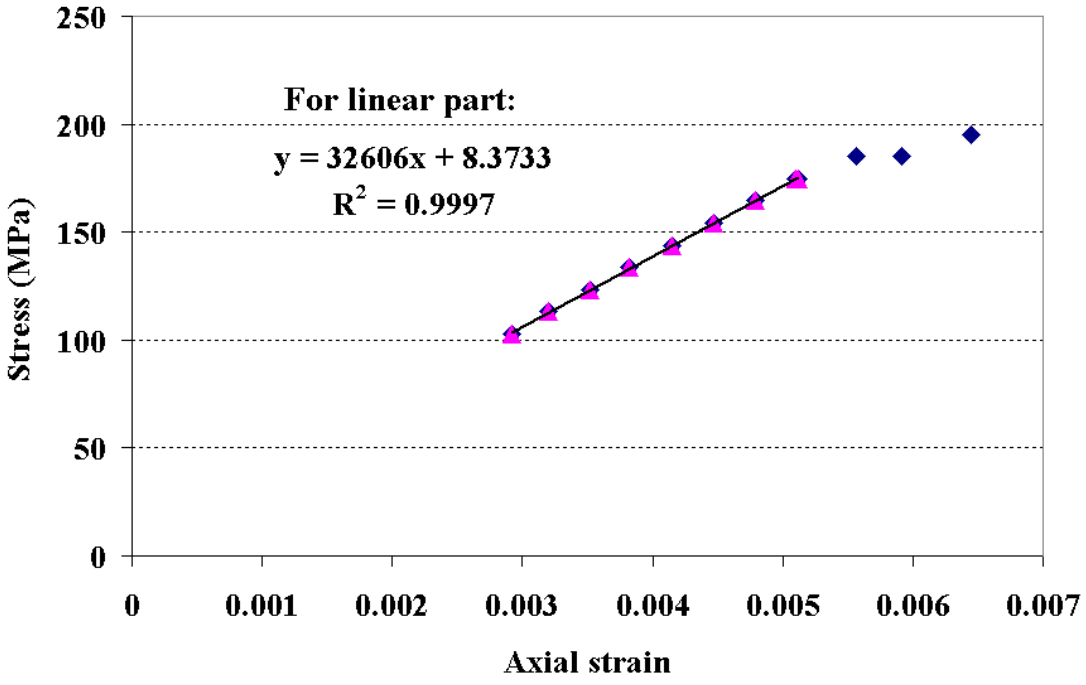

Figure 5.6 Stress-strain position at which the transition takes place from transient to steady-state creep at twelve stress levels (Specimen ID: 01023665-2-CU, from Tptpmn). At the highest stress levels accelerating creep has been reached.

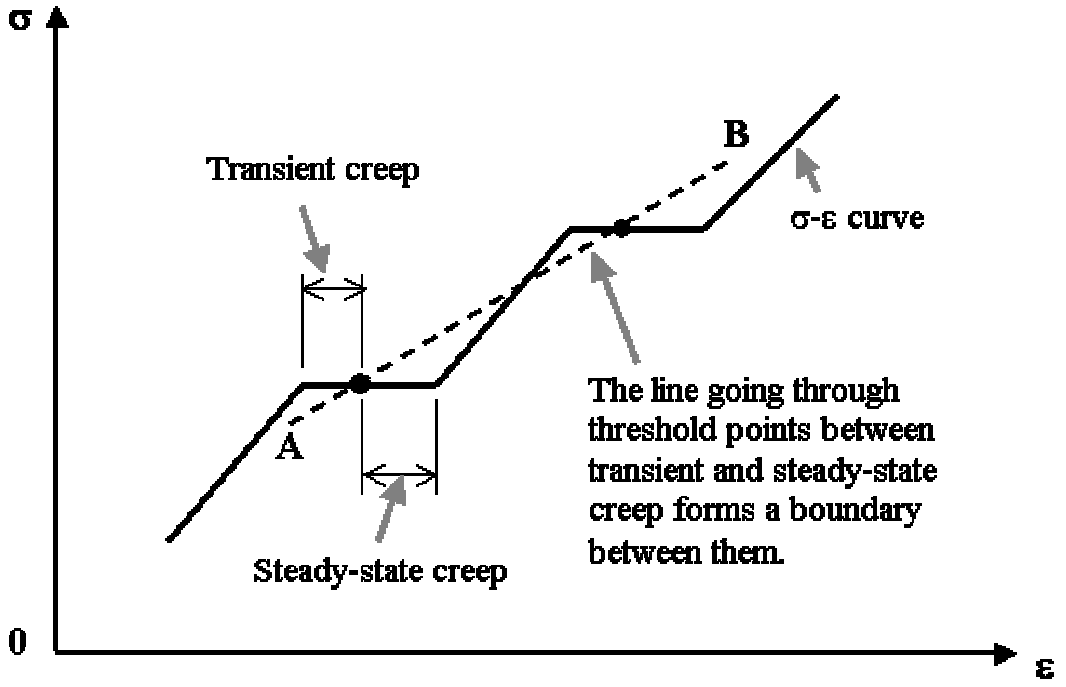

Figure 5.7 Diagram showing the stress-strain curve for creep under stepwise loading and the boundary (AB) between transient and steady-state creep

5.3 Steady-state creep

The steady-state creep in all the tests was maintained from 2 to 7 days. Over this time most of the strain-time curves appear clearly linear. For some stress levels strain-time curves were seriously affected by ambient temperature. Those strain-time curves have not been used to calculate strain rates. Only the strain-time curves obtained within a reasonably narrow temperature range are used. An ideal temperature range for strain rate measurements is within $\pm 1°$C. Some times if the temperature changes beyond this range, the strain-time curves may still be used. In those cases a remedy measure can be adopted. If a strain-time curve has been maintained for at least three days and both the ends of the curve were obtained under the condition of the same or very close temperature, this

strain-time curve may still be considered reliable since it can be fitted with a straight line. As a general rule, only those strain-time curves are used from stress levels at which the steady-state creep part has been maintained for at least three days. The slope of the straight line fit to a strain-time curve is the strain rate. Fig. 5.8 shows an example of how a strain rate for a steady-state creep at a given stress level was obtained.

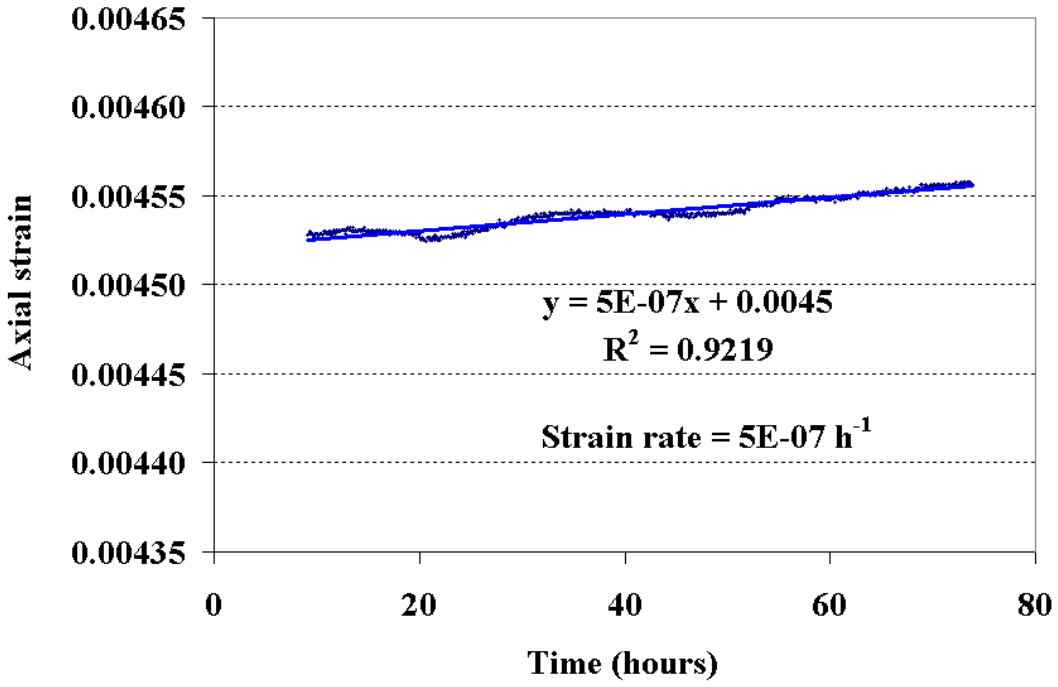

Figure 5.8 Experimental strain-time curve for steady-state creep and best fit straight line (Specimen ID: 01023364-1-CU, Axial stress = 146.90 MPa)

In addition to temperature consideration, the strain rate cannot be used if a test specimen was previously loaded higher than the current stress level. In this situation the specimen could have suffered some degree of damage. The measured strain rate would have a higher strain rate than it should be.

To understand the stress dependence of a strain rate, a scatter plot of strain rate versus stress level is shown in Fig. 5.9. A clear trend is observed in the plot in which strain rate increases nonlinearly with an increase of stress. In this test, the starting stress is about 70% of the peak strength. If a starting stress is sufficiently low, the pattern of the strain rate-stress plot tends to be different (Figs. 5.10 and 5.11). Figs. 5.10 and 5.11 indicate that the points representing strain rate versus stress level show more scatter at low stress (left side of dashed lines). When the axial stress reaches a certain level, the distribution of the points follows the same trend as in Fig. 5.9. This trend can be described as a type of power function. The dashed lines are visually drawn boundaries. A critical stress level must be applied to define this boundary. Martin (1972) points out that above approximately half to two-thirds of the compressive strength, the dominant mode of deformation becomes the opening and subsequent growth of axial cracks. Martin (1972) also references several authors (including Peng, 1970, Wawersik, 1968, Wawersik and Brace, 1971) who have shown that in granite microfracturing starts when the rock is stressed to about 60 % of its strength. This critical stress can be related to the critical stress intensity factor or fracture toughness, K_{IC} which is a material constant. K_{IC} is the maximum value of the stress intensity factor K_I for mode I (opening mode) crack.

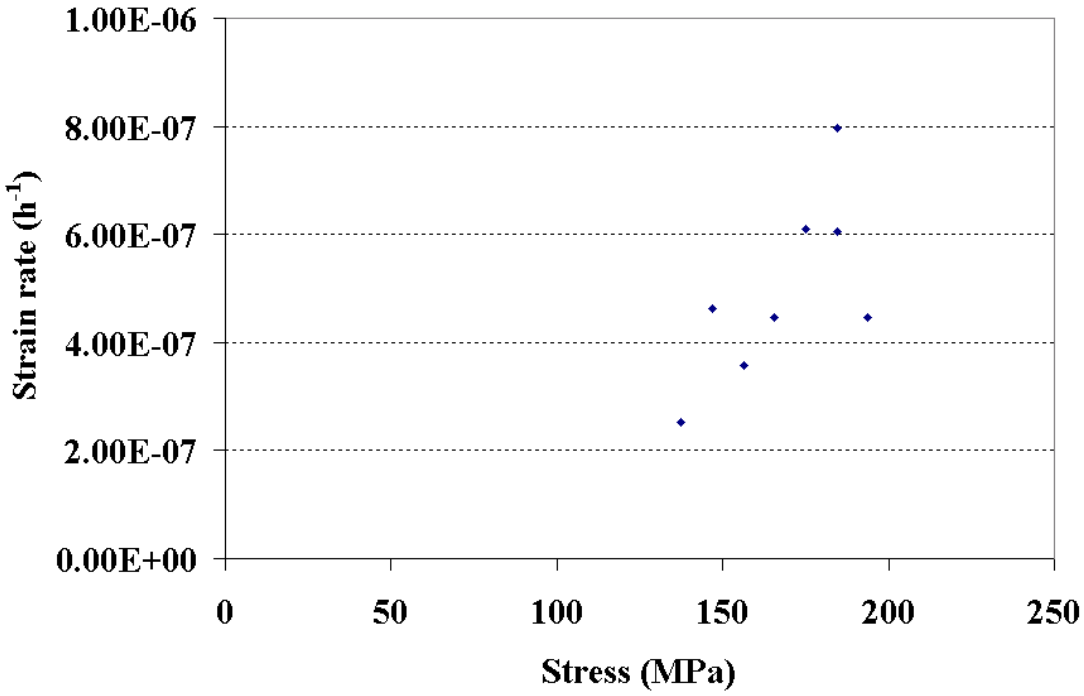

Figure 5.9 Strain rate as a function of stress showing stress dependence of steady-state creep strain rate (Specimen ID: 01023364-1-CU)

Fig. 5.10 shows an example of a curve fit with the power function. Eq. 5.3 is rewritten from the equation in Fig. 5.10, with real variables where $\dot{\varepsilon}_S$ denotes the strain rate during steady-state creep. This equation agrees closely with the finding obtained by a number of investigators, which is quoted by Scholz (1968b, p. 3299): creep rate can often be given as a power function of stress, with the exponent greater than unity for moderate stresses and near unity for very small stresses. In a study of static fatigue of rock salt under uniaxial compression, Cruden (1974, p. 70) proposed the same form as Eq. 5.3 for the strain rate-stress relationship, where the exponent of σ is 2.7. To obtain a more accurate function, more tests are needed.

$$\dot{\varepsilon}_S = 8 \times 10^{-18} \times \sigma^{4.98} \tag{5.3}$$

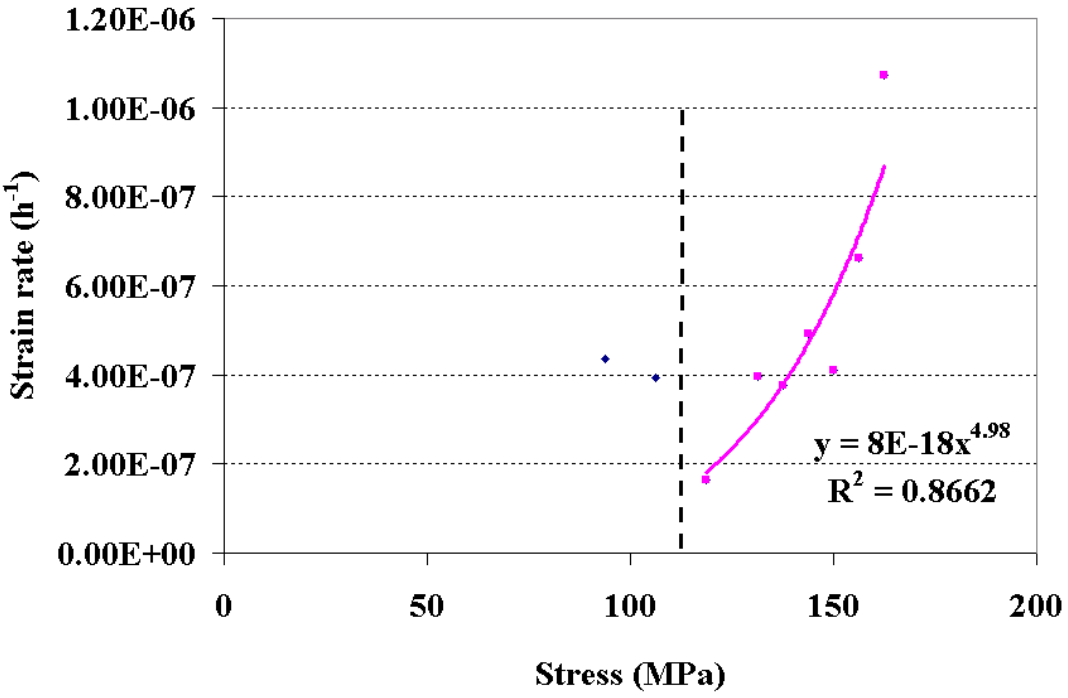

Figure 5.10 Steady-state creep strain rate as a function of stress (Specimen ID: 01023363-1-CU, from Tptpmn)

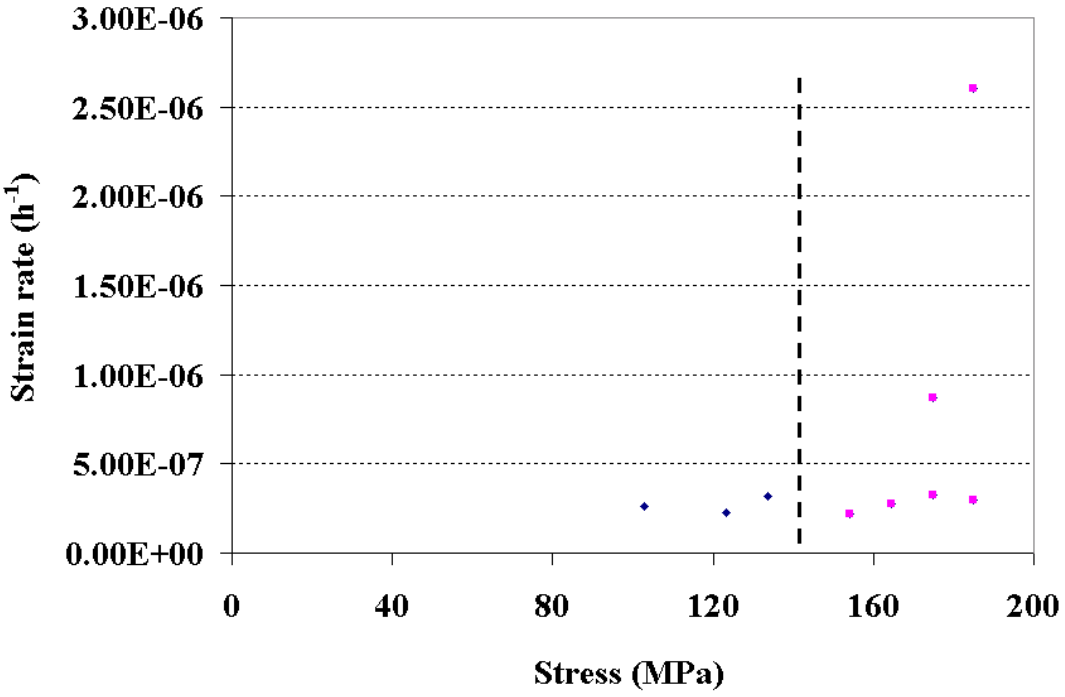

Figure 5.11 Steady-state strain rate as a function of stress (Specimen ID: 01023665-2-CU, from Tptpmn)

Carrying on the damage concept applied in Chapter 4, stiffness damage is calculated for some tested specimens. Secant modulus is determined for each stress level. Here the stiffness damage factor is determined by

$$\omega_E = 1 - \frac{E_{SD}}{E_{SI}} \tag{5.4}$$

where ω_E = stiffness damage variable, E_{SD} = secant moduli for a damaged specimen. For each stress level, it is determined at the end of the steady-state creep. E_{SI} = secant

modulus for an undamaged specimen. It is determined at the beginning of steady-state creep at the first stress level.

Figs. 5.12 and 5.13 give stiffness damage versus axial stress for two specimens. The plot in Fig. 5.12 shows that at low stress, say lower than 135 MPa, the stiffness damage in the specimen is very small. Beyond this stress, the damage increases rapidly. In Fig. 5.13, the creep started at relatively high stress level. The stiffness damage that occurred in each loading step is much higher. In fact the stiffness damage analysis provides the same indication as the plots in Figs. 5.9-5.11. Both approaches indicate a stress threshold exists at about 50% of the strength of a specimen. Below the threshold, the specimen creeps at a very low rate, if at all. The strain rates measured in this low range seem not regular at all. The stiffness damage stays at a very low level, if there is any.

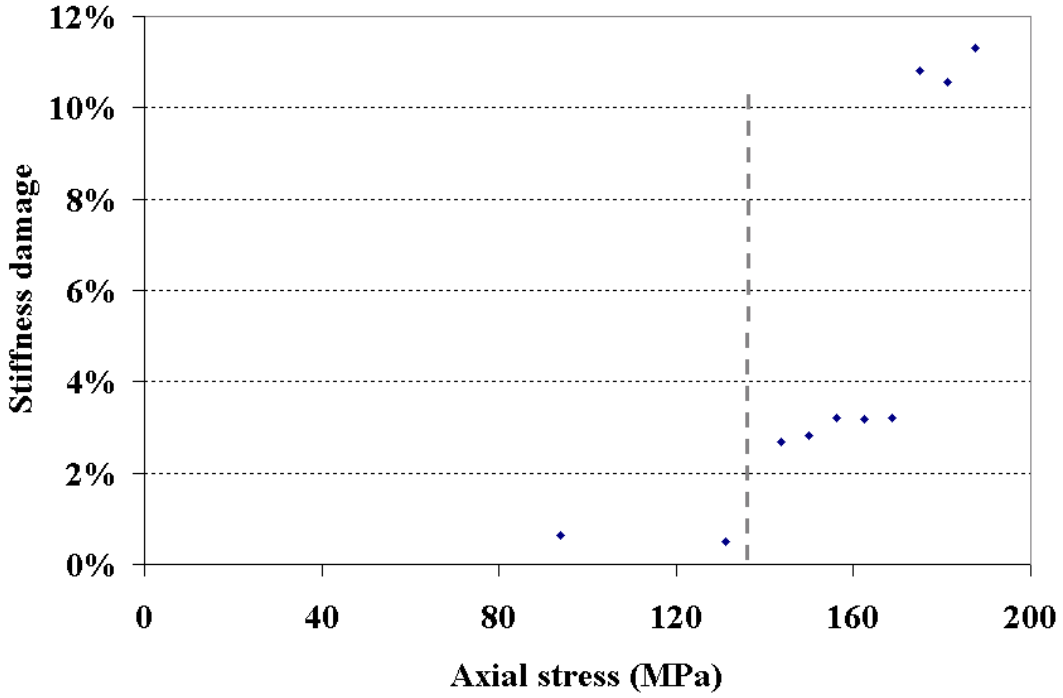

Figure 5.12 Stiffness damage as a function of stress. Below a certain stress, the stiffness damage in the specimen is very small, if there is any at all (Specimen ID: 01023363-3-CU; from Tptpmn; starting stress level = 87.5 MPa).

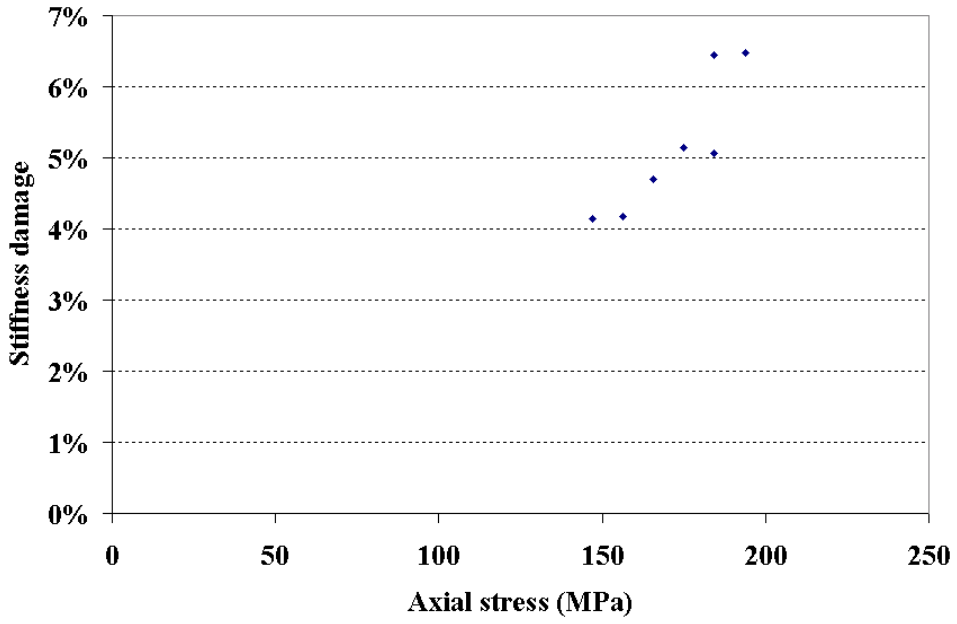

Figure 5.13 Stiffness damage as a function of stress (Specimen ID: 01023364-1-CU, from Tptpmn; starting stress level = 137.5 MPa).

5.4 Accelerating creep and specimen damage

For each test, this final creep stage occurs during the last stress level. If a specimen fails right after a load increase, this stage may not occur. Since each load increment is only about 7-10 MPa, and the loading is incremented very quickly, there is no case in which a specimen fails during a loading increment. Accelerating creep usually lasts for no longer than two hours. Figs. 5.14 and 5.15 give two examples of accelerating creep. In Fig. 5.14, when stress increases from 84.4 MPa to 89.6 MPa, the specimen keeps creeping until about 2.8 hours. Within this time period, the creep rate goes fairly high, but remains stable. A jump in the strain-time curve indicates that a fracture occurs inside the

specimen. This fracture is known as unstable because it occurs under a constant stress. Beyond this point, the creep goes to the accelerating stage.

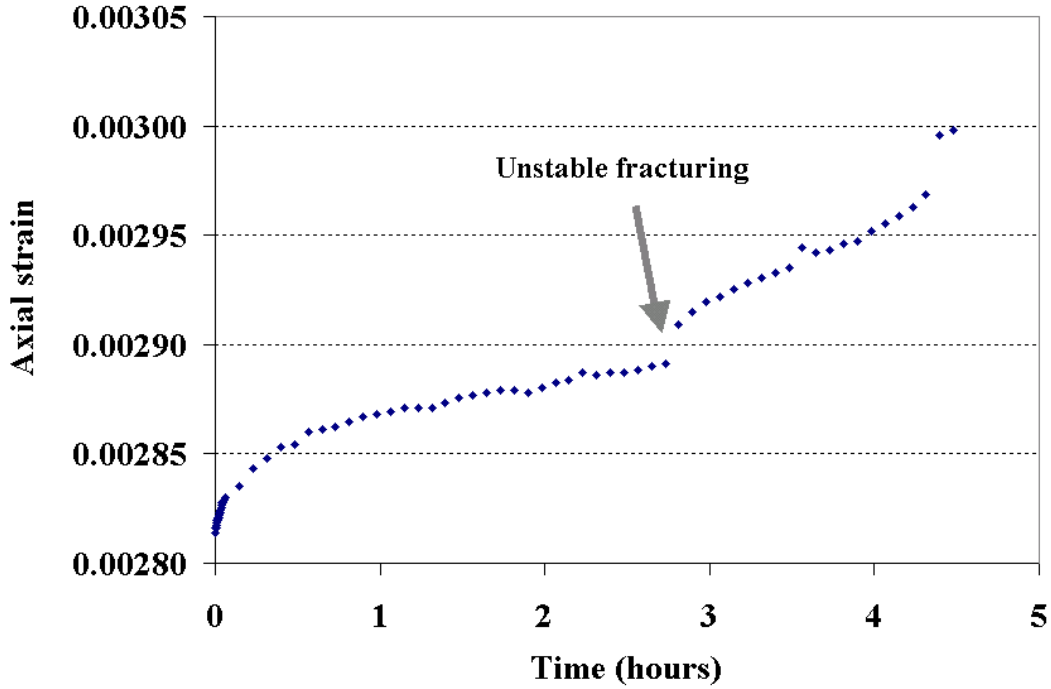

Figure 5.14 A fracture indicates the beginning of the accelerating creep (Specimen ID: 01014951-1-CU, from Tptpmn). Axial stress = 89.6 MPa.

Fig. 5.15 shows a case in which the accelerating creep starts from the very beginning of the current stress level. This may reveal that unstable fracturing initiated during the loading increase. Until the end of the previous stress level (93.2 MPa) the creep was stable. The whole process lasts about 1.7 hours.

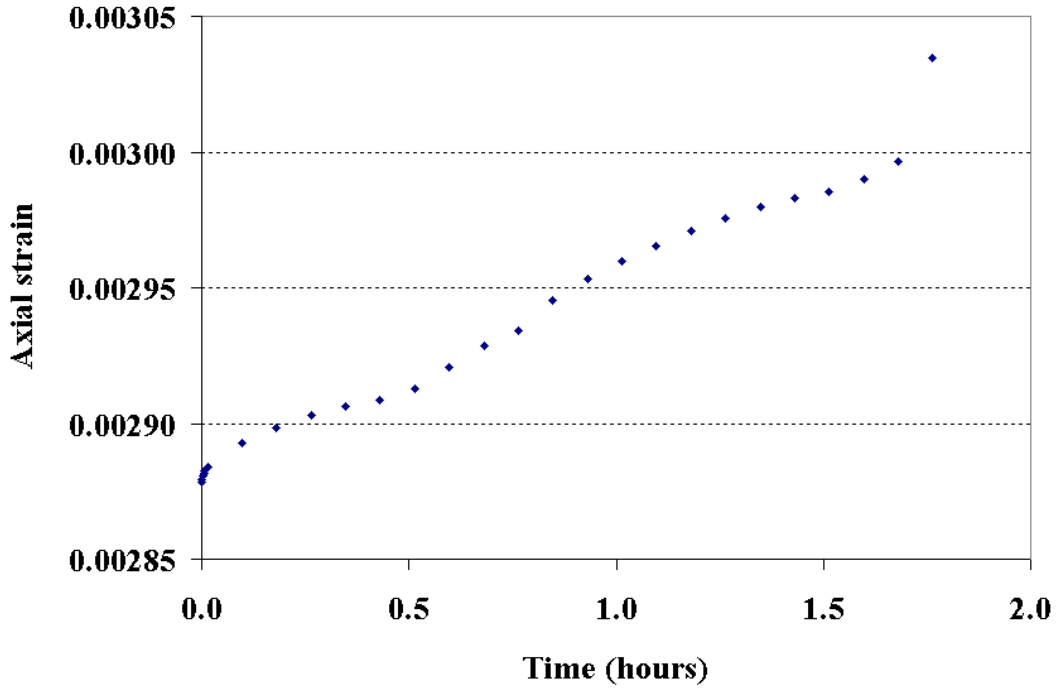

Figure 5.15 The highest stress level showing that accelerating creep develops over the course of an entire constant stress level (Specimen ID: 01014733-2-CU, stress level = 103.5 MPa, from Tptpll).

Unstable fracturing may not necessarily lead a specimen to the accelerating stage. Fig. 5.16 gives an example in which an unstable fracture occurs at about a half hour after the new stress level has been reached. Both axial strain-time and lateral stain-time curves have a jump. This shows that an axial compression and a dilatancy take place simultaneously. After this fracture, the specimen takes about 30 hours to go to the accelerating stage which is very short.

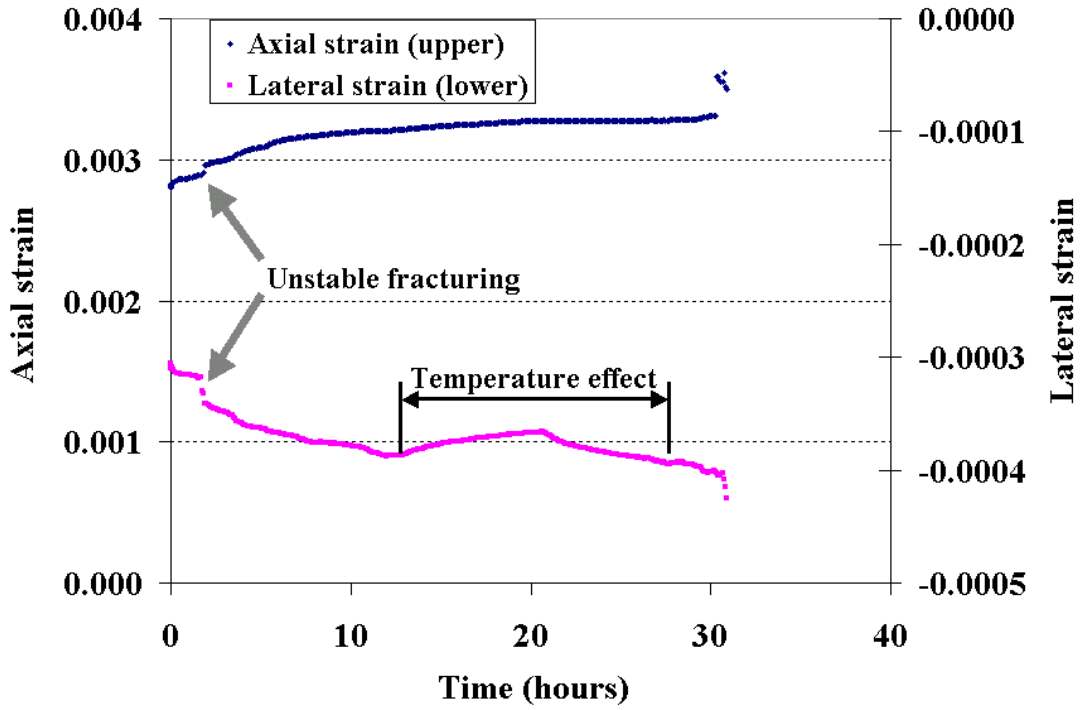

Figure 5.16 Axial strain-time and lateral strain-time at last stress level. Axial strain and lateral strain increase simultaneously (Specimen ID: 01014951-2-CU, from Tptpmn). Stress = 61.98 MPa.

Fig. 5.17 shows another example in which unstable fracture did not lead the specimen to failure. A jump in the strain-time curves occurs at the next to last loading step in a series of constant axial stress steps. Figs. 5.16 and 5.17 suggest that significant permanent deformation can start long before the accelerating creep obviously begins. The critical points where deviations occur from the straight trend indicate that larger strains are generated.

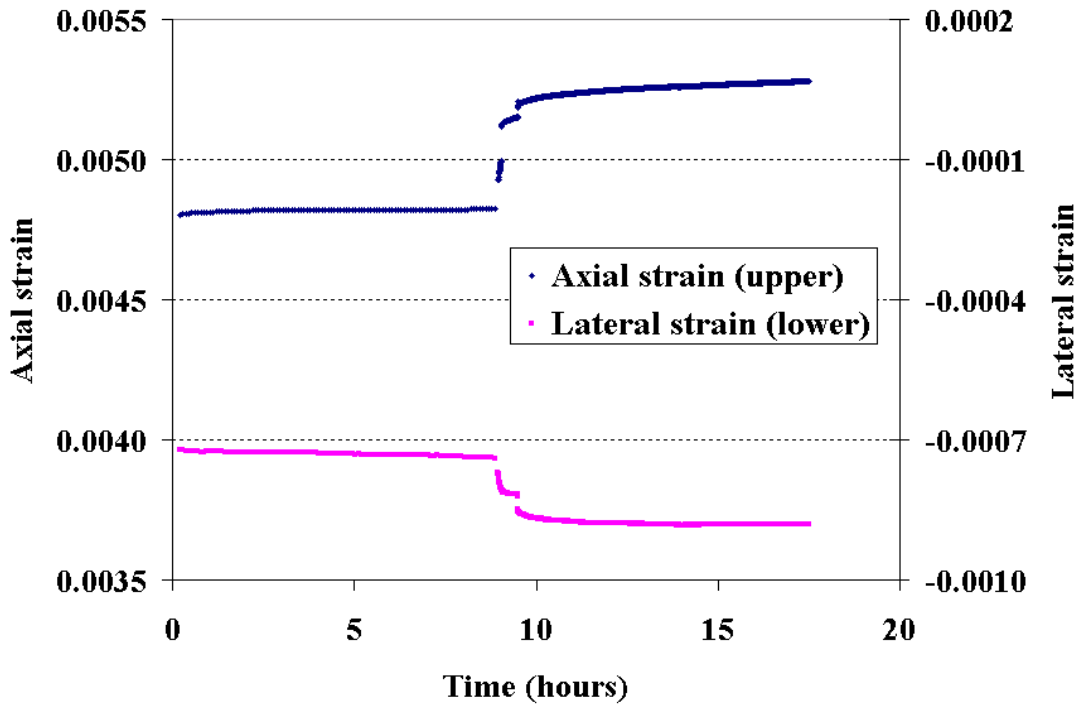

Figure 5.17 Internal damage of a specimen reflected in the strain-time curves at the next to last loading step in a series of constant axial stress steps (Specimen ID: 01023363-3-CU, from Tptpmn). Stress = 175.0 MPa.

At accelerating creep, the elastic limit of the rock has been exceeded. Scholz (1968a), Cruden (1974), and Kranz and Scholz (1977, p. 4893) believe that accelerating creep starts when a critical crack density is reached. At this stage the specimen has been damaged to such an extent that it can no longer resist the applied load elastically. Once a rock has entered this stage it inevitably fails unless it is unloaded (Kranz and Scholz, 1977, p. 4893). Cruden (1974, p. 69) referenced the works by Potts (1964) and Hedley (1965). In their studies the strain before the onset of accelerating creep is considered as safe strain.

Between steady-state and accelerating creep, there must exist a critical transition point. This point is analogous to the yield point for ductile materials. Beyond this point, the specimen loses its elasticity and enters a process where brittle failure develops. For this reason, determining the critical point where the accelerating creep starts is more important than to study the detailed process of the accelerating creep stage. However, without a good understanding of the creep process in this stage, determining the critical point could be very difficult.

5.5 Stress threshold discussion for creep

In Section 5.3, the plots of strain rate versus stress in Figs. 5.9-5.11 show that the tuff specimens creep at a very low rate below a certain stress level, say 110-140 MPa. The plots of stiffness damage versus stress in Figs. 5.12 and 5.13 give the same information. In the stress-strain curve analyses in Chapter 4, it is found that a relative change between axial strain and lateral strain occurs at about 52% of the average peak strength of the tuff from the middle nonlithophysal zone. It indicates that the tuff starts to significantly activate at about a half of the peak strength. Up to now, there have been three experimental evidences to support a conclusion: the Yucca mountain tuff in this study does not deform measurably below about 50% of its strength. As indicated in Figs. 5.9-5.11, beyond this stress the specimens creep stably approximately following a power function. Beyond steady-stage creep, unstable fractures start developing. It makes a specimen accelerating creep. As widely recognized a threshold stress must exist and indicate the beginning of the accelerating creep. This threshold stress is almost

impossible to determine by creep tests. With the aid of uniaxial compression tests, it becomes possible. Fig. 4.12 illustrates a stress-crack volumetric strain curve where a reversal point occurred at about 92% of peak strength. Fig. 4.14 and Table 4.2 show about 94% of the peak strength defines the start of unstable crack propagation. A schematic diagram in Fig. 5.18 summarizes these conclusive remarks.

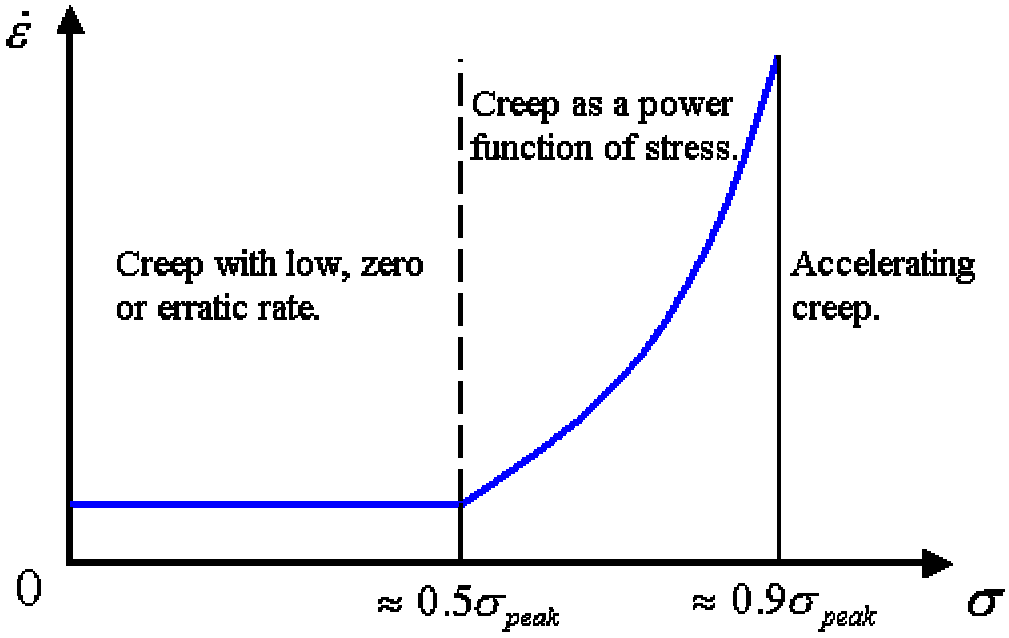

Figure 5.18 Schematic diagram illustrating creep rate development with stress. Below about 50% strength, a specimen creeps at an erratic, low or even zero rate. Above this stress, the specimen creeps with a power function of stress. Above about 90% of strength, unstable deformation occurs.

Below the first threshold, damage is short-term and insignificant. Above it, failure is only a matter of time (Lajtai and Dzik, 1996). For long term consideration, a safe stress is below 50% of peak strength. Beyond this, the structure must suffer creep. The creep rate depends on the stress level. The second threshold defines the limit for short term stress.

Above this stress, accelerating creep occurs, which leads to failure quickly unless the load is removed.

CHAPTER 6 BRAZILIAN (INDIRECT SPLITTING TENSILE) TESTING, INCLUDING STRAIN-RATE DEPENDENT STRENGTH MEASUREMENTS

6.1 Experimental description

Brazilian (Indirect splitting tensile) tests have been performed on 158 specimens. Three specimens were collected from the lower lithophysal zone of the Topopah Spring Tuff formation (Tptpll). All others were collected from the middle nonlithophysal zone (Tptpmn). The specimen source information and test results are given in Tables 6.1 and 6.2, respectively (at the end of this chapter). The test specimens are prepared from rock cores. Of the specimens, 146 have a nominal diameter of 2.4 inch (60.96 mm), 12 of 1.78 inch (45.21 mm). All the specimens are sawed and ground. The ratio of thickness to diameter is between 0.2 – 0.75, to meet ASTM D3967-95a. Moisture contents of 96 specimens have been measured before testing. The mean is 0.87% and standard deviation is 0.19%. Thirty four specimens have flaws. These flaws include lithophysal cavities and obvious vapor-phase altered inclusions.

All the tests are performed in an MTS testing machine. Load is measured using a load cell. Displacement is measured using the machine LVDT. The strain of a specimen is calculated by dividing the displacement (assumed equal to the diametrical compression) by the diameter of the specimen. So the measured displacement is not only for the specimen, but also includes the deformation of steel platens and spacers, the machine frame deformation, and the deformation of each contact pair of specimen, platens,

spacers and load cell. As a consequence, the calculated strain is not the true strain of the specimen. Given the low stress levels, and hence small maximum forces reached during these tests, it is assumed that the machine, platen, and spacer deformations are small, and essentially the same during all tests. All the tests follow ASTM D3967-95a, except for tests in which the applied displacement rate is intentionally changed (increased or reduced). Such accelerated or slowed down tests are performed in order to study strain rate dependency of rock strength. Fig. 6.1 shows a specimen in the frame for a Brazilian test.

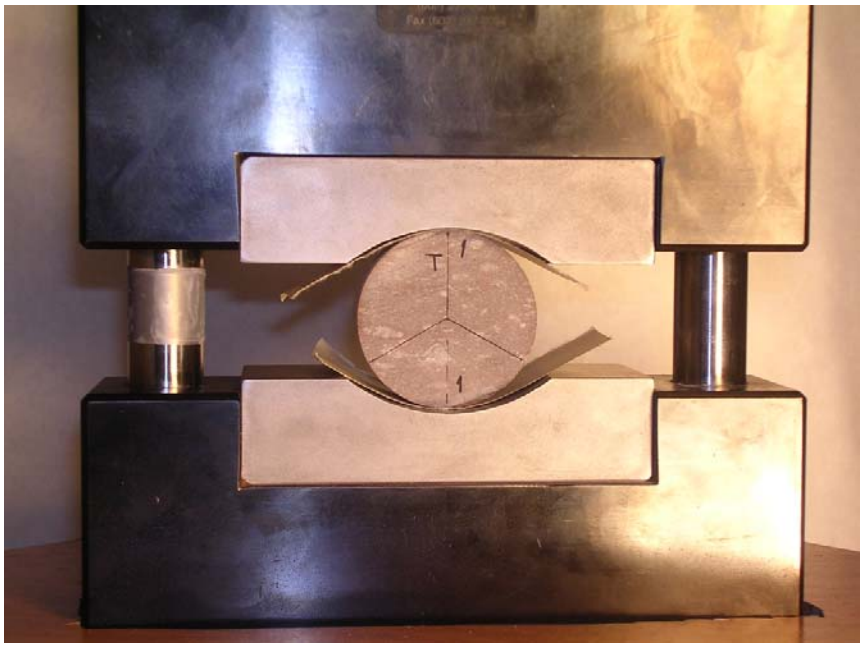

Figure 6.1 Example of a specimen considered not to contain major obvious flaws, although vapor altered “inclusions” (“spots”) are clearly visible.

The specimen sits between the bearing blocks. Bearing strips (cardboard) are used between the contact surfaces of the specimen and bearing blocks to transfer the load more evenly, and reduce the stress concentration on the contact surface of the specimen. This is

more important for brittle rocks. Of the tests, fifteen did not use bearing strips in order to test the effect of the bearing strips. One specimen was broken accidentally before getting the results.

6.2 Test results and analysis

6.2.1 Tensile strength

The splitting tensile strength of a specimen is calculated from Eq 6.1 (ASTM D 3967-95a) if the failure is a true splitting failure, i.e. a tension crack running diametrically between the loading points.

$$\sigma_t = \frac{2 \times P}{\pi \times L \times D} \tag{6.1}$$

where:

σ_t = splitting (Brazilian) tensile strength, MPa (psi),

P = load at (splitting) failure, N (lbf),

L = average specimen thickness, mm (inch), and

D = diameter, mm (inch).

The tests are categorized into three groups. Group 1 refers to the tests for which bearing strips were used and for which the specimens do not contain major obvious flaws. One hundred and twelve tests fall in this group. Seventy seven of those are tested at the

standard loading rate (the total test duration is between 1 and 10 minutes, as required by ASTM D 3967–95a). Group 2 includes the tests for which no bearing strips were used and for which the specimens are judged not to contain major flaws. Group 3 contains the tests for which bearing strips were used and for which there are flaws in the specimens. Table 6.3 gives the strengths for the three groups for tests conducted at the standard loading rate.

Table 6.3 Statistical summary of Brazilian tests at standard loading rate

	Group 1 (no flaws and with bearing strips)	Group 2 (no flaws and no bearing strips)	Group 3 (with flaws and with bearing strips)
Minimum	10.13	8.80	4.51
Maximum	22.69	19.46	21.61
Number of specimens	77	15	25
Mean	16.92	14.65	10.93
Median	16.85	14.71	10.93
Std Deviation	2.70	3.45	3.68

The mean strength of Group 1 is the highest, and of Group 3 the lowest. Group 1 has the lowest standard deviation. This comparison shows the effect of bearing strips and the effect of flaws in specimens. It appears that omitting the bearing strips clearly reduces the strength (13.42% in average, comparing Group 2 and Group 1). It is obvious that the presence of visible large flaws significantly reduces the strength (35.4% in average, comparing Group 3 and Group 1).

Fig. 6.2 shows a typical failure pattern for the specimens in Group 1. A main fracture runs between the loading points and near the central vertical axis of the specimen. In

addition, two curved fractures symmetric about the main fracture are generated almost at the same time as the main fracture. The overwhelming majority of specimens in Group 1 show this classical (e.g. Andreev, 1995, Fig. 4.39) failure pattern.

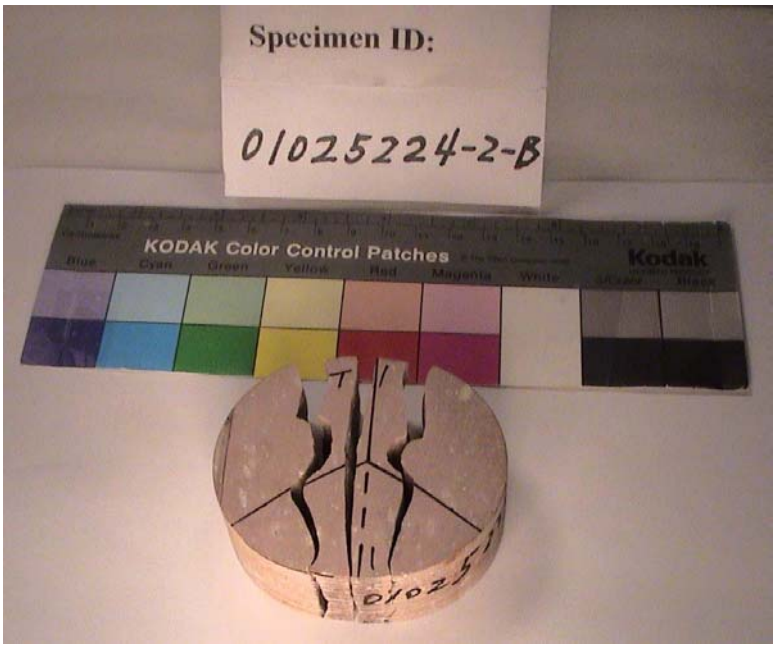

Figure 6.2 A typical failure pattern of specimens of Group1

A simulation has been performed using ANSYS 8.0, a finite element code. Before doing the simulation, a number of technical problems regarding finite element modeling were discussed with Dr. Shen-Yi Luo who is a professor in the Department of Mechanical Engineering, University of Nevada, Reno. He is also in the author's Doctoral Advisory Committee. The ANSYS8.0 was used under his permission. Figs. 6.3 and 6.4 are von Mises stress contour plots. When load is applied on the specimen, the maximum compressive stress occurs at the loading points (Fig. 6.3). The stress paths between the loading points are fairly similar to the fracture path shown in Fig. 6.2. With the increase

of the load, the concentrated stress spread out. The maximum compressive stress transferred to two points at each end of the specimen (Fig.6.4).

Based on the simulation, it can be judged that the fractures are initiated at the ends of the specimen. The fracture in the midwidth is initiated first. When running a test, this process occurred too quickly to be observed by naked eye. This judgment may be verified by the comparison between Group1 and Group 2 (Table 6.3). The only difference between the groups is whether the bearing strips are used. Specimens in Group1 tested with bearing strips got a higher average strength. The bearing strips only affect the ends of a specimen. In other words, the stress distributions at the center of a specimen should be no different no matter there are bearing strips installed, according to St. Venant's Principle.

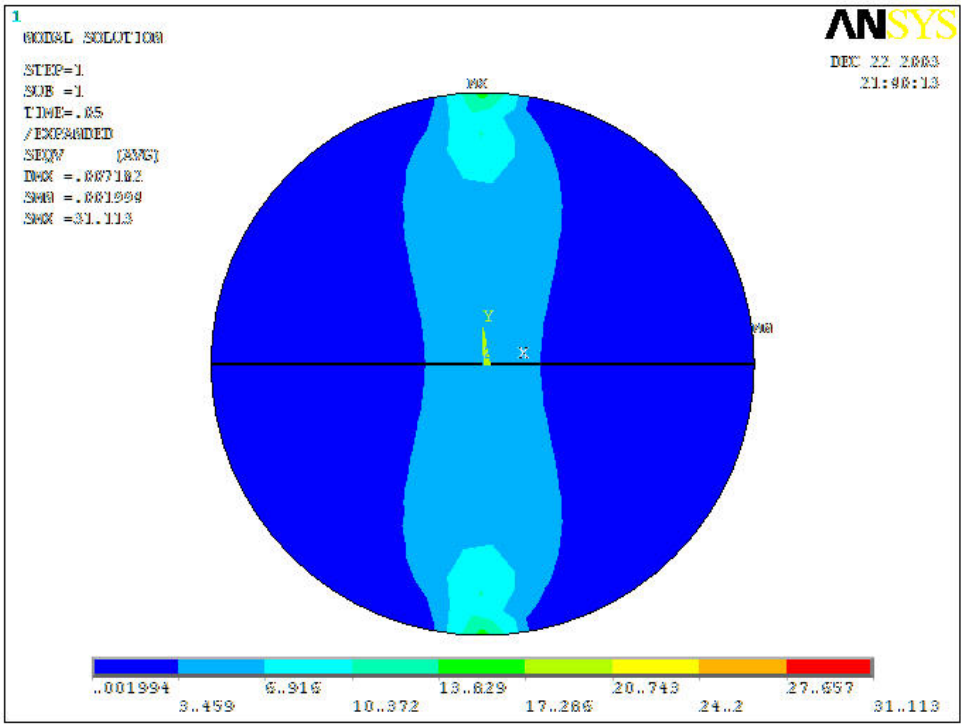

Figure 6.3 A von Mises stress contour plot at the beginning of loading

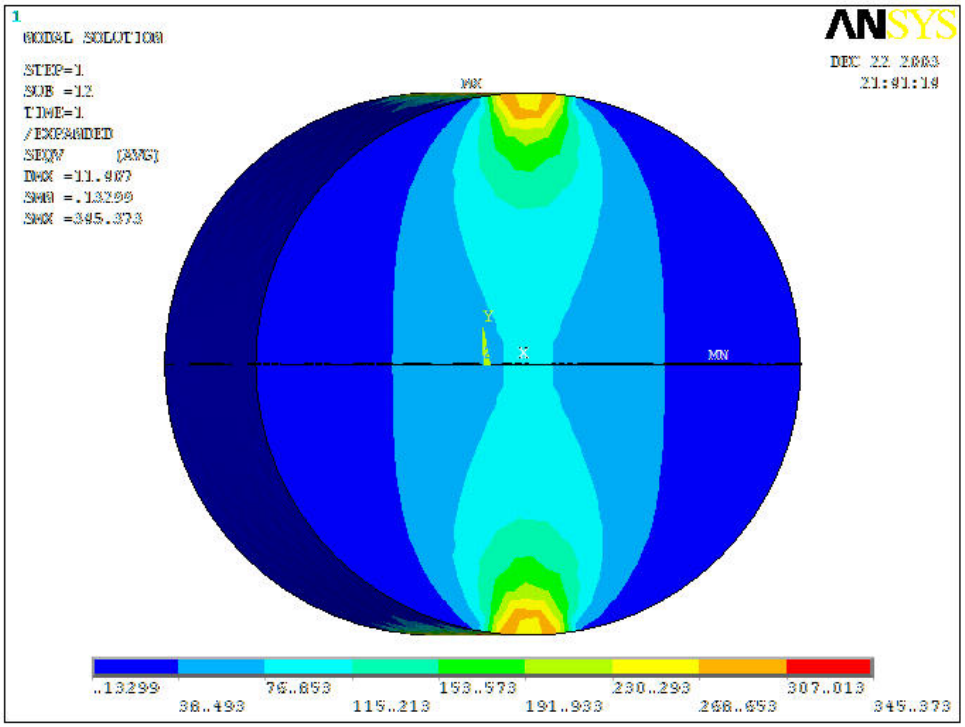

Figure 6.4 A von Mises stress contour plot showing stress concentration at the ends of a specimen

Figs. 6.5 and 6.6 show the stress distributions along the x-axis in the midheight of the specimen in the horizontal direction (Fig. 6.5) and the vertical direction (Fig. 6.6). Positive value is given for tensile stress. In Fig. 6.5, the maximum tensile stress occurs in the center of the specimen. The magnitude of the maximum tensile stress is calculated by Eq. 6.1. Fig. 6.6 indicates that the maximum compressive stress occurs in the center of the specimen as well.

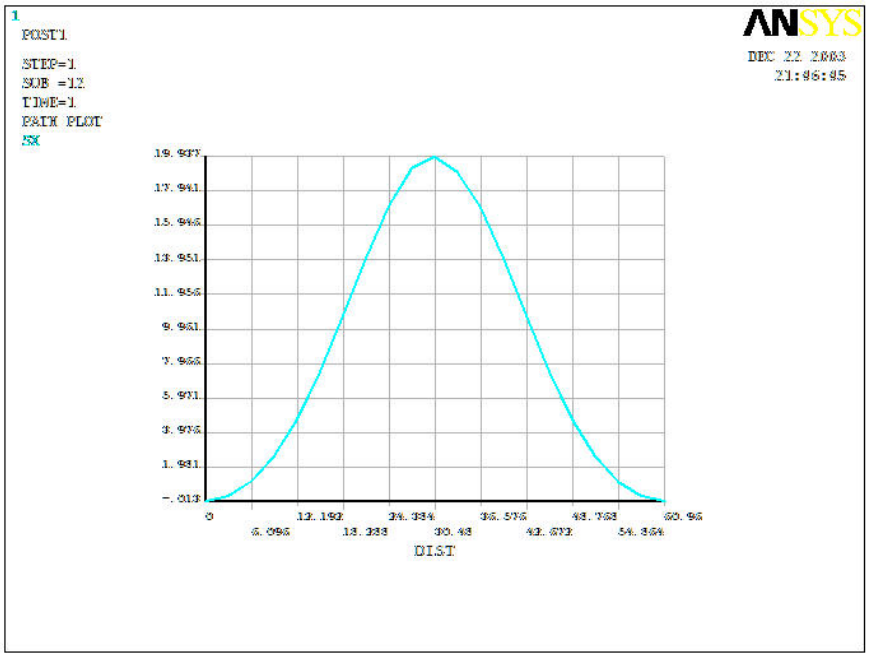

Figure 6.5 Stress in horizontal direction (σ_x) along the x-axis in the midheight of the specimen

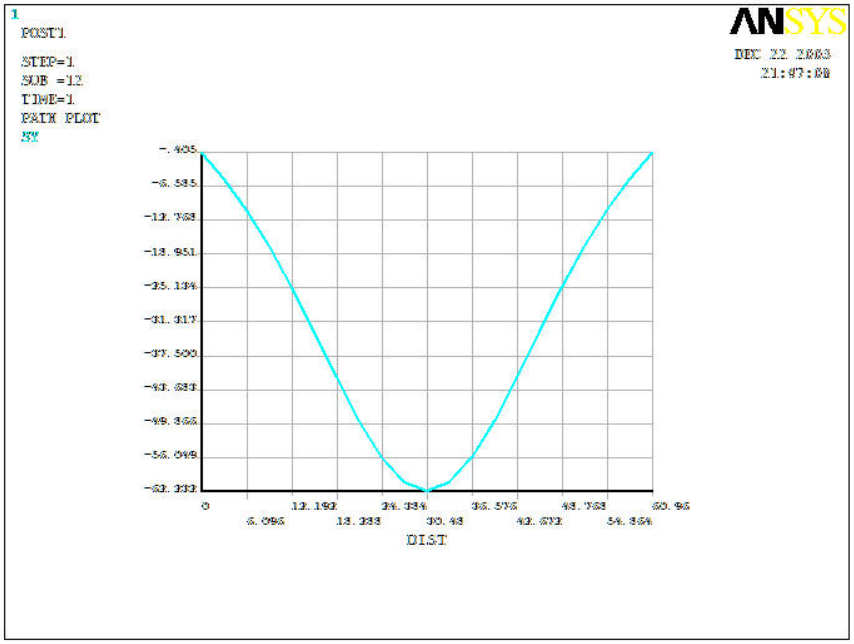

Figure 6.6 Stress in vertical direction (σ_y) along the x-axis in the midheight of the specimen

Figs. 6.7 and 6.8 give the plots of stresses in horizontal and vertical direction along y-axis. Both plots indicate the compressive stress at the ends of the specimen much higher than the stress at the center.

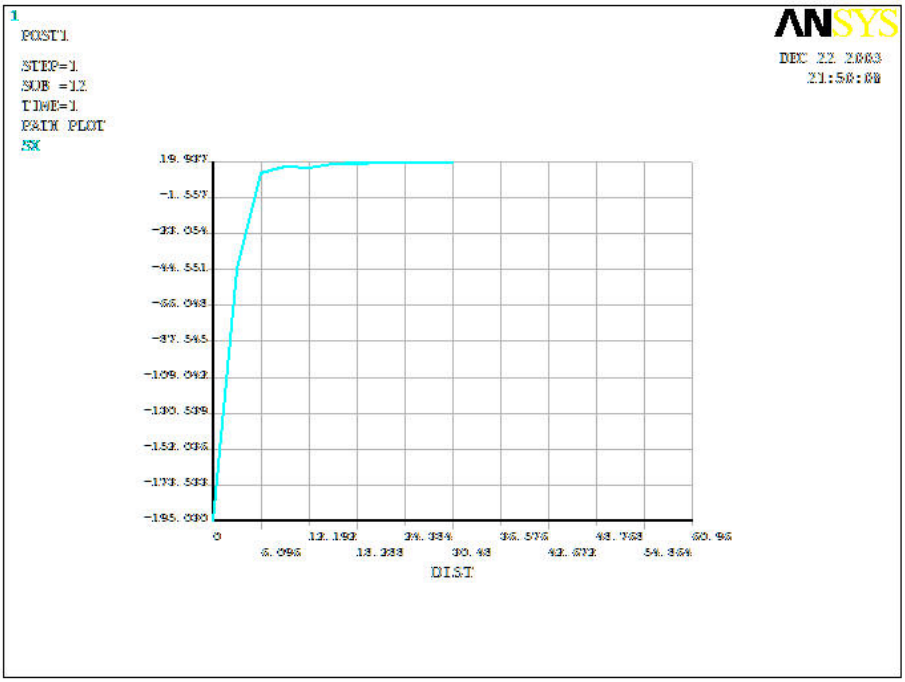

Figure 6.7 Stress in horizontal direction (σ_x) along y-axis in the midwidth of the specimen

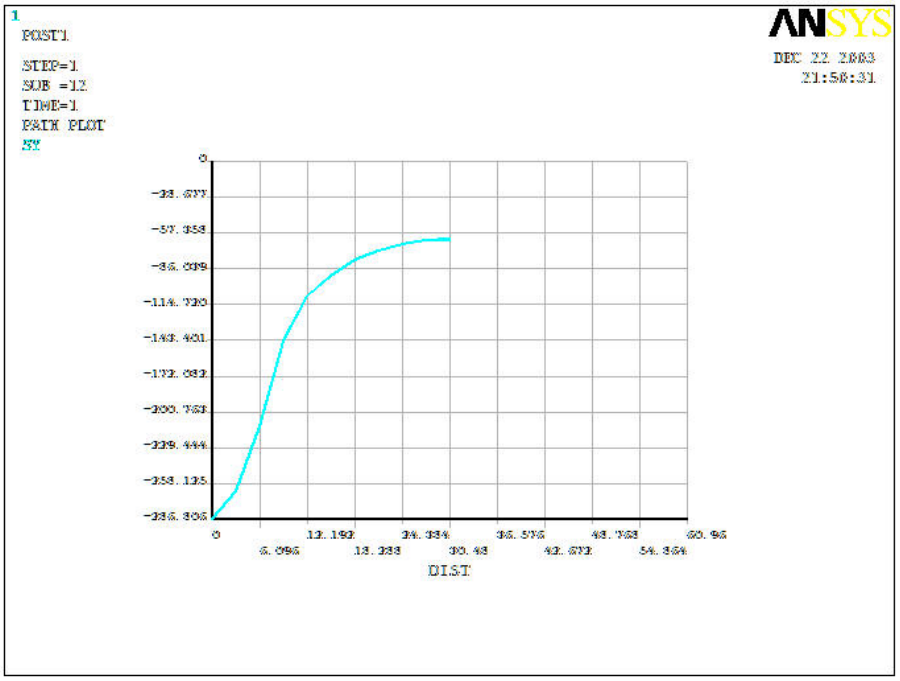

Figure 6.8 Stress in vertical direction (σ_y) along y-axis in midwidth of the specimen

The pattern shown in Fig. 6.9 also occurs frequently: another two short fractures develop near the upper loading end of the specimen (see Fig. 6.1). The upper loading end is where the machine piston is located. Very likely these short fractures are resulted from bending. The short fractures are generated after the three long fractures. After the three long fractures are formed, there is a strong tendency for the rock pieces at farthest left and farthest right to split away from the central vertical axis. At this moment the bearing block at the upper loading end is still moving down owing to inertia of the piston in testing machine. As a consequence a heavy restriction is applied to the splitting rock pieces by the curved surface of the bearing block. The short fractures shown in Fig. 6.9 do not occur when running tests for smaller diameter (1.78 inch or 45.21 mm) specimens.

Figure 6.9 A fracture pattern that occurs frequently for 2.4 inch (60.96 mm) diameter specimens

Weakness inclusions affect the strength and failure pattern significantly. The vapor-phase altered spot on the left side of the specimen in Fig. 6.10 results in only one “diametrical” fracture developing. This type of asymmetric “diametrical” fracture, curving away from the center of the specimen, has been observed fairly frequently. A secondary, probably bending, fracture has formed through the left half of the specimen, most likely as a result of a stress concentration at the edge of the vapor-altered weakened zone.

Figure 6.10 Effect of weakness inclusion on the failure pattern of a specimen: tensile failure of left part, assumed induced by weak (white) spot on left outer edge of specimen (Splitting tensile strength = 18.2 MPa).

Fig. 6.11 shows a case in which a vapor-phase altered zone was hidden inside and near the center of the specimen. In this example only one straight vertical fracture develops, through the weakness inclusion, and the specimen has a rather low strength.

Figure 6.11 Effect of weakness inclusion on the failure pattern of a specimen (Splitting tensile strength = 8.5 MPa)

6.2.2 Strain rate dependence

The strain rate-dependence of tensile strength has been studied. Only the results of tests in Group 1 are used for this purpose. Fig. 6.12 shows a plot of tensile strength versus strain rate in logarithmic scale. As mentioned previously, the strain is not the true strain. Because the strain is calculated from a displacement that includes the test system deformation, the strain calculated and used here is somewhat larger than the actual strain. As a summary of strain rate-dependence, Fig. 6.12 is still valuable. The tensile strength decreases with a decrease of the strain rate. In other words, it decreases with an increase of test duration.

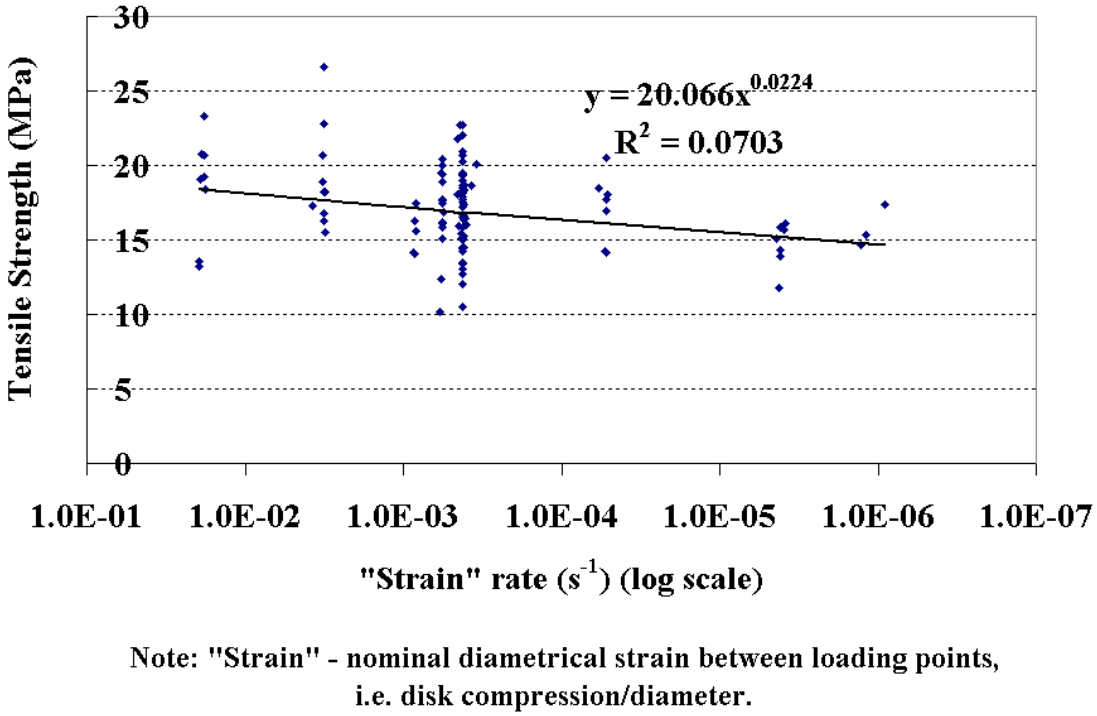

Figure 6.12 Tensile strength versus "strain rate" showing time-dependence of the tensile strength

6.3 Recommendations for further study

1) Use Brazilian test data for spatial variability studies.

2) Use Brazilian test data to analyze rock stiffness, possibly determine Young's modulus.

3) Perform static fatigue Brazilian tests.

4) Study properties as a function of moisture content, density (porosity) and specimen volume.

5) Compare indirect tensile splitting strengths with uniaxial compressive strengths. Evaluate whether empirical relations in literature are acceptable for these tuffs, or whether they might need to be modified.

6) Evaluate whether compressive and tensile strength (and stiffness) strain rate dependency can be (cor)related.

7) Correlate Brazilian and lump test tensile strength results.

8) Evaluate whether it is possible to evaluate numerically the influence of vapor altered spots on strength and stiffness.

9) Perform numerical analyses of tests on specimens with modeled vapor altered spots, and performance sensitivity analyses.

10) Evaluate whether it is possible to numerically reconcile strength and stiffness of specimens weakened and softened by vapor phase altered spots, by performing numerical simulations of such tests.

Table 6.1 Summary of Specimen Source Information for Brazilian tests

Serial #	Specimen ID	Borehole	Range in Borehole (ft)	Zone
1	01014733-1-B	UE-25 UZ#16	817.9-818.8	Tptpll
2	01014764-1-B	USW WZ-14	1076.1-1076.9	Tptpll
3	01014764-3-B	USW WZ-14	1076.1-1076.9	Tptpll
4	01023357-2-B	ESF-MD-NICHE 4788#1	3.3-3.8	Tptpmn
5	01023359-2-B	ESF-MD-NICHE 4788#1	15.7-16.5	Tptpmn
6	01023359-3-B	ESF-MD-NICHE 4788#1	15.7-16.5	Tptpmn
7	01023363-4-B	ESF-MD-NICHE 3107#7	12.1-13.6	Tptpmn
8	01023363-5-B	ESF-MD-NICHE 3107#7	12.1-13.6	Tptpmn
9	01023363-6-B	ESF-MD-NICHE 3107#7	12.1-13.7	Tptpmn
10	01023367-3-B	ESF-MD-NICHE 3107#7	8.1-9.6	Tptpmn
11	01023367-4-B	ESF-MD-NICHE 3107#7	8.1-9.6	Tptpmn
12	01023367-5-B	ESF-MD-NICHE 3107#7	8.1-9.6	Tptpmn
13	01023370-2-B	ESF-MD-NICHE 3107#7	20.9-21.5	Tptpmn
14	01023370-3-B	ESF-MD-NICHE 3107#7	20.9-21.5	Tptpmn
15	01023372-3-B	ESF-MD-NICHE 3107#7	22.7-23.4	Tptpmn
16	01023566-2-B	ESF-HD-WH-3	0.2-1.1	Tptpmn
17	01023567-2-B	ESF-HD-WH-3	2.0-2.9	Tptpmn
18	01023567-3-B	ESF-HD-WH-3	2.0-2.9	Tptpmn
19	01023567-4-B	ESF-HD-WH-3	2.0-2.9	Tptpmn
20	01023570-2-B	ESF-HD-WH-3	24.2-25.7	Tptpmn
21	01023570-3-B	ESF-HD-WH-3	24.2-25.7	Tptpmn
22	01023570-4-B	ESF-HD-WH-3	24.2-25.7	Tptpmn
23	01023571-1-B	ESF-HD-WH-3	27.2-27.9	Tptpmn
24	01023571-2-B	ESF-HD-WH-3	27.2-27.9	Tptpmn
25	01023571-3-B	ESF-HD-WH-3	27.2-27.9	Tptpmn
26	01023571-4-B	ESF-HD-WH-3	27.2-27.9	Tptpmn
27	01023574-1-B	ESF-HD-WH-4	15.6-16.3	Tptpmn
28	01023574-2-B	ESF-HD-WH-4	15.6-16.3	Tptpmn
29	01023574-3-B	ESF-HD-WH-4	15.6-16.3	Tptpmn
30	01023574-4-B	ESF-HD-WH-4	15.6-16.3	Tptpmn
31	01023574-5-B	ESF-HD-WH-4	15.6-16.3	Tptpmn
32	01023574-6-B	ESF-HD-WH-4	15.6-16.3	Tptpmn
33	01023574-7-B	ESF-HD-WH-4	15.6-16.3	Tptpmn
34	01023576-1-B	ESF-HD-WH-4	33.0-34.1	Tptpmn
35	01023579-2-B	ESF-HD-WH-5	12.4-13.0	Tptpmn
36	01023580-1-B	ESF-HD-WH-5	24.4-25.0	Tptpmn
37	01023581-1-B	ESF-HD-WH-5	27.7-28.4	Tptpmn
38	01023581-3-B	ESF-HD-WH-5	27.7-28.4	Tptpmn
39	01023581-4-B	ESF-HD-WH-5	27.7-28.4	Tptpmn
40	01023582-2-B	ESF-HD-WH-5	33.0-34.2	Tptpmn
41	01023585-1-B	ESF-HD-WH-6	28.2-28.9	Tptpmn

Table 6.1 (Continued)

42	01023585-2-B	ESF-HD-WH-6	28.2-28.9	Tptpmn
43	01023586-1-B	ESF-HD-WH-3	31.0-31.6	Tptpmn
44	01023586-2-B	ESF-HD-WH-3	31.0-31.6	Tptpmn
45	01023657-6-B	ESF-HD-WH-36	15.9-18.3	Tptpmn
46	01023657-7-B	ESF-HD-WH-36	15.6-18.3	Tptpmn
47	01023657-8-B	ESF-HD-WH-36	15.9-18.3	Tptpmn
48	01023658-1-B	ESF-HD-WH-36	18.8-20.2	Tptpmn
49	01023658-2-B	ESF-HD-WH-36	18.8-20.2	Tptpmn
50	01023658-3-B	ESF-HD-WH-36	18.8-20.2	Tptpmn
51	01023658-4-B	ESF-HD-WH-36	18.8-20.2	Tptpmn
52	01023658-5-B	ESF-HD-WH-36	18.8-20.2	Tptpmn
53	01023658-6-B	ESF-HD-WH-36	18.8-20.2	Tptpmn
54	01023661-1-B	ESF-HD-WH-36	30.5-31.8	Tptpmn
55	01023661-2-B	ESF-HD-WH-36	26.0-26.7	Tptpmn
56	01023661-3-B	ESF-HD-WH-36	26.0-26.7	Tptpmn
57	01023666-1-B	ESF-HD-WH-37	0.0-0.4	Tptpmn
58	01023666-2-B	ESF-HD-WH-37	0.0-0.4	Tptpmn
59	01023666-3-B	ESF-HD-WH-37	0.0-0.4	Tptpmn
60	01023666-4-B	ESF-HD-WH-37	0.0-0.4	Tptpmn
61	01023668-1-B	ESF-HD-WH-37	2.2-4.4	Tptpmn
62	01023668-2-B	ESF-HD-WH-37	2.2-4.4	Tptpmn
63	01023668-4-B	ESF-HD-WH-37	2.2-4.4	Tptpmn
64	01023668-5-B	ESF-HD-WH-37	2.2-4.4	Tptpmn
65	01023668-6-B	ESF-HD-WH-37	2.2-4.4	Tptpmn
66	01023668-7-B	ESF-HD-WH-37	2.2-4.4	Tptpmn
67	01023668-8-B	ESF-HD-WH-37	2.2-4.4	Tptpmn
68	01023685-1-B	ESF-HD-WH-37	9.8-11.0	Tptpmn
69	01023685-2-B	ESF-HD-WH-37	9.8-11.0	Tptpmn
70	01023685-3-B	ESF-HD-WH-37	9.8-11.0	Tptpmn
71	01023685-4-B	ESF-HD-WH-37	9.8-11.0	Tptpmn
72	01023685-5-B	ESF-HD-WH-37	9.8-11.0	Tptpmn
73	01023685-6-B	ESF-HD-WH-37	9.8-11.0	Tptpmn
74	01023685-7-B	ESF-HD-WH-37	9.8-11.0	Tptpmn
75	01023685-8-B	ESF-HD-WH-37	9.8-11.0	Tptpmn
76	01023689-3-B	ESF-HD-WH-37	19.6-21.1	Tptpmn
77	01023689-4-B	ESF-HD-WH-37	19.6-21.1	Tptpmn
78	01023689-5-B	ESF-HD-WH-37	19.6-21.1	Tptpmn
79	01023689-6-B	ESF-HD-WH-37	19.6-21.1	Tptpmn
80	01023689-7-B	ESF-HD-WH-37	19.6-21.1	Tptpmn
81	01023690-2-B	ESF-HD-WH-37	22.7-23.7	Tptpmn
82	01023690-3-B	ESF-HD-WH-37	22.7-23.7	Tptpmn
83	01023690-4-B	ESF-HD-WH-37	22.7-23.7	Tptpmn

Table 6.1 (Continued)

84	01023690-5-B	ESF-HD-WH-37	22.7-23.7	Tptpmn
85	01023693-1-B	ESF-HD-WH-37	27.6-28.1	Tptpmn
86	01023693-2-B	ESF-HD-WH-37	27.6-28.1	Tptpmn
87	01023697-2-B	ESF-HD-WH-50	4.8-6.0	Tptpmn
88	01023697-3-B	ESF-HD-WH-50	4.8-6.0	Tptpmn
89	01023697-4-B	ESF-HD-WH-50	4.8-6.0	Tptpmn
90	01023701-2-B	ESF-HD-WH-50	11.9-13.0	Tptpmn
91	01023701-3-B	ESF-HD-WH-50	11.9-13.0	Tptpmn
92	01023701-4-B	ESF-HD-WH-50	11.9-13.0	Tptpmn
93	01023702-1-B	ESF-HD-WH-50	15.1-16.2	Tptpmn
94	01023704-1-B	ESF-HD-WH-50	18.3-19.1	Tptpmn
95	01023704-3-B	ESF-HD-WH-50	18.3-19.1	Tptpmn
96	01023704-4-B	ESF-HD-WH-50	18.3-19.1	Tptpmn
97	01023704-5-B	ESF-HD-WH-50	18.3-19.1	Tptpmn
98	01023704-6-B	ESF-HD-WH-50	18.3-19.1	Tptpmn
99	01023704-7-B	ESF-HD-WH-50	18.3-19.1	Tptpmn
100	01023704-8-B	ESF-HD-WH-50	18.3-19.1	Tptpmn
101	01023704-9-B	ESF-HD-WH-50	18.3-19.1	Tptpmn
102	01023715-1-B	ESF-HD-WH-50	32.1-33.0	Tptpmn
103	01023715-2-B	ESF-HD-WH-50	32.1-33.0	Tptpmn
104	01023715-3-B	ESF-HD-WH-50	32.1-33.0	Tptpmn
105	01023715-4-B	ESF-HD-WH-50	32.1-33.0	Tptpmn
106	01023721-1-B	ESF-HD-WH-50	35.4-35.8	Tptpmn
107	01023721-2-B	ESF-HD-WH-50	35.4-35.8	Tptpmn
108	01023727-1-B	ESF-HD-WH-26	4.9-5.2	Tptpmn
109	01023727-2-B	ESF-HD-WH-26	4.9-5.2	Tptpmn
110	01023734-1-B	ESF-HD-WH-26	15.5-16.0	Tptpmn
111	01023734-2-B	ESF-HD-WH-26	15.5-16.0	Tptpmn
112	01023734-3-B	ESF-HD-WH-26	15.5-16.0	Tptpmn
113	01023734-4-B	ESF-HD-WH-26	15.5-16.0	Tptpmn
114	01023734-5-B	ESF-HD-WH-26	15.5-16.0	Tptpmn
115	01023735-1-B	ESF-HD-WH-26	14.1-14.4	Tptpmn
116	01023735-2-B	ESF-HD-WH-4	26.1-27.3	Tptpmn
117	01023735-3-B	ESF-HD-WH-26	14.1-14.4	Tptpmn
118	01023741-1-B	ESF-HD-WH-26	22.6-22.8	Tptpmn
119	01023741-2-B	ESF-HD-WH-26	22.6-22.8	Tptpmn
120	01023744-1-B	ESF-HD-WH-26	24.1-24.4	Tptpmn
121	01023744-2-B	ESF-HD-WH-26	24.1-24.4	Tptpmn
122	01023746-1-B	ESF-HD-WH-26	25.2-25.5	Tptpmn
123	01023746-2-B	ESF-HD-WH-26	25.2-25.5	Tptpmn
124	01023746-3-B	ESF-HD-WH-26	25.2-25.5	Tptpmn
125	01023747-2-B	ESF-HD-WH-26	25.7-26.8	Tptpmn

Table 6.1 (Continued)

126	01023747-4-B	ESF-HD-WH-26	25.7-26.8	Tptpmn
127	01023748-1-B	ESF-HD-WH-26	29.0-29.3	Tptpmn
128	01023748-2-B	ESF-HD-WH-26	29.0-29.3	Tptpmn
129	01023754-1-B	ESF-HD-WH-32	4.7-5.7	Tptpmn
130	01023754-3-B	ESF-HD-WH-32	4.7-5.7	Tptpmn
131	01023755-1-B	ESF-HD-WH-32	9.0-9.3	Tptpmn
132	01023755-2-B	ESF-HD-WH-32	9.0-9.3	Tptpmn
133	01023755-3-B	ESF-HD-WH-32	9.0-9.3	Tptpmn
134	01023756-1-B	ESF-HD-WH-32	9.6-9.7	Tptpmn
135	01023756-2-B	ESF-HD-WH-32	9.6-9.7	Tptpmn
136	01023757-1-B	ESF-HD-WH-32	9.9-10.2	Tptpmn
137	01023757-2-B	ESF-HD-WH-32	9.9-10.2	Tptpmn
138	01025222-B	ESF-HD-WH-32	16.1-16.2	Tptpmn
139	01025224-2-B	ESF-HD-WH-32	27.2-28.8	Tptpmn
140	01025224-3-B	ESF-HD-WH-32	27.2-28.8	Tptpmn
141	01025226-2-B	ESF-HD-WH-32	32.0-33.1	Tptpmn
142	01025226-3-B	ESF-HD-WH-32	32.0-33.1	Tptpmn
143	01025226-4-B	ESF-HD-WH-32	32.0-33.1	Tptpmn
144	01025226-5-B	ESF-HD-WH-32	32.0-33.1	Tptpmn
145	01025227-3-B	ESF-HD-WH-32	33.8-35.6	Tptpmn
146	01025227-4-B	ESF-HD-WH-32	33.8-35.6	Tptpmn
147	01025227-5-B	ESF-HD-WH-32	33.8-35.6	Tptpmn
148	01025228-1-B	ESF-HD-WH-32	37.4-37.6	Tptpmn
149	01025228-2-B	ESF-HD-WH-32	37.4-37.6	Tptpmn
150	01025228-3-B	ESF-HD-WH-32	37.4-37.6	Tptpmn
151	01025229-1-B	ESF-HD-WH-32	35.8-36.2	Tptpmn
152	01025229-2-B	ESF-HD-WH-32	35.8-36.2	Tptpmn
153	01025229-3-B	ESF-HD-WH-32	35.8-36.2	Tptpmn
154	01025229-4-B	ESF-HD-WH-32	35.8-36.2	Tptpmn
155	01025232-2-B	ESF-HD-WH-33	10.2-10.9	Tptpmn
156	01025232-3-B	ESF-HD-WH-33	10.2-10.9	Tptpmn
157	01025232-4-B	ESF-HD-WH-33	10.2-10.9	Tptpmn
158	01025261-3-B	ESF-HD-WH-33	25.8-26.5	Tptpmn

Note: Tptpll = lower lithophysal zone of Topopah Spring Tuff,
Tptpmn = middle nonlithophysal zone of Topopah Spring Tuff.

Table 6.2 Summary of Brazilian tests

Serial #	Specimen ID	Specimen Code *	Test Code **	Diameter (in)	Thickness (in)	Strength (MPa)	"Strain" Rate (/s)	Moisture Content (%)
1	01014733-1-B	0	0	2.40	0.99	10.13	0.000589	N/A
2	01014764-1-B	1	0	2.40	1.23	8.50	0.000418	N/A
3	01014764-3-B	1	0	2.40	1.31	6.87	0.000419	N/A
4	01023357-2-B	0	0	1.77	1.05	12.39	0.000575	N/A
5	01023359-2-B	0	0	1.77	0.95	16.22	0.000567	N/A
6	01023359-3-B	0	0	1.77	0.68	18.87	0.000569	N/A
7	01023363-4-B	0	0	1.78	0.82	15.12	0.000565	N/A
8	01023363-5-B	0	0	1.78	0.63	19.51	0.000573	N/A
9	01023363-6-B***	0	0	1.78	0.67	N/A	N/A	N/A
10	01023367-3-B	0	0	1.78	0.57	19.41	0.000566	N/A
11	01023367-4-B	0	0	1.78	0.59	17.49	0.000566	N/A
12	01023367-5-B	0	0	1.78	0.72	20.00	0.000570	N/A
13	01023370-2-B	0	0	1.78	0.64	20.43	0.000566	N/A
14	01023370-3-B	0	0	1.78	0.68	17.65	0.000565	N/A
15	01023372-3-B	0	0	1.78	0.68	15.87	0.000571	N/A
16	01023566-2-B	0	0	2.40	0.90	13.38	0.000425	0.652
17	01023567-2-B	0	0	2.40	1.06	17.73	0.000569	N/A
18	01023567-3-B	1	0	2.40	1.14	10.23	0.000559	N/A
19	01023567-4-B	1	0	2.40	1.14	11.21	0.000564	N/A
20	01023570-2-B	1	0	2.40	0.87	12.14	0.000421	N/A
21	01023570-3-B	0	0	2.38	1.01	20.04	0.000567	N/A
22	01023570-4-B	0	0	2.39	0.74	19.01	0.000423	N/A
23	01023571-1-B	0	0	2.40	1.04	15.67	0.000004	0.819
24	01023571-2-B	0	0	2.40	1.04	13.50	0.000419	0.901
25	01023571-3-B	0	0	2.40	1.10	16.25	0.003195	0.932

Table 6.2 (Continued)

26	01023571-4-B	0	0	2.40	1.01	12.06	0.000421	0.952
27	01023574-1-B	1	1	2.40	1.42	9.22	0.000419	0.679
28	01023574-2-B	0	0	2.40	1.00	16.03	0.000402	0.936
29	01023574-3-B	0	0	2.40	1.05	14.66	0.000001	0.816
30	01023574-4-B	0	0	2.40	0.87	18.47	0.000058	0.858
31	01023574-5-B	0	1	2.40	0.99	14.59	0.000418	1.008
32	01023574-6-B	0	0	2.40	0.96	18.63	0.000417	0.931
33	01023574-7-B	0	0	2.40	1.09	20.25	0.000423	0.808
34	01023576-1-B	1	0	2.40	1.30	4.51	0.000556	N/A
35	01023579-2-B	0	0	2.40	1.16	18.62	0.000373	N/A
36	01023580-1-B	0	0	2.40	1.17	15.41	0.000427	N/A
37	01023581-1-B	0	0	2.40	1.22	19.46	0.000418	N/A
38	01023581-3-B	0	0	2.40	1.16	16.85	0.000557	N/A
39	01023581-4-B	0	0	2.40	1.29	16.13	0.000564	N/A
40	01023582-2-B	0	0	2.40	0.98	20.06	0.000347	N/A
41	01023585-1-B	0	0	2.40	1.12	22.69	0.000419	0.552
42	01023585-2-B	0	0	2.40	1.08	20.71	0.017992	0.658
43	01023586-1-B	1	0	2.40	1.13	9.84	0.000423	N/A
44	01023586-2-B	0	0	2.31	1.00	15.91	0.000444	N/A
45	01023657-6-B	0	0	2.40	0.98	13.87	0.000004	0.864
46	01023657-7-B	0	0	2.40	0.93	14.27	0.000053	0.925
47	01023657-8-B	0	0	2.40	1.06	18.10	0.000420	0.801
48	01023658-1-B	0	0	2.40	0.68	15.47	0.003099	N/A
49	01023658-2-B	0	0	2.40	1.05	18.24	0.003153	N/A
50	01023658-3-B	0	0	2.40	0.85	19.04	0.019150	N/A
51	01023658-4-B	0	0	2.40	0.89	18.08	0.000051	N/A
52	01023658-5-B	1	0	2.40	1.24	8.47	0.003280	N/A

Table 6.2 (Continued)

53	01023658-6-B	0	0	2.40	0.67	26.62	0.003194	N/A
54	01023661-1-B	0	1	2.40	1.09	15.67	0.000418	0.679
55	01023661-2-B	0	0	2.40	1.08	12.72	0.000420	0.625
56	01023661-3-B	0	0	2.40	1.14	11.74	0.000004	0.662
57	01023666-1-B	1	0	2.40	1.08	16.93	0.000420	N/A
58	01023666-2-B	1	0	2.40	0.88	21.61	0.000418	N/A
59	01023666-3-B	0	0	2.40	0.85	23.31	0.018229	N/A
60	01023666-4-B	1	0	2.40	0.88	13.13	0.000421	N/A
61	01023668-1-B	0	0	2.40	1.24	15.59	0.000825	N/A
62	01023668-2-B	0	0	2.40	0.75	16.28	0.000843	N/A
63	01023668-4-B	0	0	2.40	0.85	17.37	0.000001	N/A
64	01023668-5-B	0	0	2.40	0.88	16.97	0.000052	N/A
65	01023668-6-B	1	0	2.40	1.00	11.68	0.000424	N/A
66	01023668-7-B	1	0	2.40	0.82	15.24	0.000414	N/A
67	01023668-8-B	0	0	2.40	0.87	22.81	0.003183	N/A
68	01023685-1-B	0	0	2.40	1.11	13.25	0.019444	0.943
69	01023685-2-B	0	0	2.40	0.94	20.68	0.003247	0.807
70	01023685-3-B	0	1	2.40	0.97	14.71	0.000418	0.948
71	01023685-4-B	0	0	2.40	1.08	18.27	0.000421	0.983
72	01023685-5-B	0	1	2.40	0.95	14.07	0.000402	0.988
73	01023685-6-B	1	0	2.40	0.90	7.85	0.000418	1.145
74	01023685-7-B	1	0	2.40	0.97	7.00	0.000418	1.221
75	01023685-8-B	0	1	2.40	0.95	18.89	0.000416	1.066
76	01023689-3-B	0	0	2.40	1.10	15.28	0.000418	0.708
77	01023689-4-B	0	0	2.40	1.11	16.57	0.000419	0.842
78	01023689-5-B	0	0	2.40	1.04	16.66	0.000419	0.924
79	01023689-6-B	1	0	2.40	1.06	13.27	0.000416	0.830

Table 6.2 (Continued)

80	01023689-7-B	0	0	2.40	1.00	18.32	0.000416	0.734
81	01023690-2-B	0	0	2.40	1.11	14.23	0.000419	0.703
82	01023690-3-B	0	1	2.40	1.04	17.79	0.000413	0.814
83	01023690-4-B	0	0	2.40	1.06	17.22	0.000420	0.722
84	01023690-5-B	0	0	2.40	1.06	18.04	0.000458	0.874
85	01023693-1-B	0	0	2.40	1.08	16.58	0.000417	0.818
86	01023693-2-B	1	1	2.40	1.09	8.80	0.000419	1.022
87	01023697-2-B	0	0	2.40	0.84	15.30	0.000001	0.806
88	01023697-3-B	0	1	2.40	0.84	17.32	0.000422	0.974
89	01023697-4-B	0	1	2.40	0.88	15.66	0.000414	0.992
90	01023701-2-B	0	0	2.40	1.04	16.34	0.000417	0.988
91	01023701-3-B	0	0	2.40	0.89	16.63	0.000414	1.030
92	01023701-4-B	0	0	2.40	0.97	17.74	0.000424	0.894
93	01023702-1-B	1	0	2.40	1.27	7.39	0.000415	0.921
94	01023704-1-B	0	0	2.40	1.19	14.52	0.000419	0.805
95	01023704-3-B	0	0	2.40	1.08	13.52	0.019360	N/A
96	01023704-4-B	0	0	2.40	0.86	14.09	0.000845	N/A
97	01023704-5-B	1	0	2.40	0.81	12.34	0.003108	N/A
98	01023704-6-B	0	0	2.40	0.80	14.15	0.000857	N/A
99	01023704-7-B	0	0	2.40	1.05	15.87	0.000004	N/A
100	01023704-8-B	0	0	2.40	0.73	14.19	0.000052	N/A
101	01023704-9-B	1	0	2.40	0.64	9.82	0.000421	N/A
102	01023715-1-B	0	0	2.40	1.06	16.41	0.000409	0.787
103	01023715-2-B	0	0	2.40	0.86	22.06	0.000420	0.635
104	01023715-3-B	0	0	2.40	0.83	14.44	0.000418	0.635
105	01023715-4-B	0	0	2.40	0.92	20.69	0.000420	0.693
106	01023721-1-B	0	0	2.40	1.01	20.49	0.000052	N/A

Table 6.2 (Continued)

107	01023721-2-B	0	0	2.40	0.93	15.16	0.000423	0.676
108	01023727-1-B	0	0	2.40	1.05	10.48	0.000420	0.541
109	01023727-2-B	0	1	2.40	0.87	17.25	0.000406	0.609
110	01023734-1-B	1	0	2.40	1.06	14.36	0.000419	N/A
111	01023734-2-B	1	0	2.40	0.78	11.81	0.000419	N/A
112	01023734-3-B	1	0	2.40	0.90	13.54	0.018836	N/A
113	01023734-4-B	0	0	2.40	0.94	18.39	0.017765	N/A
114	01023734-5-B	0	0	2.40	0.85	20.76	0.018964	N/A
115	01023735-1-B	0	0	2.40	0.98	19.33	0.000419	0.508
116	01023735-2-B	0	0	2.40	0.91	19.41	0.000419	0.474
117	01023735-3-B	0	0	2.40	1.29	14.27	0.000419	0.473
118	01023741-1-B	0	0	2.40	0.97	17.28	0.003721	0.747
119	01023741-2-B	0	0	2.40	0.85	14.47	0.000417	0.725
120	01023744-1-B	1	1	2.40	0.96	13.42	0.000413	0.761
121	01023744-2-B	0	0	2.40	0.79	15.05	0.000428	0.766
122	01023746-1-B	0	0	2.40	0.99	17.57	0.000420	0.776
123	01023746-2-B	0	0	2.40	0.86	18.63	0.000420	0.757
124	01023746-3-B	0	0	2.40	1.32	19.21	0.018188	0.677
125	01023747-2-B	0	0	2.40	1.22	18.24	0.003105	N/A
126	01023747-4-B	0	0	2.40	0.71	17.47	0.000837	N/A
127	01023748-1-B	0	0	2.40	1.04	21.74	0.000453	0.640
128	01023748-2-B	0	0	2.40	0.83	20.91	0.000421	0.630
129	01023754-1-B	0	0	2.40	0.99	18.45	0.000420	0.918
130	01023754-3-B	0	0	2.40	0.82	17.86	0.000419	0.921
131	01023755-1-B	1	0	2.40	1.04	8.62	0.000414	0.910
132	01023755-2-B	0	0	2.40	1.06	22.69	0.000441	0.997
133	01023755-3-B	1	0	2.40	1.22	10.67	0.000414	0.933

Table 6.2 (Continued)

134	01023756-1-B	0	0	2.40	0.85	15.05	0.000004	0.847
135	01023756-2-B	0	0	2.40	0.88	16.09	0.000004	0.894
136	01023757-1-B	0	1	2.40	0.98	14.05	0.000409	0.868
137	01023757-2-B	1	0	2.40	0.93	11.94	0.000395	1.076
138	01025222-B	1	1	2.40	1.50	8.81	0.000421	0.697
139	01025224-2-B	0	0	2.40	1.04	15.00	0.000419	1.260
140	01025224-3-B	1	0	2.40	0.92	8.87	0.000003	1.261
141	01025226-2-B	0	1	2.40	0.92	19.46	0.000420	1.368
142	01025226-3-B	0	0	2.40	0.93	16.77	0.003193	1.197
143	01025226-4-B	0	0	2.40	0.81	15.08	0.000418	1.241
144	01025226-5-B	0	0	2.40	0.93	17.39	0.000415	1.057
145	01025227-3-B	0	0	2.40	1.01	15.85	0.000419	1.034
146	01025227-4-B	0	0	2.40	0.91	18.91	0.003245	1.184
147	01025227-5-B	1	0	2.40	0.86	11.18	0.000418	1.369
148	01025228-1-B	0	0	2.40	1.02	18.77	0.000416	0.906
149	01025228-2-B	0	0	2.40	0.81	18.40	0.000417	0.929
150	01025228-3-B	0	0	2.40	0.90	15.05	0.000421	1.129
151	01025229-1-B	1	0	2.40	1.07	10.93	0.000422	0.945
152	01025229-2-B	1	0	2.40	0.90	13.24	0.003225	1.060
153	01025229-3-B	0	0	2.40	0.94	17.68	0.000053	1.148
154	01025229-4-B	0	0	2.40	0.97	12.68	0.000419	1.217
155	01025232-2-B	0	0	2.40	0.89	13.09	0.000420	0.852
156	01025232-3-B	0	0	2.40	0.92	18.12	0.000419	0.886
157	01025232-4-B	0	0	2.40	0.90	14.30	0.000004	0.828
158	01025261-3-B	1	0	2.40	1.15	6.43	0.000417	0.663

* 0: no obvious major flaws and/or weakness inclusions, 1: visible obvious flaws and/or weakness inclusions.

** 0: with cardboard bearing strip, 1: without. *** Broken accidentally before getting results

CHAPTER 7 UNIAXIAL COMPRESSIVE TESTING OF LITHOPHYSAL SPECIMENS

7.1 Experimental description

In this chapter, the uniaxial compression tests on specimens containing lithophysae are discussed (Tables 7.1 and 7.2). Nineteen tests fall into this category. These specimens were collected from the upper lithophysal (Tptpul) and lower lithophysal (Tptpll) zones of the Topopah Spring Tuff. Another group of nine tests on specimens that do not contain lithophysae are listed in Tables 7.3 and 7.4 at the end of this chapter.

The nineteen specimens contain a significant number of lithophysae and large vapor-phase altered zones (Fig. 7.1). These weakness inclusions make these specimens much weaker. In some cases measuring the mechanical properties of a specimen becomes difficult or impossible. The main purpose of testing these specimens is to see how they fail. For only six specimens were able to measure strains and calculate “nominal” Young’s modulus as well as Poisson’s ratio. Given that strains and stresses in these specimens are highly nonuniform, these properties can be considered as some descriptor of local axial and lateral stiffness of the specimen. The force-displacement plots for these tests probably give a better measure of the stiffness of these specimens.

Table 7.1 Source information for the specimens containing lithophysae

Specimen ID	Borehole	Range in Borehole (ft)	Zone
01014755-U	USW UZ-14	828.8-828.4	Tptpll
01014979-U	UE-25 UZ#16	422.4-422.8	Tptpul
01014985-U	USW SD-12	442.0-442.4	Tptpul
01014994-U	USW SD-12	513.4-513.8	Tptpul
01015001-U	USW SD-12	600.3-600.6	Tptpul
01015004-U	USW SD-12	614.8-615.4	Tptpul
01015455-1-U	USW SD-12	519.4-520.1	Tptpul
01015456-U	USW SD-12	520.2-520.6	Tptpul
01014723-U	UE-25-UZ#16	785.8-786.3	Tptpll
01014759-U	USW UZ-14	990.4-990.8	Tptpll
01014760-U	USW UZ-14	992.2-992.9	Tptpll
01014765-U	USW UZ-14	1077.3-1077.7	Tptpll
01014779-1-U	USW UZ-14	1137.0-1137.5	Tptpll
01014780-U	USW UZ-14	1023.2-1023.6	Tptpll
01014947-1-U	UE-25 UZ#16	451.2-452.4	Tptpul
01014977-U	UE-25 UZ#16	420.5-420.9	Tptpul
01014986-U	USW SD-12	446.9-447.2	Tptpul
01015003-U	USW SD-12	613.2-613.6	Tptpul
01015453-U	USW SD-12	518.5-518.9	Tptpul

All nineteen specimens have a nominal diameter of 2.4 inch (60.96 mm). Moisture content is not measured. Fig. 7.1 shows two typical specimens.

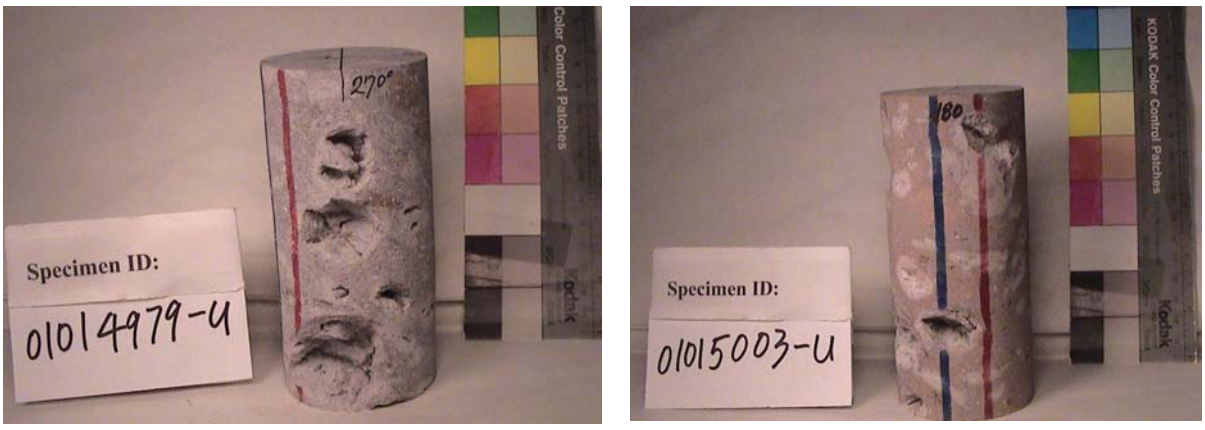

(a) (b)

Figure 7.1 Typical specimens containing lithophysae and vapor-phase altered zones

Strain gages have been installed on specimens as the one shown in Fig. 7.1 (b), but not on the one shown in Fig. 7.1 (a). Strain gage measurements may give some insight into strain distributions around lithophysae, and may assist in clarifying failure mechanisms.

Strains for the six specimens are measured using 350 ohms strain gages. Four strain gages are installed on each specimen. Two measure the axial strain and two measure the lateral strain.

7.2 Results

Test results are shown in Table 7.2. The specimens containing lithophysae do not break in a brittle mode. After initial failure they tend to retain considerable residual strength. Fig. 7.2 shows an example of a specimen after the first loading-unloading cycle.

Table 7.2 Summary of dimensions and test results for the specimens containing lithophysae

Specimen ID	Nomimal Diameter (in)	Length (in)	Strength (MPa)	"Young's Modulus (GPa)" *	"Poisson's Ratio" *
01014755-U	2.4	5.047	30.88	N/A	N/A
01014979-U	2.4	4.961	25.73	N/A	N/A
01014985-U	2.4	4.818	12.01	N/A	N/A
01014994-U	2.4	4.657	25.74	N/A	N/A
01015001-U	2.4	4.738	15.43	N/A	N/A
01015004-U	2.4	4.113	41.27	N/A	N/A
01015455-1-U	2.4	3.981	18.89	N/A	N/A
01015456-U	2.4	3.917	39.49	N/A	N/A
01014723-U	2.4	4.544	98.8	25.73	0.13
01014759-U	2.4	4.936	58.54	N/A	N/A
01014760-U	2.4	5.712	44.02	20.91	0.22
01014765-U	2.4	4.211	57.11	N/A	N/A
01014779-1-U	2.4	5.588	92.94	22.77	0.13
01014780-U	2.4	4.949	94.31	N/A	N/A
01014947-1-U	2.4	3.981	49.55	29.59	0.24
01014977-U	2.4	4.876	30.97	N/A	N/A
01014986-U	2.4	3.912	75.7	26.03	0.2
01015003-U	2.4	5.323	30.96	28.29	0.14
01015453-U	2.4	4.648	33.03	N/A	N/A

* These properties should be considered as nominal values, given the fact that strain and stress distributions in these specimens were strongly nonuniform.

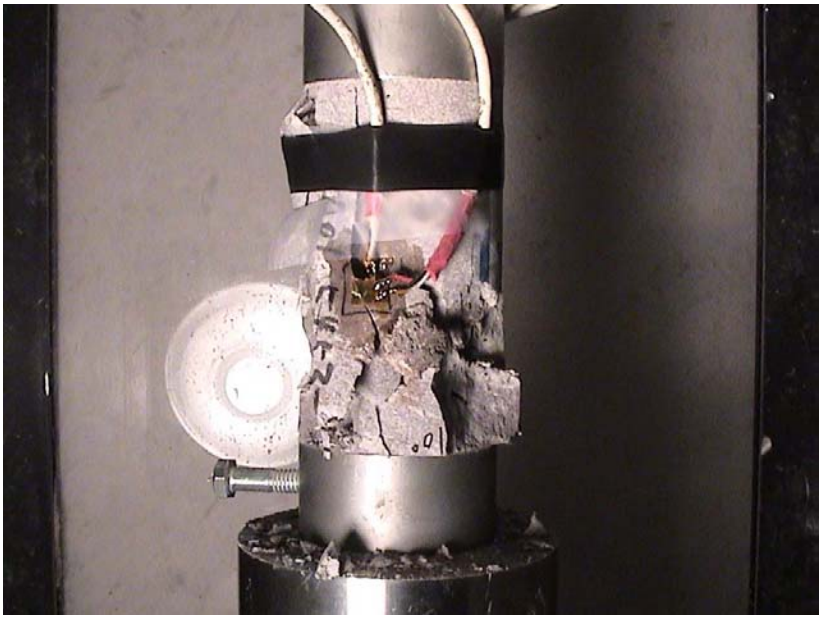

Figure 7.2 A specimen can be loaded again after failure (Specimen ID: 01015453-U).

Figs. 7.3–7.6 show load-displacement plots for four loading-unloading cycles for the specimen shown in Fig. 7.2. The observations from these plots can be summarized as: 1) the significant nonlinear load-displacement relation during loading indicates a large nonlinear compression of the specimen; 2) the "peak" load (or at least a fairly large stress fairly close to the maximum) can be sustained over a large strain range; 3) the maximum load for any subsequent cycle is lower but close to the unloading level of the current cycle. The rock "memorizes" its previous peak strength; 4) when the specimen is unloaded to zero stress, a significant strain remains as a permanent deformation; 5) significant residual strength remains even after very large deformation (Fig. 7.6). The permanent deformation increases significantly with each loading-unloading cycle.

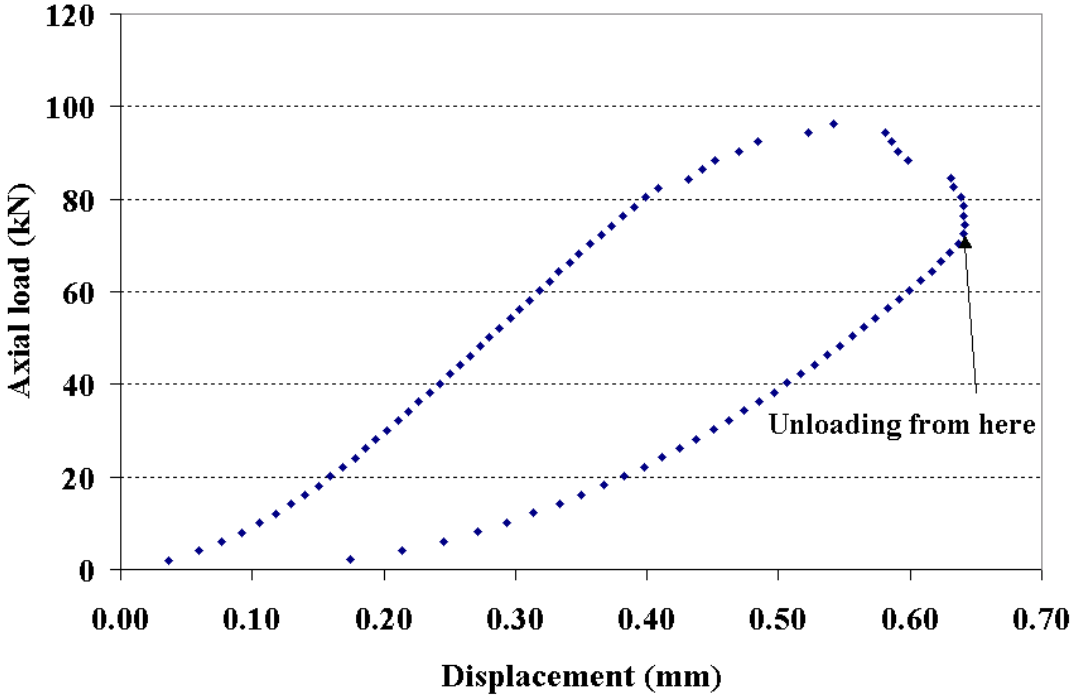

Figure 7.3 Load versus displacement (Specimen ID: 01015453-U, 1st run)

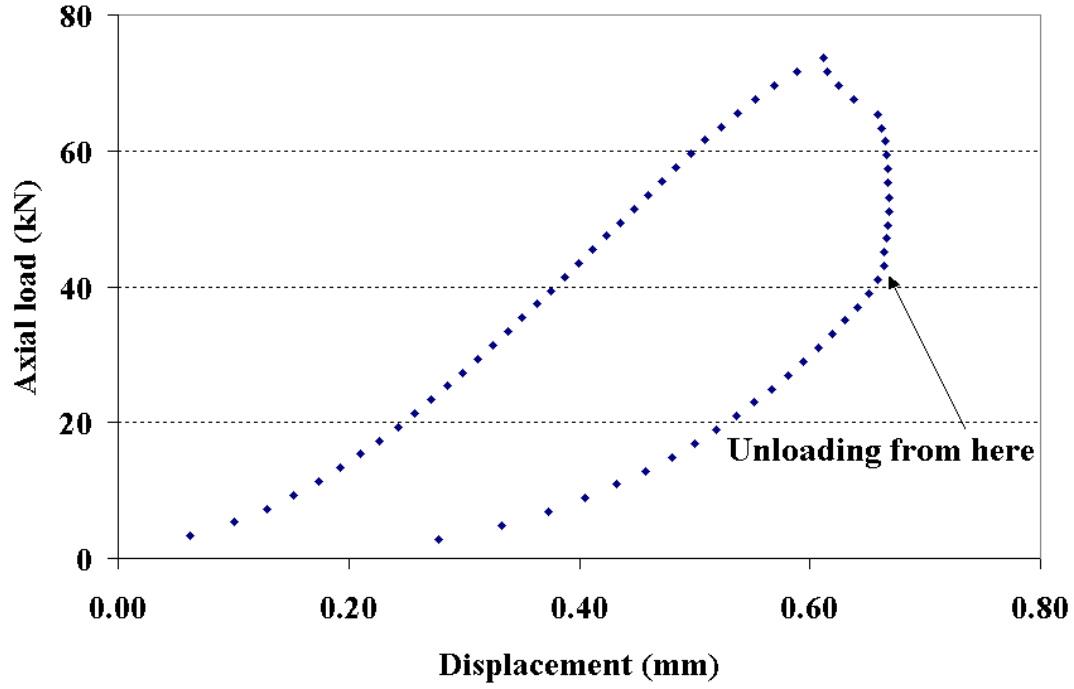

Figure 7.4 Load versus displacement (Specimen ID: 01015453-U, 2nd run)

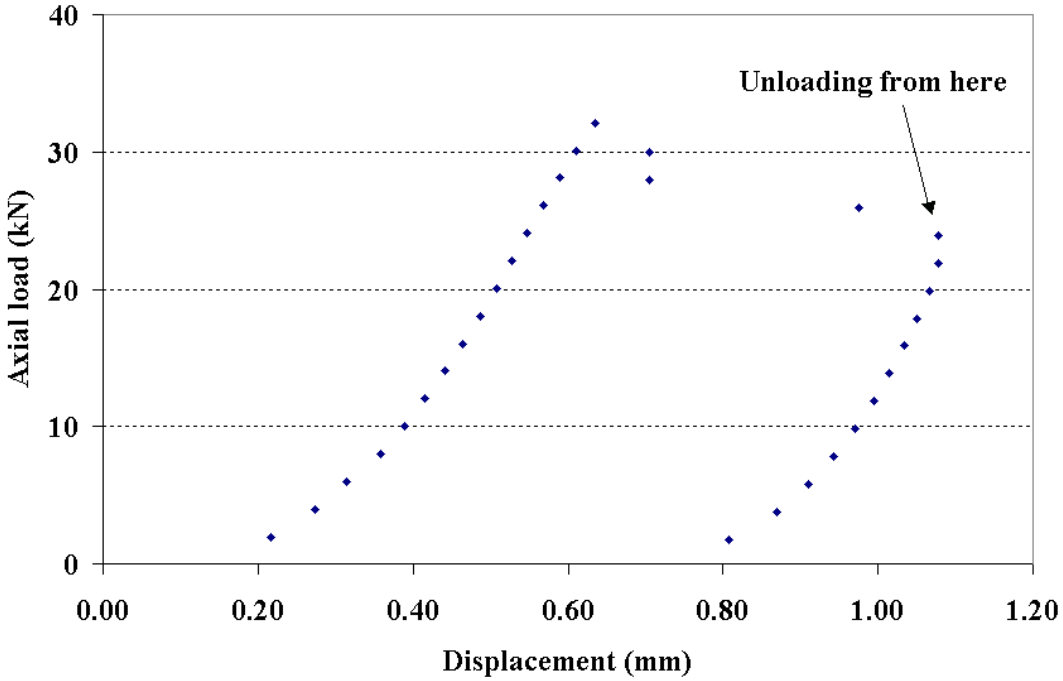

Figure 7.5 Load versus displacement (Specimen ID: 01015453-U, 3rd run)

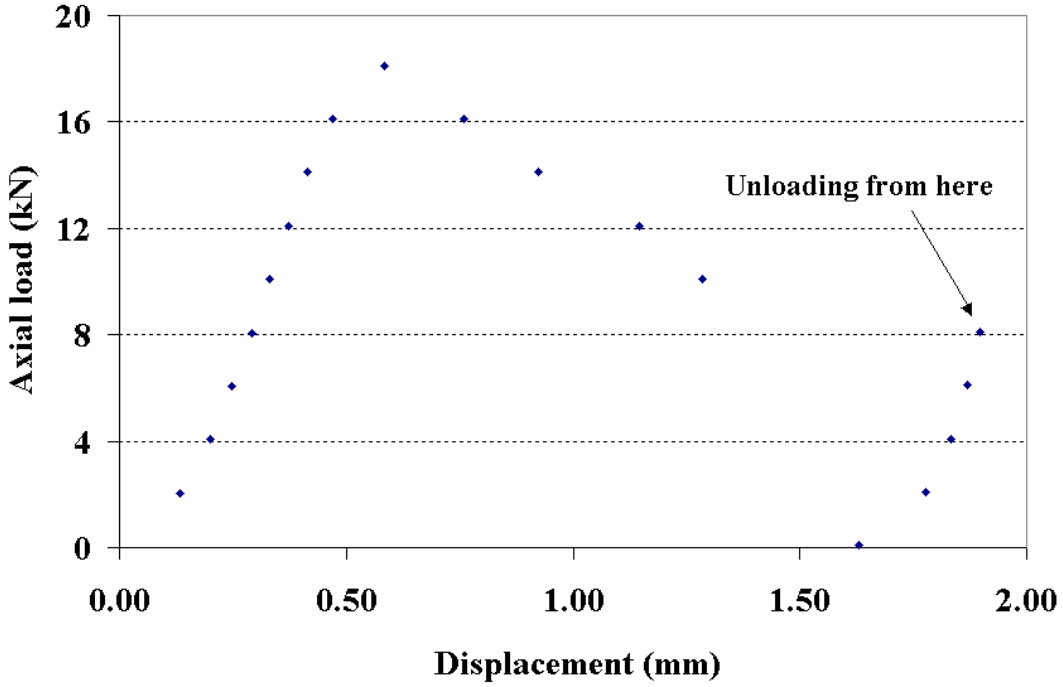

Figure 7.6 Load versus displacement (Specimen ID: 01015453-U, 4th run)

7.3 Future work

1) Laboratory testing of lithophysal specimens can provide considerable insight into potential failure modes of excavations in lithophysal zones, but probably requires more detailed and comprehensive analysis if one is to derive the full benefit of such tests. Striking is the non-brittle slow and gradual progress towards collapse as compared to the exceedingly brittle failure of virtual all nonlithophysal specimens tested. It is possible that a comparison of collapse mechanisms of these lithophysal specimens with those of highly porous materials might be a productive avenue for further investigation into the failure of lithophysal tuff.

   A first step in such a test program would be the installation of strain gages at judiciously chosen positions around lithophysal cavities (and/or using a noncontact displacement monitoring system). The purpose would be to obtain a database that can be analyzed through numerical modeling.

2) Videorecording of failure initiation/propagation.

3) Numerical analysis/simulation of failure initiation and propagation.

4) A/E monitoring of failure initiation and propagation should assist in identifying the location of failure events, and the stress/deformation levels at which they

occur. It is of concern that the highly nonuniform, and unknown, distribution of voids in the specimens is likely to complicate the interpretation and analysis.

Table 7.3 Source information for the specimens not containing lithophysae

Specimen ID	Borehole	Range in Borehole (ft)	Zone
01014764-2-CU(U)	USW WZ-14	1076.1-1076.9	Tptpll
01014950-U	UE-25 UZ#16	544.6-544.9	Tptpmn
01015013-1-U	USW SD-12	781.7-782.5	Tptpmn
01023357-1-U	ESF-MD-NICHE 4788#1	3.3-3.8	Tptpmn
01023359-1-U	ESF-MD-NICHE 4788#1	15.7-16.5	Tptpmn
01023363-2-U	ESF-MD-NICHE 3107#7	12.1-13.6	Tptpmn
01023372-1-U	ESF-MD-NICHE 3107#7	22.7-23.4	Tptpmn
01023567-CU(U)	ESF-HD-WH-3	2.0-2.9	Tptpmn
01025234-2-U	ESF-HD-WH-33	18.0-19.1	Tptpmn

Table 7.4 Summary of dimensions and test results for the specimens not containing lithophysae

Specimen ID	Nominal diameter (in)	Length of Specimen (in)	Loading Rate (MPa/s)	Strength (MPa)	Young's Modulus (GPa)	Poisson's Ratio	Moisture content (%)
01014764-2-CU(U)	2.4	5.945	0.31	80.53	46.9	0.24	N/A
01014950-U	2.4	3.709	0.35	133.55	29.57	0.18	0.332*
01015013-1-U	2.4	4.256	0.44	263.06	34.1	N/A	0.441*
01023357-1-U	1.78	4.29	5.23E-06 /s**	224.42	35.95	0.16	0.335*
01023359-1-U	1.78	4.187	0.37	203.57	30.68	0.15	0.344*
01023363-2-U	1.78	4.29	0.31	116.99	32.61	0.16	0.470*
01023372-1-U	1.78	4.23	0.42	140.49	31.98	0.16	0.497*
01023567-CU(U)	2.4	5.46	3.69E-06 /s**	91.07	46.65	0.22	0.533*
01025234-2-U***	2.4	4.65	N/A	N/A	N/A	N/A	1.065

* Moisture content is measured after testing; ** Displacement control is used when testing; *** Specimen was broken accidentally before getting result.

CHAPTER 8 SUMMARY, CONCLUSIONS AND RECOMMENDATIONS

8.1 Summary

8.1.1 General

Four types of laboratory tests have been conducted on the welded Topopah Spring Tuff. Two types of these tests were performed to study the time dependent behavior of the tuff: constant strain rate tests and creep tests, which were performed under uniaxial compression at room temperature and humidity. Eighty eight specimens tested at constant strain rate were collected form Alcove #5 which was excavated in the middle nonlithophysal zone of the welded Topopah Spring Tuff. Fourteen specimens for creep test were collected from the middle nonlithophysal zone, lower lithophysal zone and lower nonlithophysal zone of the welded Topopah Spring Tuff. In order to apply the analysis results of constant strain rate tests to interpret creep phenomena, it is desirable to have similar mechanical properties of specimens for both groups of tests. For this reason, the analysis of specimens for creep test from middle nonlithophysal zone has been strongly emphasized.

All the specimens for time dependence study exhibit extremely brittle fracture behavior and fail by axial splitting. It is assumed that microfracturing dominates the deformation and failure of the tuff. Based on this assumption, the outcomes of previous studies on crack initiation, crack propagation and crack coalescence as well as their application to brittle rocks are applied to interpret the mechanical behavior of the tuff.

8.1.2 Constant strain rate tests

The eighty eight specimens for constant strain rate tests were divided into two categories: the first category contains sixty five specimens that do not contain obvious flaws. The second category contains twenty three specimens that contain obvious flaws. The sixty five specimens in category 1 are randomly divided into six groups to test at six strain rates: 10^{-2}, 10^{-4}, 10^{-5}, 10^{-6}, 10^{-7}, and 10^{-8} s^{-1}. Test durations range from 2 seconds to 7 days. At a strain rate of 10^{-5} specimens fail in about 10 minutes, corresponding to the test duration prescribed by ASTM D 2938-95. The twenty three specimens in category 2 are tested to study failure patterns and explore how the peak strengths and especially the failure mode are influenced by gross defects at a given strain rate.

Stress-strain curves have been analyzed in order to determine the dilatancy behavior of the tuff, the crack initiation in the tuff and the unstable crack propagation. Nonlinear regression is applied to analyze the strain rate dependency of peak strength, peak axial strain and secant modulus. The peak strength, peak axial strain and secant modulus all decrease with a decrease of strain rate. The decrease can be represented by power functions. Secant modulus serves as a tool for long term strain analysis. An innovative diagram is proposed for strain analysis. Strain rate effected strain component can be separated from peak or total axial strain. This component essentially results from stiffness damage of the tuff specimen. Long term strength has been estimated using nonlinear regression. The long term strength of the tuff is predicted for the 300-year design life step of the HLW repository at Yucca Mountain based on the estimated regression equation.

8.1.3 Creep tests

Stepwise loading is applied to each creep test. Stress increments range from 7 to 10 MPa. Each stress level is maintained at least for three days. The specimens take 2 to 17 stress levels to fail. Accumulated test duration for all the fourteen tests is approximately 401 days. In analysis, transient creep, steady-state creep and accelerating creep are separated for each stress level. Linear regression is applied to steady-state creep to obtain the relation between stress and strain rate. Findings of crack initiation and unstable crack propagation obtained in the constant strain rate study are incorporated to the creep study. Consequently a creep law is created.

8.1.4 Brazilian tests and uniaxial compressive testing of lithophysal specimens

Brazilian tests have been performed on 158 specimens. Three specimens were collected from the lower lithophysal zone of the welded Topopah Spring Tuff. All others were collected from the middle nonlithophysal zone of the welded Topopah Spring Tuff. Brazilian testing have mainly focused on determination of tensile strength of the tuff, lithophysae effect, bearing strip effect and displacement rate dependency of tensile strength. Fracture pattern is analyzed in terms of stress distribution with the aid of finite element simulation.

Nineteen specimens containing a significant number of lithophysae and large vapor-phase altered zones have been tested under uniaxial compression. These specimens were

collected from the upper lithophysal zone and lower lithophysal zone of the welded Topopah Spring Tuff. The main purpose of this type of test is to observe fracture development in the specimens. The following phenomena have been observed: 1) the significant nonlinear load-displacement relation during loading indicates a large nonlinear compression of the specimen; 2) the "peak" load (or at least a fairly large stress fairly close to the maximum) can be sustained over a large strain range; 3) the maximum load for any subsequent cycle is lower but close to the unloading level of the current cycle. The rock "memorizes" its previous peak strength; 4) when the specimen is unloaded to zero stress, a significant strain remains as a permanent deformation; 5) significant residual strength remains even after very large deformation.

8.2 Conclusions

8.2.1 Conclusions based on constant strain rate tests

1) The tuff specimens collected from the middle nolithophysal zone of the welded Topopah Spring Tuff exhibit extremely brittle fracture and fail by axial splitting, and do not show significant dilatancy during deformation.

2) Stress-strain curve analysis indicates that two threshold stresses exist in the course of loading: crack initiation starts at about 50% of peak strength, and unstable crack propagation starts at about 94% of peak strength.

3) Peak strength, peak strain and secant modulus decrease with a decrease of strain rate as power functions: $\sigma_{peak} = 271.37\dot{\varepsilon}^{0.0212}$, $\varepsilon_{peak} = 0.0066\dot{\varepsilon}^{0.0083}$, $E_S = 41985.4\dot{\varepsilon}^{0.015}$.

4) Long term axial strain suffers an explicit reduction and an implicit reduction. The explicit reduction is strain rate effected strain loss. The implicit reduction is caused by stiffness damage of the specimen.

8.2.2 Conclusions based on creep tests

1) Transient creep results from elastic aftereffect. The transient creep curve is best fitted with a power function of time.

2) Two threshold stresses define the creep law for the tuff in the middle nonlithophysal zone. Below about 50% of peak strength, a specimen does not creep regularly. The creep rate is either very low or decays to zero. Above about 94% of peak strength, a specimen creeps at an accelerating rate. Between these two threshold stresses, a power law is found between strain rate and stress: $\dot{\varepsilon}_S = 8 \times 10^{-18} \times \sigma^{4.98}$. The phenomena threshold stresses correspond to microfracturing in the specimen.

8.3 Recommendations

For time dependent study, investigating long term strength and long term strain is the key. To achieve this goal, an intensive and systematic study is essential. In this study a consistent test environment and a well conceived plan are required. The following suggested tests give the main features for such a study plan:

8.3.1 Recommendations for constant strain rate tests

1) Given a diameter, making all test specimens equal length to eliminate size effect.

2) Perform triaxial compression tests to determine effect of σ_3 on strain rate dependency of σ_1. In addition, explore constitutive relations under strain rate variation.

3) Monitor seismic acoustic emissions during loading on specimen. Investigate the relations among stresses, crack development in specimens and release of energy from the specimens.

4) Determine fracture toughness K_{IC} of the tuff and relate the K_{IC} to microfracturing in the tuff.

8.3.2 Recommendations for creep tests

1) Longer term creep testing to test the linearity of secondary creep for different stress levels. This requires maintaining a stress level for a sufficiently long time and keeping the environment temperature constant or within a small range, i.e. ±1°C.

2) Acoustic emission monitoring. For brittle rock, crack growth plays an important or critical role in its damage. Observing the crack initiation and propagation under applied load and relating this progress to creep is an important step towards the creep study.

3) Conduct triaxial compressive creep tests to develop constitutive equations for creep. Emphasize the range of two threshold stresses.

8.3.3 Other recommendations

1) Conduct tests under different moisture content and temperature.

2) Improve strain measurement, e.g. use optical extensometers.

REFERENCES

Anderson, O. L. and P. C. Grew, "Stress Corrosion Theory of Crack Propagation with Applications to Ceophysics", *Review of Geophysics and Space Physics*, Vol. 15, No. 1, Feb. 1977.

Andreev, G. E., 1995, *Brittle Failure of Rock Materials- Tests Results and Constitutive Models.* A.A. Balkema, P.O.Box 1675, 3000 BR Rotterdam, Netherlands.

ASTM D 2938-95, "Standard Test Method for Unconfined Compressive Strength of Intact Rock Core Specimens," *Annual Book of ASTM Standards*, Section 4, Construction, Volume 04.08 Soil and Rock, Building Stones, American Society for Testing and Materials, Philadelphia.

ASTM D 3148 – 96", Standard Test Method For Elastic Moduli Of Intact Rock Core Specimens In Uniaxial Compression", *Annual Book of ASTM Standards*, Section 4, Construction, Volume 04.08 Soil and Rock; Building Stones. American Society for Testing and Materials, Philadelphia.

ASTM D3967-95a, "Standard Test Method for Splitting Tensile Strength of Intact Rock Core Specimens," *Annual Book of ASTM Standards*, Section 4, Construction, Volume 04.08 Soil and Rock; Building Stones. American Society for Testing and Materials, Philadelphia.

ASTM D 4543-85 (Reapproved 1991), "Standard Practice for Preparing Rock Core Specimens and Determining Dimensional and Shape Tolerances," *Annual Book of ASTM Standards*, Section 4, Construction, Volume 04.08 Soil and Rock; Building Stones. American Society for Testing and Materials, Philadelphia.

Bieniawski, Z. T., "Mechanism of Brittle Fracture of Rock: Part I-Theory of the Fracture Process", *Int. J. Rock Mech. Min. Sci.* Vol. 4, No. 4, pp. 395-406, Oct. 1967a.

Bieniawski, Z. T., "Mechanism of Brittle Fracture of Rock: Part II-Experimental Studies", *Int. J. Rock Mech. Min. Sci.* Vol. 4, No. 4, pp. 407-423, Oct. 1967b.

Bieniawski, Z. T., "Mechanism of Brittle Fracture of Rock: Part III-Fracture in Tension and under Long-Term Loading", *Int. J. Rock Mech. Min. Sci.* Vol. 4, No. 4, pp. 425-430, Oct. 1967c.

Bobet, A. and H. H. Einstein, "Fracture Coalescence in Rock-type Materials under Uniaxial and Biaxial Compression", *Int. J. Rock Mech. Min. Sci.* Vol. 35, pp. 863-888, 1998a.

Bobet, A. and H. H. Einstein, "Numerical Modeling of Fracture Coalescence in a Model Rock Material", *Int. J. Frac.* Vol. 92, pp. 221-252, 1998b.

Brace, W. F. and E. G. Bombolakis, “A note on Brittle Crack Growth in Compression.” *Journal of Geophysical Research*. Vol. 68, No. 12, pp. 3709-3713. June 15, 1963.

Brace, W. F., Paulding, Jr., B. W. and C. Scholz, “Dilatancy in the Fracture of Crystalline Rocks.” *Journal of Geophysical Research*, Vol. 71, No. 16, pp. 3939-3953. Aug. 15, 1966.

Brace, W. F., Silver, E., Hadley, K. and C. Goetze. “Crack and Pores: A Closer Look.” *Science*, Vol. 178, No. 4058, Oct. 13, 1972.

Budynas, R. G. 1999. Advanced Strength and Applied Stress Analysis, 2nd Ed., McGraw-Hill, NY, USA.

Buesch, D. C. and R. W. Spengler, “Character of the Middle Nonlithophysal Zone of the Topopah Spring Tuff at Yucca Mountain”, *High-Level Radioactive Waste Management*, *Proceedings of the Eighth International Conference*, Las Vegas, Nevada, May 11-14, 1998.

Costin, L. S., “A Microcrack Model for the Deformation and Failure of Brittle Rock.” *Journal of Geophysical Research*, Vol. 88 No. B11, pp 9485-9492, Nov. 10, 1983.

Costin, L. S., “Time-Dependent Damage and Creep of Brittle Rock.” *Damage Mechanics and Continuum Modeling*, Proceedings of 2 Sessions Sponsored by the Engineering Mechanics Division of the American Society of Civil Engineers in Conjunction with the ASCE Convention, Detroit, Michigan, Stubbs, N. and D. Krajcinovic Ed., Oct. 22, 1985.

Costin, L. S. and D. J. Holcomb, “A Continuum Model of Inelasticity Deformed Brittle Rock Based on the Mechanics of Microcracks”, *Constitutive Laws for Engineering Materials Theory and Application*, Proceedings of the International Conference, Desai, C. S. and R. H. Gallagher Ed. Tucson, Arizona, USA, January 10-14, 1983.

Cristescu, N. D. and U. Hunsche, 1998, *Time Effects in Rock Mechanics*, John Wiley & Sons Ltd, Baffins Lane, Chichester, West Sussex PO19 1 UD, England.

Cruden, D. M., “A Theory of Brittle Creep in Rock under Uniaxial Compression”, *Journal of Geophysical Research*, Vol. 75, No. 17, pp. 3431-3442, June. 10, 1970.

Cruden, D. M., “The Form of the Creep Law for Rock under Uniaxial Compression”, *Int. J. Rock Mech. Min. Sci*., Vol. 8, pp. 105-126, 1971.

Cruden, D. M., “The Static Fatigue of Brittle Rock under Uniaxial Compression”, *Int. J. Rock Mech. Min. Sci. & Geomech. Abstr.,* Vol. 11, pp. 67-73, 1974.

Dey, T. N. and C. Wang, “Some Mechanisms of Microcrack Growth and Interaction in

Compressive Rock Failure", *Int. J. Rock Mech. Min. Sci. & Geomech. Abstr.* Vol. 18, pp. 199-209, 1981.

Dusseault, M. B. and C. J. Fordham. "Time-dependent Behavior of Rocks." in *Comprehensive Rock Engineering, Principles, Practice and Projects*, PERGAMON PRESS, Oxford 1993, Editor-in-Chief J. A. Hudson, Vol.3, pp. 119-149.

Eberhardt, E., Stead, D., Stimpson, B. and R. S. Read, "Identifying crack initiation and propagation threshold in brittle rock", *Can. Geotech. J*., Vol. 35, pp. 222-233, 1998.

Farmer, I., 1983, *Engineering Behaviour of Rocks*, 2nd Ed., Chapman and Hall, London.

Fernandez, G., *Data Mining Using SAS Applications*, Chapman & Hall/CRC, 2003.

Germanovich, L.N., R.L. Salganik, A.V. Dyskin and K.K. Lee, 1994, "Mechanisms of brittle fracture of rock with multiple pre-existing cracks in compression", *Pure and Applied Geophysics* (PAGEOPH), Vol. 143 1/2/3, p. 117-149.

Goodman, R. E., 1989, *Introduction to Rock Mechanics*, 2nd Ed., John Wiley & Sons, New York.

Griggs, D., "Creep of Rocks", *Journal of Geology*, Vol. 48, No. 3, April-May, 1939.

Griggs, D., "Experimental flow of rocks under conditions favoring recrystallization." *Bull. Geol. Soc. Amer*. Vol. 51, pp. 1001-1022, July 1, 1940.

Hallbauer, D. K., Wagner, H. and N. G. W. Cook, "Some Observations Concerning the Microscopic and Mechanical Behavior of Quartzite Specimens in Stiff, Triaxial Compression Tests", *Int. J. Rock Mech. Min. Sci. & Geomech. Abstr*. Vol. 10, pp. 713-726, 1973.

Henry, J. P., Paquet, J. and J. P. Tancrez, "Experimental Study of Crack Propagation in Calcite Rocks", *Int. J. Rock Mech. Min. Sci. & Geomech. Abstr*. Vol. 14, pp. 85-91, 1977.

Holcomb, D. J., "A Quantitative Model of Dilatancy in Dry Rock and its Application to Westerly Granite", *Journal of Geophysical Research*, Vol. 83, No. B10, pp. 4941-4950, Oct. 10, 1978.

Holocomb, D. J., "Memory, Relaxation, and Microfracturing in Dilatant Rock", *Journal of Geophysical Research*, Vol. 86, No. B7, pp. 6235-6248, July. 10, 1981.

Horii, H. and S. Nemat-Nasser, "Compression-Induced Microcrack Growth in Brittle Solids: Axial Splitting and Shear Failure", *Journal of Geophysical Research*, Vol. 90, No. B4, pp. 3105-3125, June. 10, 1985.

Hudson, J. A. “Rock Properties, Testing Methods and Site Characterization”, *Comprehensive Rock Engineering, Principles, Practice and Projects*, PERGAMON PRESS, Oxford 1993, Editor-in-Chief J. A. Hudson, Vol.3, pp. 1-39.

Jaeger, J. C. and N. G. W. Cook, 1979, *Fundamentals of Rock Mechanics*, 3rd Ed., Chapman and Hall, London, UK.

Kranz, R. L. and C. H. Scholz, “Critical Dilatant Volume of Rocks at the Onset of Tertiary Creep”, *Journal of Geophysical Research*, Vol. 82, No. 30, pp. 4893-4898, Oct. 10, 1977.

Kranz, R. L., “Crack Growth and Development During Creep of Barre Granite”, *Int. J. Rock Mech. Min. Sci. & Geomech. Abstr*. Vol. 16, pp. 23-35, 1979.

Kranz, R. L., “Microcracks in Rocks: A Review”, *Tectonophysics*, Vol. 100, pp. 449-480, 1983.

Ladanyi, B., “Time-dependent Response of Rock Around Tunnels”, *Comprehensive Rock Engineering, Principles, Practice and Projects*, PERGAMON PRESS, Oxford 1993, Editor-in-Chief J. A. Hudson, Vol.3, pp. 77-112.

Lajtai, E. Z. and E. J. Dzik, “Searching for the damage threshold in intact rock”, Rock Mechanics Tools and Techniques, Proceedings of the 2nd North American Rock Mechanics Symposium: NARMS’96 A regional Conference of ISRM, Vol. 1, Aubertin, M., Hassani, F. and H. Mitri Ed., Montreal, Quebec, Canada, 19-21 June 1996.

Lajtai, E. Z., “A Theoretical and Experimental Evaluation of the Griffith Theory of Brittle Fracture.” *Tectonophysics*. Vol. 11, pp. 129 – 156, 1971.

Lajtai, E. Z., “Microscopic Fracture Processes in a Granite”, *Rock Mech. Rock Engrg*, Vol. 31 (4), pp. 237-250, 1998.

Lajtai, E. Z., and V. N. Lajtai, “The evolution of brittle fracture in rocks”, *J. Geol. Soc. Lond*. Vol. 130, pp. 1-18, 1974.

Lauterbach, B. and D. Gross, “Crack Growth in Brittle Solids under Compression”, *Mechanics of Materials*, Vol. 29, pp. 81-92, 1998.

Lemaitre, J., *A Course on Damage Mechanics*, Springer-Verlag, NY, 1992.

Martin, C. D., and N. A. Chandler, “The Progressive Fracture of Lac du Bonnet Granite”, *Int. J. Rock Mech. Min. Sci. & Geomech. Abstr.* Vol. 31, No. 8, pp. 643-659, 1994.

Martin, III, R. J, “Time-Dependent Crack Growth in Quartz and Its Application to the Creep of Rocks.” *Journal. of Geophysical Research*. Vol. 77, No. 8, March 10 1972.

Martin, III, R. J., Price, R. H., Boyd, P. J. and J. S. Noel. "The Influence of Strain Rate and Sample Inhomogeneity on the Moduli and Strength of Welded Tuff." *Int. J. Rock Mech. Min. Sci. & Geomech. Abstr*. Vol. 30, No. 7, pp. 1507-1510, 1993.

Martin, III, R. J., Price, R. H., Boyd, P. J. and J. S. Noel, *Creep in Topopah Spring Member Welded Tuff*. SAND94-2585, UC-814. Sandia National Laboratories, 1995.

Martin, R. J., Noel, J. S., Boyd, P. J and R. H. Price, "Creep Properties of the Paintbrush Tuff Recovered from Borehole USW NRG-7/7A: Data Report." SAND95-1759, UC-814. Sandia National Laboratories, 1997.

Munson, D. E. and P. R. Dawson, "Constitutive Model for the Low Temperature Creep of Salt (with Application to WIPP)", SAND79-1853. Sandia National Laboratories, 1979.

Neter, J., Kutner, M. H., Nachtsheim, C. J. and W. Wasserman, *Applied Liner Regression Models*, 3rd Ed., McGraw-Hill Companies, Inc., 1996.

OCRWM (Office of Civilian Radioactive Waste Management), 1999. *Geology of the ECRB Cross Drift - Exploratory Studies Facility, Yucca Mountain Project, Yucca Mountain, Nevada*, prepared by G.S. Mongano, W.L. Singleton, T.C. Moyer, S.C. Beason, G.L.W. Eatman, A.L. Albin, and R.C. Lung, Bureau of Reclamation and U.S. Geological Survey. Denver, Colorado.

OCRWM (Office of Civilian Radioactive Waste Management), 2002a. *Yucca Mountain Science and Engineering Report,* Rev 1.

OCRWM (Office of Civilian Radioactive Waste Management), 2002b. *Yucca Mountain Site Suitabilit Evaluation*. DOE/RW-0549.

OCRWM (Office of Civilian Radioactive Waste Management), *Yucca Mountain Project*, from Website http://www.ocrwm.doe.gov/index.shtml, March 15, 2004.

Paterson, M. S., *Experimental Rock Deformation-The Brittle Field*, Sprinere-Verlag Berlin, 1978.

Sagong, M. and A. Bobet, "Coalescence of multiple flaws in a rock-model material in uniaxial compression", *Int. J. Rock Mech. Min. Sci.* Vol. 39, pp. 229-241, 2002.

Sano, O., Ito, I. and M. Terada, "Influence of Strain Rate on Dilatancy and Strength of Oshima Granite under Uniaxial Compression", *Journal of Geophysical Research*, Vol. 86, No. B10, pp. 9299-9311, Oct. 10, 1981.

Sano, O., Terada, M. and S. Ehara, "A Study on the Time-Dependent Microfracturing and Strength of Oshima Granite", *Tectonophysics*, Vol. 84, pp. 343-362, 1982.

Schmidtke, R. H. and E. Z. Lajtai, “The Long-term Strength of Lac du Bonnet Granite.” *Int. J. Rock Mech. Min. Sci. & Geomech. Abstr*. Vol. 22, No. 6, pp. 461-465, 1985.

Scholz, C. H., “Mictofracturing and the Inelastic Deformation of Rock in Compression”, *Journal of Geophysical Research*, Vol. 73, No. 4, pp. 1417-1432, Feb.15, 1968a.

Scholz, C. H., “Experimental Study of the Fracturing Process in Brittle Rock”, *Journal of Geophysical Research*, Vol. 73, No. 4, pp. 1447-1454, Feb.15, 1968b.

Scholz, C. H., “Mechanism of Creep in Brittle Rock”, *Journal of Geophysical Research*, Vol. 73, No. 10, pp. 3295-3302, May 15, 1968c.

Shen, B., Stephansson, O., Einstein, H. H. and G. Bidjan, “Coalescence of fractures under shear stresses in experiments”, *Journal of Geophysical Research*, Vol. 100, No. B4, pp. 5975-5990, April 10, 1995.

Swanson, P. L., “Subcritical Crack Growth and Other Time- and Environment-Dependent Behavior in Crustal Rocks”, *Journal of Geophysical Research*, Vol. 89, No. B6, pp. 4137-4152, June. 10, 1984.

Tang, C. A., Lin, P., Wong, R. H. C. and K. T. Chau, “Analysis of crack coalescence in rock-like materials containing three flaws-Part II: numerical approach”, *Int. J. Rock Mech. Min. Sci.* Vol. 38, pp. 925-939, 2001.

Timoshenko, S. P., *History of strength of materials: with a brief account of the history of theory of elasticity and theory of structures*, McGraw-Hill, New York, 1953.

Vasarhelyi, B. and A. Bobet, “Modeling of Crack Initiation, Propagation and Coalescence in Uniaxial Compression”, *Rock Mech. Rock Engng*, Vol. 33 (2), pp. 119-139, 2000.

Walsh, J. B., “The Effect of Cracks on the Uniaxial Elastic Compression of Rocks”, *Journal of Geophysical Research*, Vol. 70, No. 2. pp. 399-411. Jan. 15, 1965.

Wiederhorn, S. M. and L. H. Bolz, "Stress Corrosion and Static Fatigue of Glass", J. Am. Ceram. Soc. 53, pp. 543-548, 1970.

Wong, R. H. C., Chau, K. T., Tang, C. A. and P. Lin, “Analysis of crack coalescence in rock-like materials containing three flaws-Part I: experimental approach”, *Int. J. Rock Mech. Min. Sci.* Vol. 38, pp. 909-924, 2001.

APPENDIX A SUMMARY OF RESULTS FOR ALL SPECIMENS IN CONSTANT STRAIN RATE TESTS

Serial #	Specimen ID	Nominal diameter (in)	Length of Specimen (in)	Strain Rate (s^{-1})	Strength (MPa)	Young's Modulus (GPa)	Poisson's Ratio	Moisture content (%)
1	01023568-1-CU(U)	2.4	5.40	6.07E-06	140.85	46.46	0.21	0.534*
2	01023570-1-U	2.4	4.74	1.45E-05	142.12	22.77	N/A	0.742*
3	01023570-U	2.4	4.78	1.41E-05	98.35	28.32	0.25	0.653
4	01023575-1-U	2.4	4.23	1.33E-07	223.10	34.61	N/A	0.772*
5	01023575-2-U	2.4	4.71	1.35E-07	101.80	28.34	N/A	0.733*
6	01023576-2-U	2.4	5.66	1.08E-07	128.59	33.38	N/A	0.769*
7	01023576-3-U	2.4	6.04	1.10E-08	163.28	35.71	N/A	0.702*
8	01023579-1-U	2.4	5.93	1.11E-05	135.97	37.63	0.19	N/A
9	01023580-U	2.4	5.50	1.24E-06	172.00	34.10	0.19	0.706*
10	01023581-2-U	2.4	5.38	1.15E-07	183.54	35.25	N/A	0.648*
11	01023582-1-U	2.4	5.60	1.24E-05	202.98	33.66	0.19	0.744*
12	01023586-3-U	2.4	4.92	1.34E-08	253.29	36.47	N/A	0.721*
13	01023657-1-U	2.4	6.02	1.13E-05	233.16	37.14	0.17	0.727*
14	01023657-3-U	2.4	5.70	1.18E-05	216.95	35.58	0.16	0.796*
15	01023657-4-U	2.4	4.26	1.33E-05	261.63	36.18	0.18	0.620
16	01023660-1-U	2.4	4.93	1.32E-07	168.10	33.08	N/A	0.663*
17	01023662-1-U	2.4	6.02	1.15E-07	204.55	35.04	0.12	0.672
18	01023662-2-U	2.4	5.93	9.89E-06	203.36	37.64	0.16	0.783*
19	01023662-3-U	2.4	5.67	1.44E-05	163.95	41.73	N/A	0.877
20	01023663-1-U	2.4	5.40	1.21E-05	275.96	34.94	0.18	0.701*
21	01023663-2-U	2.4	5.80	1.11E-08	173.21	36.55	N/A	0.811*
22	01023664-U	2.4	6.04	1.08E-05	239.62	36.39	0.18	0.788*

Appendix A (Continued)

23	01023667-1-U	2.4	5.87	1.19E-06	176.63	38.96	0.15	0.616
24	01023667-2-U	2.4	5.21	1.39E-07	215.07	32.83	N/A	0.450*
25	01023668-3-U	2.4	5.44	1.36E-08	113.21	28.15	N/A	0.886*
26	01023682-2-U	2.4	6.12	1.16E-07	121.15	35.09	0.23	0.645
27	01023682-3-U	2.4	5.25	1.09E-05	142.7	34.15	0.16	N/A
28	01023686-1-U	2.4	4.72	1.28E-06	252.54	37.12	0.18	0.535
29	01023686-2-U	2.4	5.96	1.16E-06	242.43	36.16	0.16	0.494
30	01023687-1-U	2.4	5.87	1.05E-05	275.22	41.43	0.16	0.509
31	01023687-2-U	2.4	5.83	1.04E-06	213.02	40.36	0.16	0.636
32	01023687-3-U	2.4	4.27	1.31E-07	241.02	35.58	0.19	0.702
33	01023689-2-U	2.4	5.81	1.13E-04	228.02	35.45	0.16	0.825*
34	01023690-1-U	2.4	4.59	1.35E-04	248.61	36.44	0.15	0.561
35	01023691-1-U	2.4	4.53	1.43E-06	259.94	34.35	0.16	0.633
36	01023691-2-U	2.4	4.35	1.47E-05	172.71	31.14	0.19	0.812
37	01023692-U	2.4	5.51	1.18E-04	213.68	34.40	0.15	0.776*
38	01023694-1-U	2.4	4.69	1.12E-05	155.73	39.72	0.15	0.652
39	01023694-2-U	2.4	5.10	1.35E-06	244.80	34.44	0.18	0.640
40	01023695-1-U	2.4	5.30	1.11E-04	107.78	36.72	0.16	0.634
41	01023695-2-U	2.4	5.74	1.20E-05	203.02	36.00	0.13	0.680
42	01023697-1-U	2.4	5.38	1.37E-07	215.19	31.85	N/A	0.654*
43	01023697-4-U	2.4	5.76	1.26E-07	163.16	29.95	N/A	0.644*
44	01023701-1-U	2.4	5.84	1.16E-05	242.89	32.36	0.17	0.861*
45	01023702-2-U	2.4	5.32	1.17E-05	223.90	34.48	0.15	0.769
46	01023702-3-U	2.4	5.94	1.25E-05	253.72	31.09	0.21	0.745
47	01023703-1-U	2.4	5.01	1.25E-04	264.53	35.07	0.15	0.753

Appendix A (Continued)

48	01023703-2-U	2.4	4.64	1.31E-04	214.41	35.39	0.15	0.696
49	01023706-1-U	2.4	4.41	2.78E-08	199.89	31.12	0.12	0.877
50	01023707-1-U	2.4	5.95	1.17E-06	192.01	34.07	0.15	0.792
51	01023707-2-U	2.4	4.70	1.42E-07	143.24	29.14	0.16	0.757
52	01023707-3-U	2.4	4.85	1.33E-05	232.55	30.56	0.18	0.722
53	01023722-2-U	2.4	4.58	1.38E-06	296.47	35.75	0.19	0.645
54	01023732-U	2.4	5.60	9.80E-06	122.28	40.26	0.12	0.479
55	01023740-1-U	2.4	6.02	1.09E-05	225.33	38.02	0.15	0.654
56	01023740-2-U	2.4	5.92	1.00E-05	121.69	35.94	0.11	0.758
57	01023743-1-U	2.4	6.00	1.05E-05	167.47	37.59	N/A	0.766
58	01023745-1-U	2.4	6.04	1.05E-05	157.69	35.93	0.17	0.618
59	01023747-1-U	2.4	4.92	1.24E-06	264.26	35.91	0.15	N/A
60	01023747-3-U	2.4	4.80	1.15E-04	210.88	39.28	0.16	N/A
61	01023749-2-U	2.4	5.84	1.15E-06	157.6	37.24	0.21	0.767
62	01023750-U	2.4	4.54	1.21E-05	176.52	38.1	0.18	0.688
63	01023751-1-U	2.4	5.63	1.16E-07	176.95	34.51	0.17	0.597
64	01023754-2-U	2.4	4.45	1.40E-06	152.53	28.94	0.15	0.856
65	01023760-1-U	2.4	6.94	1.02E-05	126.12	34.08	0.13	0.855
66	01023760-2-U	2.4	5.45	9.85E-05	158.24	39.36	0.15	0.833
67	01025224-1-U	2.4	5.03	1.32E-04	209.32	35.06	0.12	0.845
68	01025224-3-U	2.4	6.12	1.06E-05	154.49	35.03	0.18	0.772
69	01025225-1-U	2.4	6.03	1.05E-04	196.68	37.47	0.17	0.759
70	01025225-2-U	2.4	6.14	1.16E-04	217.53	33.85	0.13	0.793
71	01025226-1-U	2.4	4.99	1.29E-07	227.37	35.32	0.20	0.674
72	01025227-1-U	2.4	5.92	9.65E-04	189.27	38.93	0.2	0.684

Appendix A (Continued)

73	01025227-2-U	2.4	4.25	8.85E-03	198.7	41.62	0.17	0.813
74	01025230-1-U	2.4	5.11	1.47E-06	209.46	29.28	0.12	0.744
75	01025230-2-U	2.4	4.90	1.16E-05	269.62	37.19	0.18	0.692
76	01025231-1-U	2.4	6.10	1.04E-05	142.85	35.72	0.16	0.670
77	01025231-2-U	2.4	6.67	8.72E-06	72.86	30.87	N/A	0.880
78	01025232-1-U	2.4	5.76	7.45E-03	215.84	38.22	0.15	0.743
79	01025233-1-U	2.4	6.89	1.01E-07	197.48	32.73	0.11	0.723
80	01025234-1-U	2.4	5.08	1.30E-05	291.64	36.32	0.16	1.039
81	01025235-1-U	2.4	4.89	1.24E-04	285.88	37.41	0.14	0.789
82	01025235-2-U	2.4	4.96	1.30E-06	229.75	35.87	0.16	0.661
83	01025259-1-U	2.4	6.08	1.10E-06	238.26	37.43	0.17	0.711
84	01025260-1-U	2.4	5.91	1.33E-06	212.17	32.86	0.14	0.718
85	01025261-1-U	2.4	5.61	1.07E-04	133.74	36.15	0.13	0.735
86	01025262-U	2.4	5.09	5.43E-03	272.85	43.22	0.17	0.727
87	01025263-U	2.4	6.62	8.75E-06	98.27	36.79	0.11	0.943
88	01025264-U	2.4	5.72	1.09E-07	119.22	35.42	0.15	0.775

* Moisture content is measured after testing.

APPENDIX B STRESS-TIME AND AXIAL STRAIN-TIME CURVES FOR TWELVE CREEP TESTS

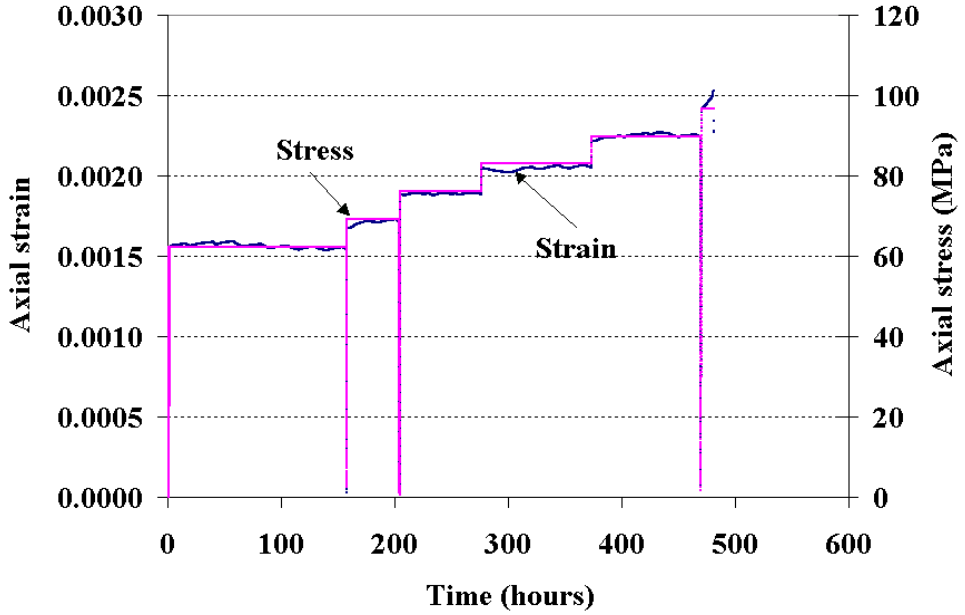

Figure B-1 Stress-time and strain-time curves for test 01014949-1-CU

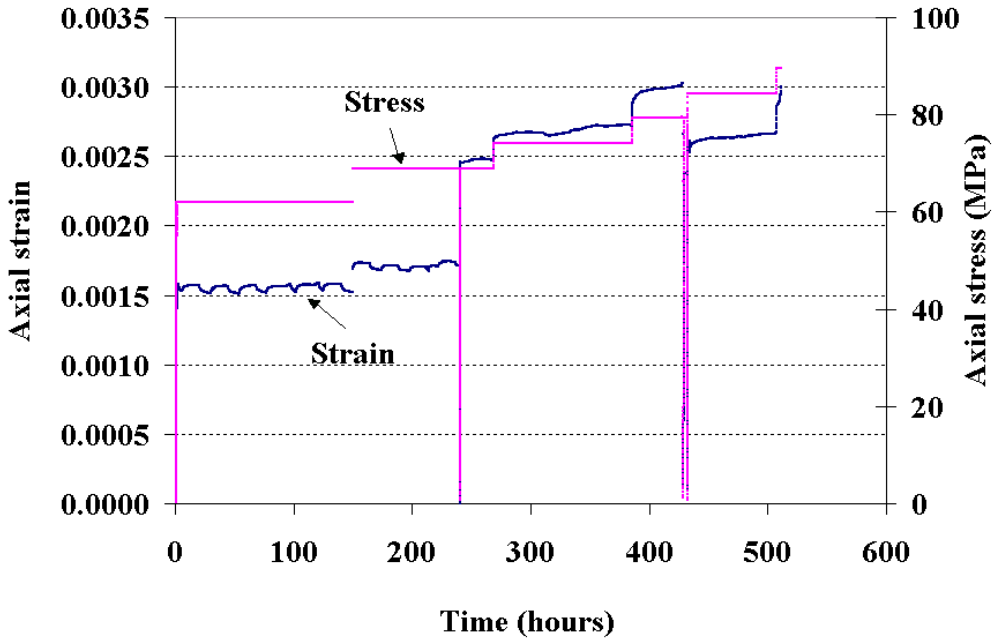

Figure B-2 Stress-time and strain-time curves for test 01014951-1-CU

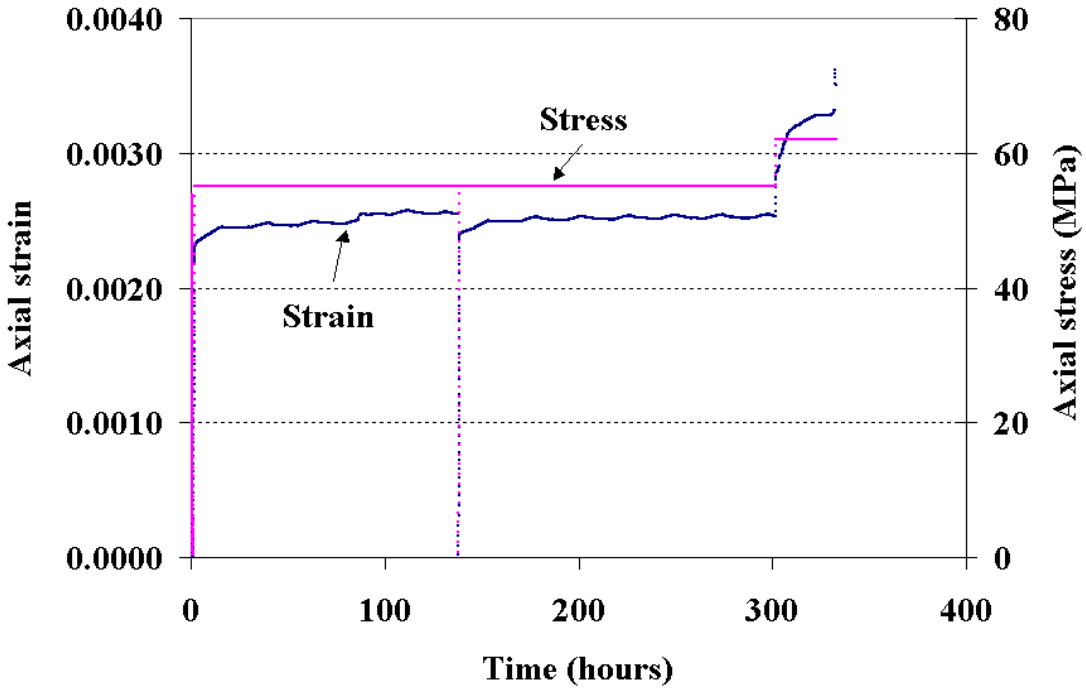

Figure B-3 Stress-time and strain-time curves for test 01014951-2-CU

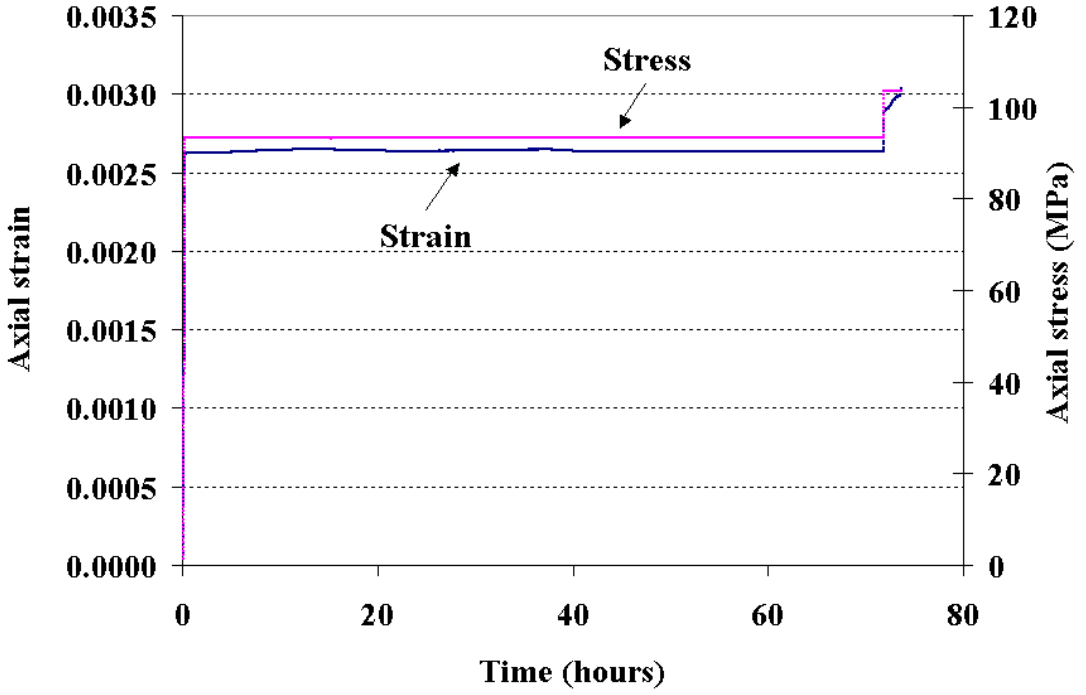

Figure B-4 Stress-time and strain-time curves for test 01014733-2-CU

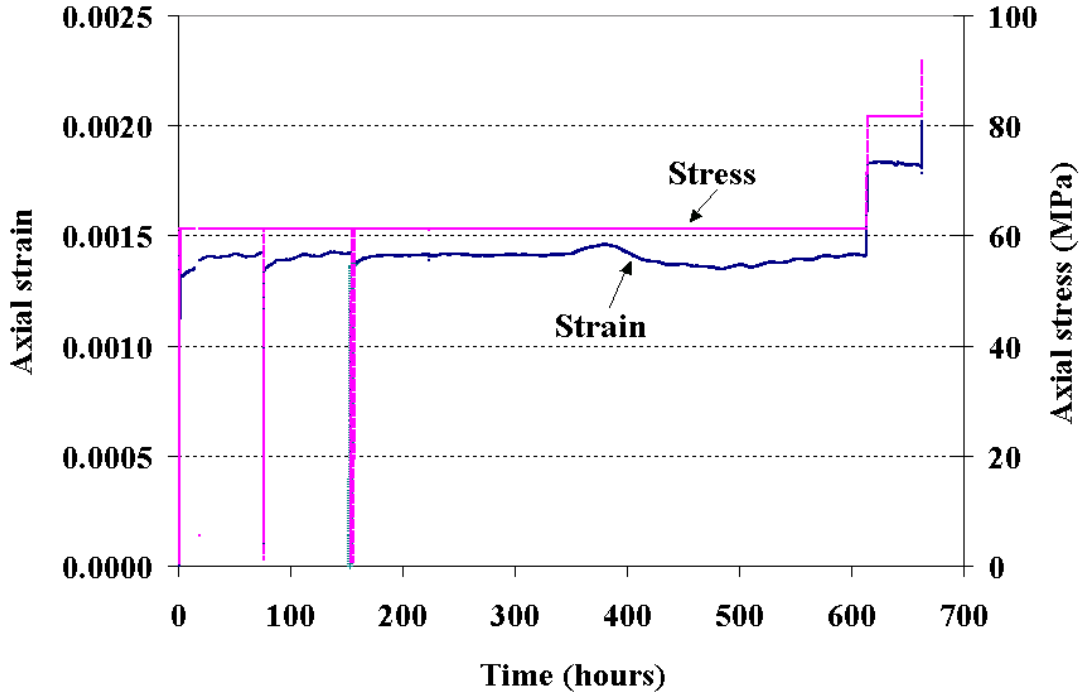

Figure B-5 Stress-time and strain-time curves for test 01014756-1-CU

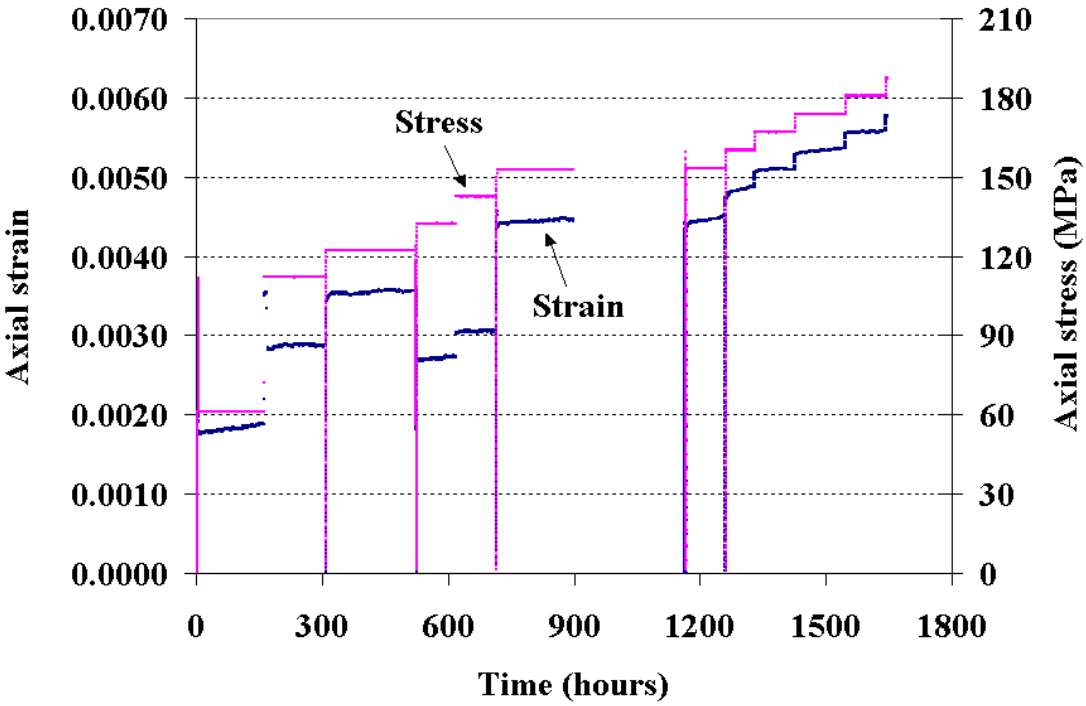

Figure B-6 Stress-time and strain-time curves for test 01015022-1-CU

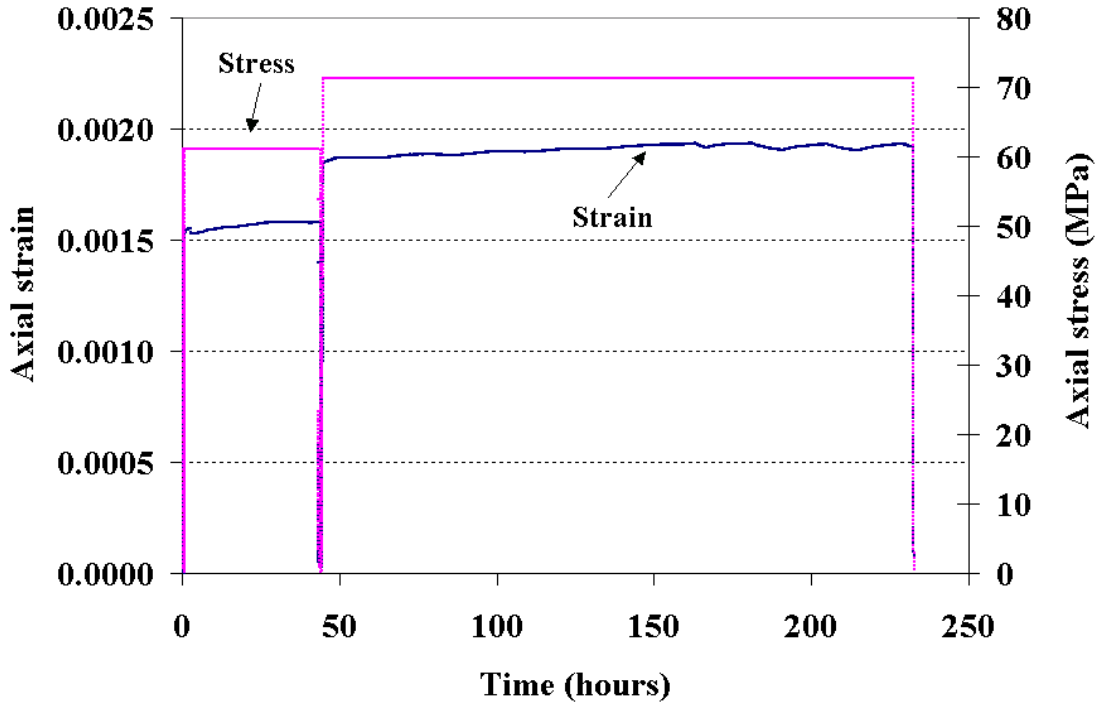

Figure B-7 Stress-time and strain-time curves for test 01015022-2-CU

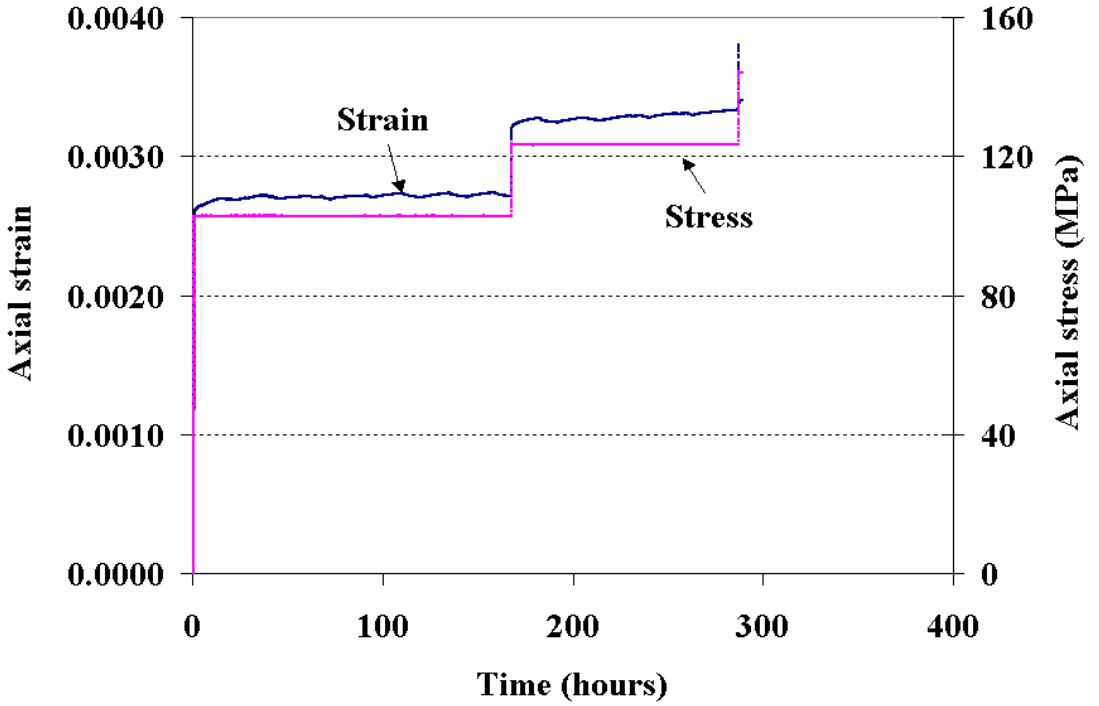

Figure B-8 Stress-time and strain-time curves for test 01015465-CU

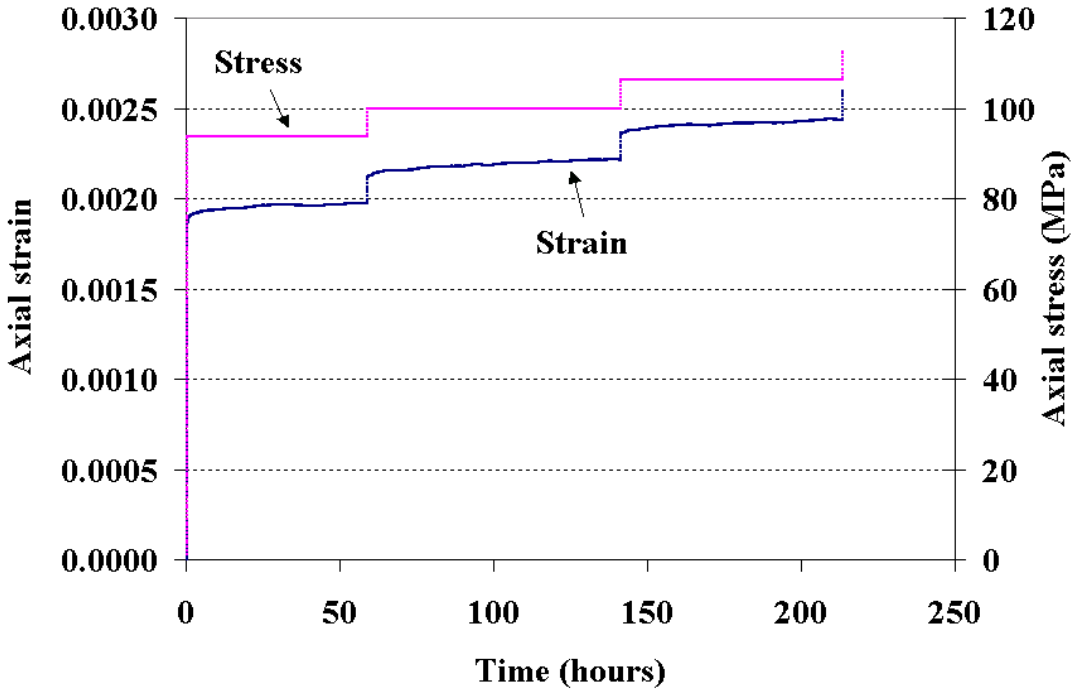

Figure B-9 Stress-time and strain-time curves for test 01023361-1-CU

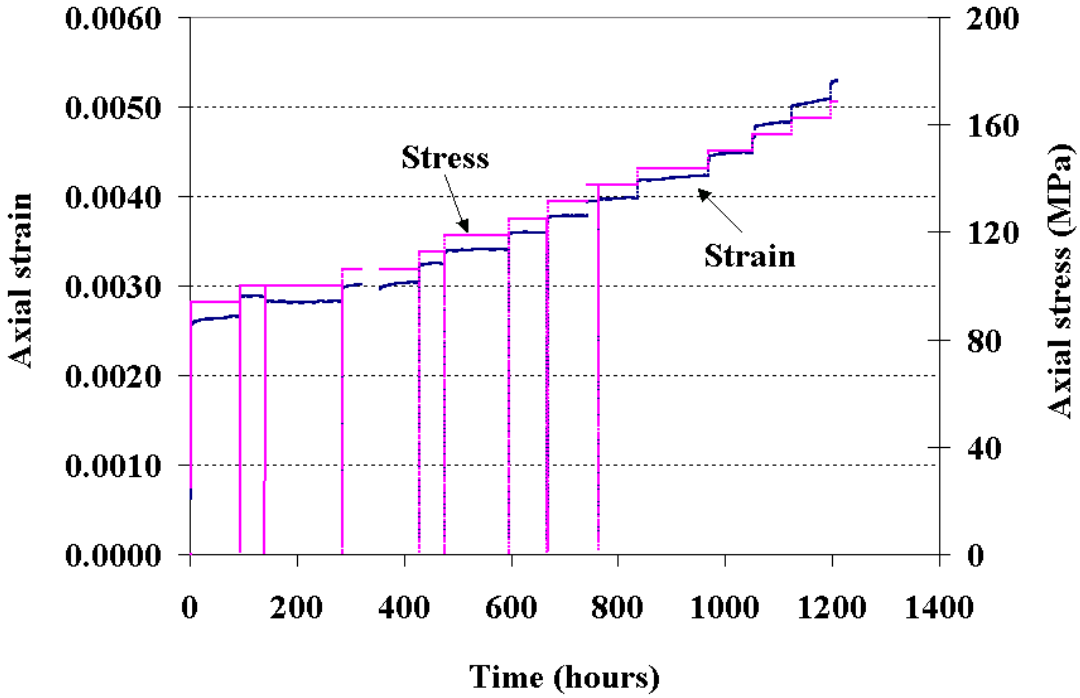

Figure B-10 Stress-time and strain-time curves for test 01023363-1-CU

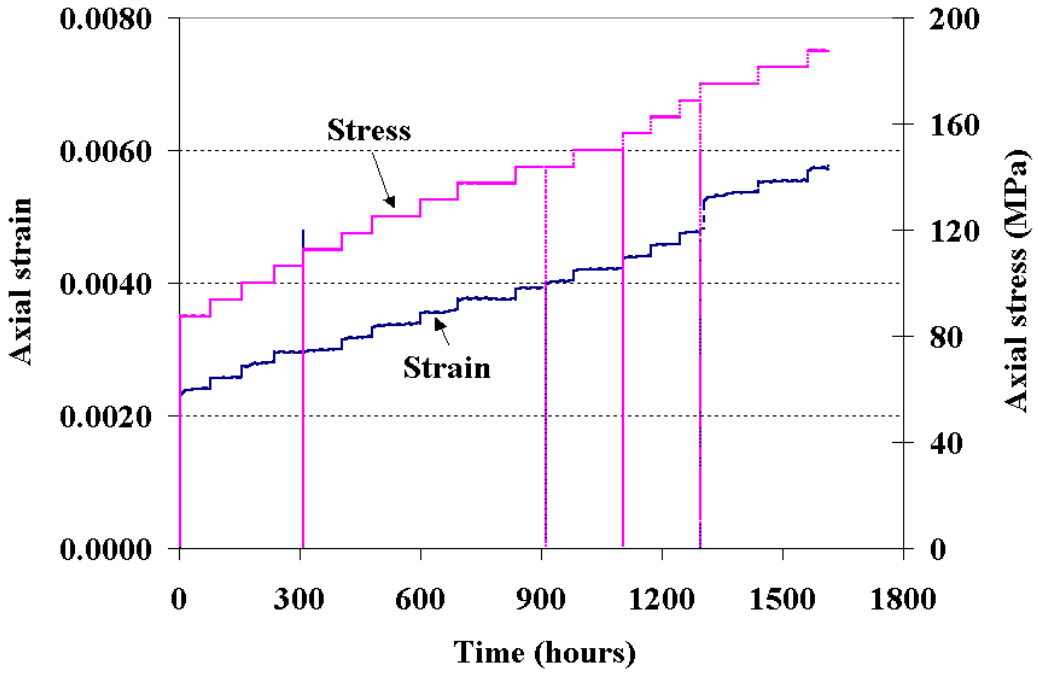

Figure B-11 Stress-time and strain-time curves for test 01023363-3-CU

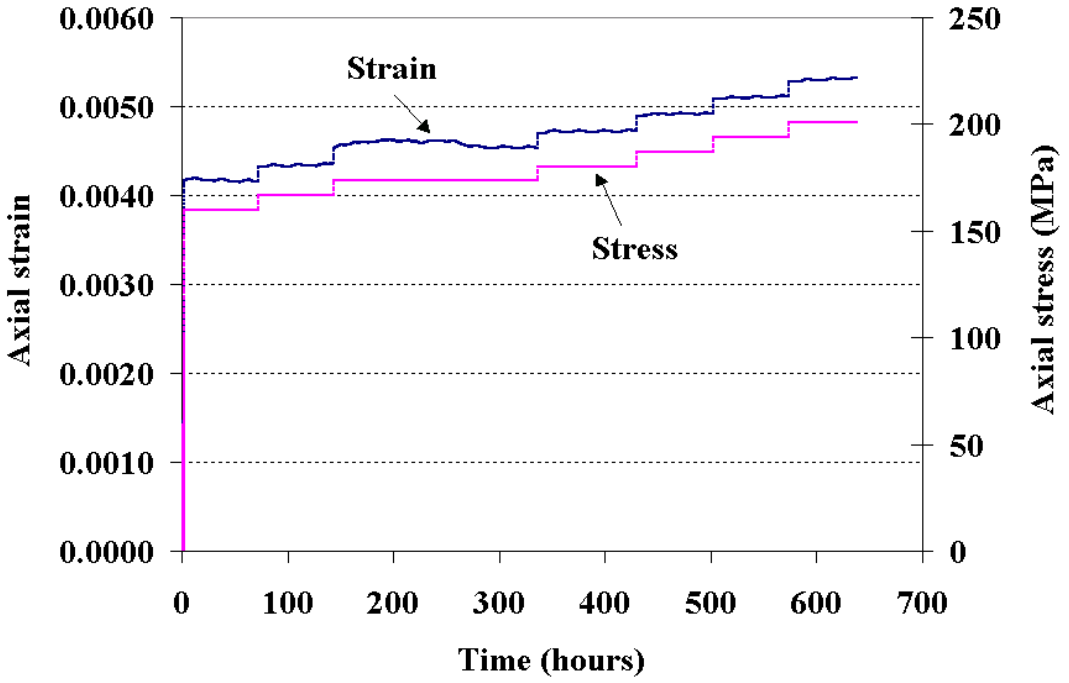

Figure B-12 Stress-time and strain-time curves for test 01023582-3-CU